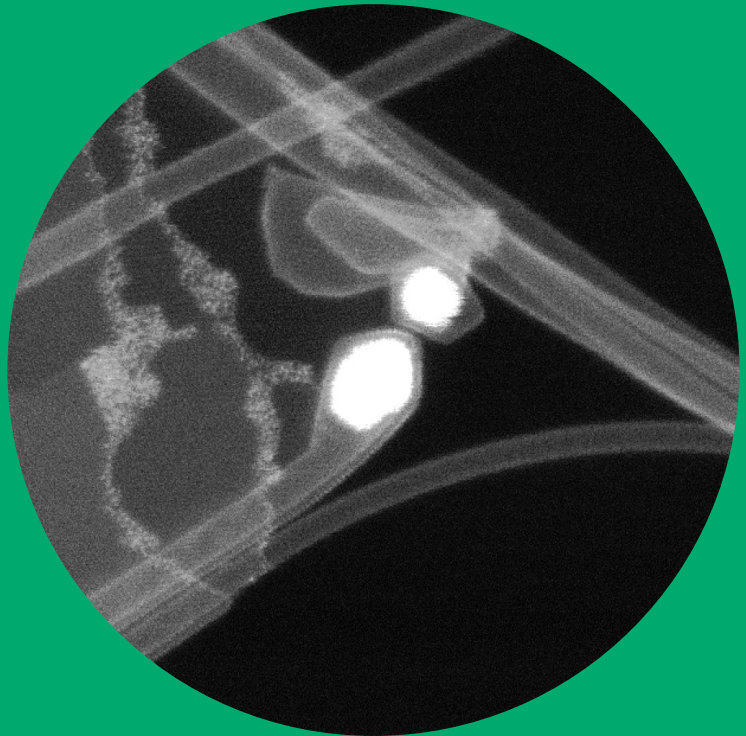


Aerosol CVD synthesis and applications of single-walled carbon nanotube thin films using spark-discharged produced catalyst

Saeed Ahmad



Aerosol CVD synthesis and applications of single-walled carbon nanotube thin films using spark-discharged produced catalyst

Saeed Ahmad

The public defense will be organized via remote technology.
Link: <https://aalto.zoom.us/j/7615938115>

Zoom Quick Guide: <https://www.aalto.fi/en/services/zoom-quick-guide>

A doctoral dissertation completed for the degree of Doctor of Science (Technology) to be defended, with the permission of the Aalto University School of Science, at a public examination held at the lecture hall Tietotekniikka T1 of the school on 17 April 2020 at 12:00.

**Aalto University
School of Science
Department of Physics
NanoMaterials Group**

Supervising professor

Professor Esko I. Kauppinen, Aalto University, Finland.

Thesis advisor

Dr. Qiang Zhang, Aalto University, Finland.

Preliminary examiners

Professor Hong-Zhang Geng, Tiangong University, Tianjin, China.

Professor Seunghyun Baik, Sungkyunkwan University, South Korea.

Opponent

Professor Thomas Wågberg, Umeå University, Umeå, Sweden.

Aalto University publication series

DOCTORAL DISSERTATIONS 44/2020

© 2020 Saeed Ahmad

ISBN 978-952-60-3795-0 (printed)

ISBN 978-952-60-3796-7 (pdf)

ISSN 1799-4934 (printed)

ISSN 1799-4942 (pdf)

<http://urn.fi/URN:ISBN:978-952-60-3796-7>

Unigrafia Oy

Helsinki 2020

Finland



Author

Saeed Ahmad

Name of the doctoral dissertation

Aerosol CVD synthesis and applications of single-walled carbon nanotube thin films using spark-discharged produced catalyst

Publisher School of Science

Unit Department of Physics

Series Aalto University publication series DOCTORAL DISSERTATIONS 44/2020

Field of research Engineering Physics

Manuscript submitted 10 December 2019

Date of the defence 17 April 2020

Permission for public defence granted (date) 11 February 2020

Language English

☐ **Monograph**

☒ **Article dissertation**

☐ **Essay dissertation**

Abstract

Structural controlled synthesis of single-walled carbon nanotubes (SWCNTs) have attracted a great deal of attention due to their widespread potential applications in electronics and photonics. Floating catalyst chemical vapor deposition (FC-CVD) being a dry and continuous method, is a highly promising technique for the scalable synthesis of SWCNTs. However, due to in-situ catalyst formation in all the conventional FC-CVD approaches, it is hard to get full control of number concentration, composition and size of nanoparticles. Hence, it hinders to investigate the effects of catalyst composition on morphology, yield and structure of SWCNTs.

In this thesis, firstly we designed a novel rod-to-tube type spark discharge generator (R-T SDG) to produce ex-situ catalyst nanoparticles for the FC-CVD growth of SWCNTs. We utilized highly time-stable and uniform number size distributions of monometallic (Fe, Ni, Co) and bimetallic (Co-Fe, Co-Ni) catalyst particles for the synthesis of SWCNTs using ethylene as carbon source and 1050 °C temperature. Optical characterizations revealed that as-grown SWCNTs have high-quality and their mean diameter is around 1 nm. The highest SWCNTs yield was obtained with Fe as a catalyst. From electron diffraction analysis, we observed that Co-Ni can produce comparatively narrower chirality and diameter distribution of SWCNTs.

Secondly, we introduced sulfur in the FC-CVD reactor as a growth promoter for the fabrication of SWCNTs based transparent conducting films (TCFs). We systematically investigated the roles of sulfur on yield, morphology, and structure of SWCNTs. It was found that the yield of SWCNTs is largely dependent on amount of sulfur introduced into the FC-CVD reactor and catalyst composition. More importantly, the addition of an optimized amount of sulfur has enhanced approximately three times, the opto-electronic performance of SWCNT-TCFs, by increasing diameter and bundle length along with improving the quality of SWCNTs. The mean diameter of SWCNTs increased from 1 nm to 1.2 nm while the ratio of metallic nanotubes slightly increased from 39% to 41% with sulfur addition. Surprisingly, chirality determination of as-grown SWCNTs indicated that sulfur promoter has little influence on modulating the chirality of SWCNTs.

Finally, we demonstrated that FC-CVD is a unique and versatile technique for the simultaneous growth of substrate-free 0D-fullerene, 1D-CNT and 2D-graphene. The formation of 0D-1D-2D carbon nanostructures were directly evidenced by lattice-resolved (scanning) transmission electron microscopy (STEM). We showed that the relative number density of graphene-nanoflakes can be tuned by optimizing the synthesis conditions. In addition, the as-synthesized hybrid films can be directly deposited on any surface at ambient temperature with an arbitrary thickness which offers a new route towards ultra-fast manufacturing and dry deposition of the hybrid structures.

Keywords floating-catalyst CVD; single-walled carbon nanotubes; pre-made catalyst; ethylene; transparent conducting film; low dimensional carbon nanostructures

ISBN (printed) 978-952-60-3795-0

ISBN (pdf) 978-952-60-3796-7

ISSN (printed) 1799-4934

ISSN (pdf) 1799-4942

Location of publisher Helsinki

Location of printing Helsinki **Year** 2020

Pages 126

urn <http://urn.fi/URN:ISBN:978-952-60-3796-7>

Acknowledgements

The research work presented in this thesis has been carried out in the Nano-Materials Group of the Department of Applied Physics, Aalto University School of Science in the years 2016-2019. I would express my deep gratitude towards my supervisor Prof. Esko I. Kauppinen for his excellent guidance, support, advice and his extensive network of collaborators which helped me a lot to finish my research work in a very short period of time. I feel myself very lucky that I got an opportunity to do my PhD research work under his supervision. The experience of working in his leadership in a relaxed, creative and scientific environment will benefit me for the rest of my life.

I give sincere thanks to my thesis advisor Dr. Qiang Zhang, for his valuable scientific advice, comments, and exchange of ideas. It was a very joyful experience to work with him. I owe special thanks to Dr. Hua Jiang for conducive scientific discussions and his support in doing transmission electron microscopy work in all my research publications. I am indebted to Dr. Kimmo Mustonen for his interest in carrying out scanning transmission electron microscopy measurements for my research work and for sparing his time for fruitful collaboration and the interpretation of the experimental results.

Thank you to all my co-authors, Dr. Patrik Laiho, Dr. Yongping Liao, Dr. Aqeel Hussain, Dr. Er-Xiong Ding, Dr. Jani Sainio, Dr. Mohammad Tavakkoli, Dr. Nan Wei, and Abu Taher Khan for their input into this thesis. Other members of the NanoMaterials Group, former and present, are also thanked for their contributions. I also want to thank many of my other friends studying or working at Aalto University. Thank you for your company in different social activities which have been always joyful for me. I acknowledge the support provided by administrative staff particularly by Reetta Lesonen, Marita Halme and Timo Kajava. This research has made extensive use of the Aalto University Nanomicroscopy Center and I am thankful to the staff for keeping equipment operational and helping us in making characterization process speedy.

Last but not the least, I wish my deep gratitude and thanks to my whole family, especially to my mother, brothers, wife and sons for their continuous unconditional love, patience, and support throughout my whole educational journey. Thank you all!

Espoo, 10 November 2019
Saeed Ahmad

Contents

Acknowledgements.....	i
Contents	iii
List of Abbreviations and Symbols.....	v
List of Publications.....	vii
Author's Contribution	viii
Other Featured Publications.....	ix
1. Introduction.....	1
2. Single-walled carbon nanotube structure and optical properties.....	3
2.1 Low-dimensional allotropes of carbon	3
2.2 Geometry of SWCNTs	4
2.3 Optical properties of SWCNTs.....	5
2.3.1 Optical absorption spectroscopy	5
2.3.2 Raman spectroscopy	6
2.4 Electronic properties of SWCNTs	8
3. Synthesis technique and experimental set-up	11
3.1 Carbon nanotubes synthesis techniques.....	11
3.2 Floating catalyst CVD technique.....	12
3.2.1 FC-CVD using <i>in-situ</i> catalyst particles	12
3.2.2 FC-CVD using pre-made catalyst particles	12
3.3 Roles of catalyst particles in SWCNTs synthesis	13
3.4 Synthesis with spark discharge generator	14
3.4.1 Spark discharge generation of catalyst particles.....	14
3.4.2 Designing novel rod-to-tube type SDG	14
3.4.3 Experimental set-up for SWCNTs synthesis.....	16
3.4.4 Carbon source decomposition and SWCNTs synthesis	17
3.4.5 Sample collection and deposition	18
3.5 SWCNTs based transparent conductive films	19
4. Characterizations	21

4.1	Differential mobility analysis	21
4.2	Optical spectroscopy.....	22
4.2.1	Uv-Vis-NIR absorption spectroscopy	22
4.2.2	Resonant Raman spectroscopy	23
4.3	Elemental analysis of SWCNTs film.....	23
4.4	Sheet resistance measurement	24
4.5	Electron microscopy	25
4.5.1	Scanning electron microscopy	26
4.5.2	Transmission electron microscopy	26
4.6	Atomic force microscopy	28
5.	Results and discussion	29
5.1	Gas-phase synthesis of time consistent catalyst particles.....	29
5.1.1	Material dependent electrode's evaporation	30
5.1.2	Tuning size and concentration of catalyst particles.....	30
5.1.3	Morphology and composition of catalyst particles.....	31
5.2	Catalyst composition effects on FC-CVD growth of SWCNTs.....	33
5.2.1	Optimization of the growth conditions	34
5.2.2	SWCNT yield dependence on catalyst composition	34
5.2.3	Catalyst composition effects on SWCNTs morphology	36
5.2.4	Tuning chirality of SWCNTs with catalyst composition	39
5.2.5	SWCNT-TCFs performance and catalyst composition.....	40
5.3	Improving conductivity of SWCNT-TCFs by sulfur addition..	41
5.3.1	Variation in yield and diameter of SWCNTs.....	42
5.3.2	Mechanism behind sulfur-assisted growth of SWCNTs	44
5.3.3	Change in morphology of SWCNTs with sulfur	46
5.3.4	Sulfur modulates the chirality of SWCNTs.....	47
5.3.5	Highly conductive SWCNT-films with sulfur addition.....	48
5.4	Simultaneous growth of 0D- 1D-2D carbon nanostructures ..	49
5.4.1	Morphology and structure of the hybrid material	49
5.4.2	Role of hydrogen.....	51
5.4.3	Universality of the growth process	52
6.	Conclusions and outlook.....	55
	References	57

Appendices

Publications I-IV

List of Abbreviations and Symbols

0D	zero-dimensional
1D	one-dimensional
2D	two-dimensional
A	absorbance
AFM	atomic force microscopy or microscope
c	concentration of the absorbing species
CAP	charged aerosol particle
CCD	charged coupled detector
CNT	carbon nanotubes
CPC	condensation particle counter
CVD	chemical vapor deposition
D	defective mode
d_b	mean bundle diameter of carbon nanotubes
D_{ME}	electrical mobility diameter
DMA	differential mobility analyser
EDPs	electron diffraction patterns
EDS	x-rays energy dispersive spectroscopy
EELS	electron energy loss spectroscopy
E_{11}^M	first inter-band transition in metallic nanotubes
E_{11}^S	first inter-band transition in semiconducting nanotubes
E_{22}^S	second inter-band transition in semiconducting nanotubes
FC-CVD	floating catalyst chemical vapor deposition
FCE	Faraday cup electrometer

G	graphitic mode
HAADF	high-angle annular dark-field
HR-TEM	high-resolution transmission electron microscope or microscopy
HWG	hot wire generator
ITO	indium tin oxide
L	optical path length
l_b	mean bundle length of carbon nanotubes
lpm	litre per minute
MFC	mass flow controller
MWCNT	multi-walled carbon nanotube
NC	number concentration
NSD	number size distribution
OAS	optical absorption spectra
ppm	part per million
RBM	radial breathing mode
R-T SDG	rod-to-tube type spark discharge generator
R_s	sheet resistance
sccm	standard cubic centimetre per minute
SDG	spark discharge generator
SEM	scanning electron microscope or microscopy
SMPS	scanning mobility particle sizer
SMPS+E	scanning mobility particle sizer with Faraday cup electrometer
SWCNT	single-walled carbon nanotube
STEM	scanning transmission electron microscope or microscopy
TCF	transparent conductive film
VLS	vapor liquid solid
XPS	x-ray photoelectron spectroscopy

List of Publications

This doctoral dissertation consists of a summary and of the following publications which are referred to in the text by their numerals

- I. Ahmad, Saeed;** Laiho, Patrik; Zhang, Qiang; Jiang, Hua; Hussain, Aqeel; Liao, Yongping; Ding, Er-Xiong; Wei, Nan; and Kauppinen, Esko I. 2018. Gas phase synthesis of metallic and bimetallic catalyst nanoparticles by rod-to-tube type spark discharge generator. Elsevier. *Journal of aerosol science*, volume 123, pages 208-218. ISSN: 0021-8502. doi.org/10.1016/j.jaerosci.2018.05.011
- II. Ahmad, Saeed;** Liao, Yongping; Hussain, Aqeel; Zhang, Qiang; Ding, Er-Xiong; Jiang, Hua; and Kauppinen, Esko I. 2019. Systematic investigation of the catalyst composition effects on single-walled carbon nanotubes synthesis in floating-catalyst CVD. Elsevier. *Carbon*, volume 149, pages 318-327. ISSN: 0008-6223. doi.org/10.1016/j.carbon.2019.04.026
- III. Ahmad, Saeed;** Ding, Er-Xiong; Zhang, Qiang; Jiang, Hua; Sainio, Jani; Tavakkoli, Mohammad; Hussain, Aqeel; Liao, Yongping; and Kauppinen, Esko I. 2019. Roles of sulfur in floating-catalyst CVD growth of single-walled carbon nanotubes for transparent conductive film applications. Elsevier. *Chemical engineering journal*, volume 378 (122010), pages 1-8. ISSN: 1385-8947. doi.org/10.1016/j.cej.2019.122010
- IV. Ahmad, Saeed;** Mustonen, Kimmo; McLean, Ben; Jiang, Hua; Zhang, Qiang; Hussain, Aqeel; Taher Khan, Abu; Ding, Er-Xiong; Liao, Yongping; Nasibulin, Albert G.; Kotakoski, Jani; Page, Alister J.; and Kauppinen, Esko I. Simultaneous growth of free-standing 0D-1D-2D carbon nanostructures through one-step gas-phase synthesis techniques. Submitted to *Nature* December-2019 (12 pages).

Author's Contribution

Publication I:

Gas phase synthesis of metallic and bimetallic catalyst nanoparticles by rod-to-tube type spark discharge generator.

The author conceived the idea, designed and built the spark discharge generator, conducted out all the experiments and characterizations except TEM measurements, analysed the data and wrote the manuscript.

Publication II:

Systematic investigation of the catalyst composition effects on single-walled carbon nanotubes synthesis in floating-catalyst CVD.

The author conceived the idea, designed and built the floating catalyst CVD reactor, conducted out all the experiments and characterizations except TEM measurements, analysed the data, and wrote the manuscript.

Publication III:

Roles of sulfur in floating-catalyst CVD growth of single-walled carbon nanotubes for transparent conductive film applications.

The author designed and built the experimental set-up, conducted out all the experiments and did all the characterizations except TEM and XPS measurements, analysed the data, and wrote the whole manuscript excluding XPS part.

Publication IV:

Simultaneous growth of free-standing 0D-1D-2D carbon nanostructures through one-step gas-phase synthesis techniques.

The author conceived the idea and modified the synthesis reactor, conducted out all the experiments and did all the characterizations except TEM, and STEM measurements, analysed the data, and wrote the initial draft of the manuscript excluding simulation part.

Other Featured Publications

The author has also contributed to the following publications:

- I. Tian, Ying; Wei, Nan; Laiho, Patrik; **Ahmad, Saeed**; Magnin, Yan; Liao, Yongping; Bichara, Christophe; Jiang, Hua; and Kauppinen, Esko I. 2019. Cutting-floating single-walled carbon nanotubes with a 'CO₂ blade'. Elsevier. Carbon, volume 143, pages 482-486. ISSN: 0008-6223. doi.org/10.1016/j.carbon.2018.11.035
- II. Hussain, Aqeel; Liao, Yongping; Zhang, Qiang; Ding, Er-Xiong; Laiho, Patrik; **Ahmad, Saeed**; Wei, Nan; Tian, Ying; Jiang, Hua; and Kauppinen, Esko I. 2018. Floating catalyst CVD synthesis of single walled carbon nanotubes from ethylene for high performance transparent electrode. The Royal society of Chemistry. Nanoscale, issue 10, pages 9752-9759. ISSN: 2040-3372. doi.org/10.1039/c8nr00716k
- III. Liao, Yongping; Hussain, Aqeel; Laiho, Patrik; Zhang, Qiang; Tian, Ying; Wei, Nan; Ding, Er-Xiong; Khan, Sabbir A; Nguyen, Nguyen Ngan; **Ahmad, Saeed**; and Kauppinen, Esko I. 2018. Tuning geometry of SWCNTs by CO₂ in floating-catalyst CVD for high-performance transparent conductive films. John Wiley and sons inc. Advanced materials interfaces, issue 5, 1801209. ISSN: 2196-7350. doi.org/10.1002/admi.201801209
- IV. Wei, Nan; Laiho, Patrik; Taher Khan, Abu; Hussain, Aqeel; Lyuleeva, Alina; **Ahmad, Saeed**; Zhang, Qiang; Liao, Yongping; Tian, Ying; Ding, Er-Xiong; Ohno, Yutaka; and Kauppinen, Esko I. 2019. Fast and Ultra-Clean Approach for Measuring the Transport Properties of Carbon Nanotubes. John Wiley and sons inc. Advanced Functional Materials, 1907150. ISSN: 1616-3028. doi.org/10.1002/adfm.201907150

1. Introduction

Single-walled carbon nanotubes (SWCNTs) are chemically derived synthetic allotropes of carbon having diameter of few nanometers, and length in the range from few micrometers to several centimeters. They have unique optical [1] and electronic [2,3] properties due to their quasi one-dimensional (1D) tubular structure and chirality dependent electronic band structure. They have large surface area to volume ratio having every atom exposed to the surface. SWCNTs can be either metallic or semiconducting (with varying band gaps) depending on the confinement of electrons wave functions around their circumference. SWCNTs have attracted widespread attention in nanoscale electronic and photonic devices due to their high electrical conductivity and charge carrier mobility [4,5]. Moreover, due to low refractive index [1], excellent mechanical flexibility, low haze [6] and optical transparency [7], SWCNT film is one of the most promising materials for the replacement of indium tin oxide (ITO) as transparent conductive films (TCFs) in future flexible electronics.

To fabricate SWCNT-TCFs, floating catalyst chemical vapor deposition (FC-CVD) is one of the most widely used technique for the large scale production of SWCNTs synthesis. However, in FC-CVD, a better control of SWCNTs morphology and structure is a big challenge for their potential applications. It is well-known that thermodynamically catalyst composition plays a vital role in the controllable synthesis of SWCNTs. In conventional FC-CVD methods, generally, catalyst particles are obtained by decomposition of volatile organometallic compounds [8,9] inside the FC-CVD reactor. It is worth mentioning that in all the approaches involving *in-situ* nanoparticle fabrication, it is hard to get full control of number concentration (NC), composition, size and structure of pure and mixed metallic nanoparticles. Moreover, the choice of catalyst composition is limited because of their toxic precursors.

To overwhelm the above-mentioned core issues of SWCNT synthesis by the FC-CVD method we decoupled the catalyst particle generation process from SWCNT growth. To produce highly time consistent and *ex-situ* catalyst particles in gas-phase having high purity in **publication-I**, we designed a novel rod-to-tube type spark discharge generator (R-T SDG), permitting a precise control of catalyst, and thus, SWCNT NC during growth [10]. Various monometallic and bimetallic catalyst particles were prepared from the physical evaporation of the electrode's material in the presence of non-reacting carrier gases. We found that our design i.e. R-T SDG can produce time stable, and a high NC of catalyst particles due to its comparatively long-term quasi-stability.

In **publication-II**, for the quantitative analysis of catalyst composition effects on various growth characteristics of SWCNTs the number size distribution (NSD) of catalyst particles (Fe, Co, Ni, Co-Fe and Co-Ni) in the gas phase were measured by using differential mobility analyzer (DMA) before feeding into the

FC-CVD reactor. We for the first time systematically studied the effects of catalyst composition on yield, morphology, conductivity and helicity of FC-CVD grown SWCNTs. Interestingly, we found that the mean diameter of as-produced SWCNTs (~ 1 nm) is independent of catalyst composition under the similar NSD of catalyst particles. However, the yield, morphology and SWCNTs film conductivity can be effectively tuned by changing catalyst composition [11]. Furthermore, from the unambiguous electron diffraction technique, we observed that the bimetallic Co-Ni catalyst can produce comparatively narrower chirality and diameter distribution of SWCNTs.

In **publication-III**, we utilized sulfur as an effective growth promotor to tune yield, structural properties and morphology of SWCNTs and to obtain high-performance SWCNT-TCFs. We found that the yield of SWCNTs is largely dependent on the amount of sulfur introduced into the FC-CVD reactor and catalyst composition. More importantly, at optimized conditions with sulfur, the opto-electronic performance of SWCNT-TCFs enhanced approximately three times [12]. The improvement in opto-electronic performance with the sulfur addition is the effect of an increase in the diameter of individual SWCNTs and their bundle length. Interestingly, the detailed atomic structure determination revealed that both SWCNTs with and without sulfur addition have wide chirality distributions spanning from zig-zag to armchair edges and sulfur promotor has little effect on chirality modulation of SWCNTs. Fig. 1.1 provides a brief summary of the publications included in this thesis in their sequential order.

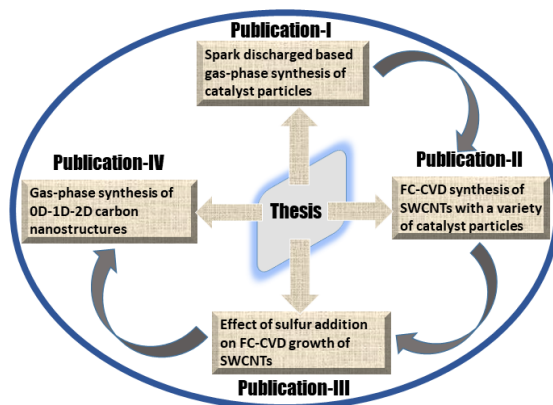


Fig. 1.1 A brief summary of the **publications-I to IV** included in the **thesis**.

In **publication-IV**, we developed a novel gas-phase and scalable method for the simultaneous growth of fullerene-CNT-graphene (0D-1D-2D) hybrid carbon nanostructures with various catalysts (Fe, Co, Ni, Co-Ni), carbon sources (C_2H_4 , CO, C_2H_5OH , CH_4) and various set-ups. We found that at the optimized conditions graphene nano flakes can grow directly from the pyrolysis of different carbon sources without any substrate. Since our method is purely in gas-phase therefore as-produced hybrid material can be deposited directly on any substrate with well-controlled thickness and transparency for further applications under ambient conditions. Our technique opens up new avenues towards the ultra-fast manufacturing of the 0D-1D-2D hybrid material at industrial scale and provides scientific community new insights into the synthesis mechanism of low dimensional carbon nanostructures, especially that of graphene.

2. Single-walled carbon nanotube structure and optical properties

2.1 Low-dimensional allotropes of carbon

Carbon has ground state electronic configuration $1s^2, 2s^2, 2p^2$ and has ability to make a long chain of carbon atoms by forming covalent C-C bonding. Carbon exists in different allotropic forms and interestingly properties of its various allotropes, not only governed by the nature of chemical bonding but also depend on their dimensionality (i.e. quantum confinement of wave function describing behaviors of electrons). Recently, low-dimensional allotropes of carbon, especially fullerene, carbon nanotubes, graphene and their mixed-dimensional hybrid have attracted tremendous research interest due to their widespread potential, technological applications in various fields. Although, all the above mentioned low-dimensional allotropes have sp^2 bonded carbon atoms and each carbon atom is bonded with the other three carbon atoms (Fig. 2.1) but they differ in electronic band structure due to quantum confinement in 1, 2 or 3 dimensions. Fullerenes (Buckyballs) are the spherical or ellipsoidal shaped molecules of carbon having different sizes and are 0D nanostructures. They have a band gap under ambient conditions [13] and can show metallic behavior if they are properly doped [14].

Carbon nanotubes (CNTs) are 1D cylindrical-shaped molecules of carbon and are considered to form by rolling a piece of graphene sheet. Depending on the number of graphene sheet layers CNTs can be divided into either single-walled (SWCNTs) or multi-walled carbon nanotubes (MWCNTs). It's worth mentioning that generally, the electronic and optical properties of CNTs and particularly of SWCNTs are highly sensitive to their diameter and specific molecular structure. Therefore, SWCNTs have remained a subject of great research interest in material science, electronics and photonics. They are topic of interest in this thesis.

On the other hand, one atom thick planar 2D carbon nanomaterial is graphene and it has a honeycomb crystalline lattice structure that consists of six-membered carbon rings. It is a zero band-gap semimetal and thinnest material known to human beings. It is the only form of carbon in which each atom is available for the chemical reaction from upper and bottom sides of the layer. Graphene is the basic structural element of some of the highly stimulating allotropes of carbon i.e. 0D-fullerene, 1D-CNT and 3D-graphite. Therefore, for the fundamental understanding of the structure and properties of fullerenes, graph-

ite and CNTs, graphene has always been considered as parent material. However, the high-quality, scalable, free-standing and single-step manufacturing of the graphene is still needed to achieve.

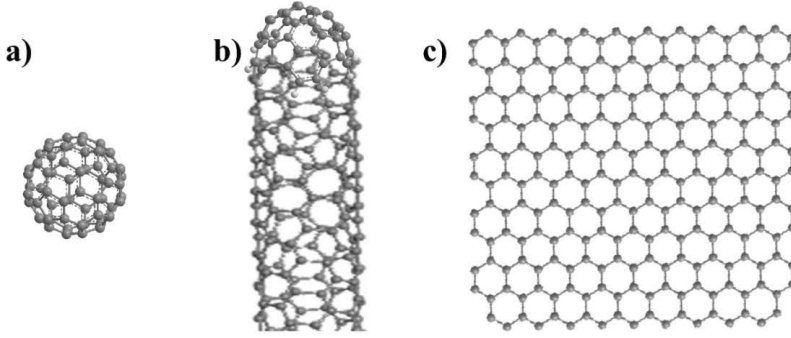


Fig. 2.1 Various low-dimensional allotropes of carbon **a)** fullerene (0-dimensional) **b)** a single-walled carbon nanotubes (1-dimensional) **c)** a graphene sheet (2-dimensional).

2.2 Geometry of SWCNTs

Conceptually a SWCNT is constructed by rolling a graphene sheet into a narrow hollow cylinder having a diameter in the nanoscale regime. In Fig. 2.2, a flat graphene lattice has been shown which can be rolled up to get SWCNT. The vector \mathbf{T} which is directed along the nanotube axis is known as translational vector and determines the length of SWCNT. The chiral vector (\mathbf{C}_h) which determines the arrangement of carbon atoms along the circumference of SWCNT fully defines the geometry of a SWCNT and is normal to \mathbf{T} . Both \mathbf{T} and \mathbf{C}_h together define unit cell of a carbon nanotubes. \mathbf{C}_h is expressed in terms of two real space, unit base vectors of the graphene \mathbf{a}_1 and \mathbf{a}_2 , whose graphical depiction is provided in Fig. 2.2.

$$\mathbf{C}_h = n\mathbf{a}_1 + m\mathbf{a}_2 \quad (2.1)$$

Where (n, m) are positive integers and $n \geq m$ and they are known as chiral indices of a SWCNT. In real space the unit base vectors of graphene \mathbf{a}_1 and \mathbf{a}_2 are expressed as in Eq. 2.2.

$$\mathbf{a}_1 = (\sqrt{3}/2 a, a/2), \quad \mathbf{a}_2 = (\sqrt{3}/2 a, -a/2) \quad (2.2)$$

Where $\langle \mathbf{a}_1 \rangle = \langle \mathbf{a}_2 \rangle = a = \sqrt{3} a_{cc}$, and a_{cc} is the distance between two adjacent carbon atoms in graphene lattice separated by 1.42 Å [15,16]. The diameter of a SWCNT is positively correlated to its chirality i.e. (n, m) by the following relation.

$$d_t = \langle \mathbf{C}_h \rangle = a\sqrt{n^2 + m^2 + nm} \quad (2.3)$$

The angle θ between \mathbf{C}_h and \mathbf{a}_1 is known as chiral angle, and for all possible combinations of n and m, it lies in the range $0 \leq \theta \leq 30^\circ$. The chiral angle can be defined in terms of chirality (n, m) of SWCNT as,

$$\theta = \cos^{-1}(\mathbf{C}_h \cdot \mathbf{a}_1 / \langle \mathbf{C}_h \rangle \langle \mathbf{a}_1 \rangle) = \cos^{-1} \left(2n + m/2\sqrt{n^2 + m^2 + nm} \right) \quad (2.4)$$

In Eq. 2.4, for non-zero n, if $m=0$, then $\theta=0^\circ$ and such type of carbon nanotubes are referred as zig-zag nanotubes (see Fig. 2.2). If ($n \neq m$) then $0^\circ < \theta < 30^\circ$ and nanotubes are chiral and if ($n=m$), then $\theta=30^\circ$ and nanotubes are armchair. Furthermore, depending on the cutting direction and size of the graphene sheet

from which a SWCNT is constructed, SWCNT can be either semiconducting or metallic. As a rule of thumb SWCNTs are metallic if $(n-m)/3$ is a whole integer and semiconducting if $(n-m)/3$ is not a whole integer.

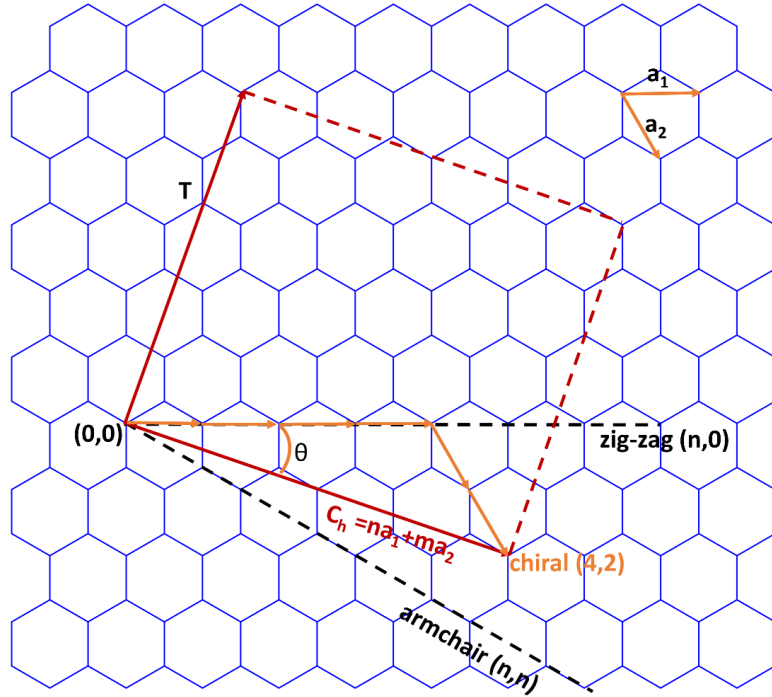


Fig. 2.2 The unrolled honeycomb lattice of a carbon nanotube. The chiral vector C_h of $(4, 2)$ SWCNTs and its translation vector T . The chiral angle has been indicated by θ and a_1 and a_2 are the real space unit vectors of hexagonal graphene lattice.

2.3 Optical properties of SWCNTs

Optical absorption (UV-Vis-NIR) and Raman spectroscopy are two useful optical techniques for the fast characterization of the diameter, quality, chirality, and metallic or semiconducting nature of a SWCNT sample. In the following sections, their working principle is briefly discussed.

2.3.1 Optical absorption spectroscopy

When electromagnetic radiations pass through an absorbing medium like SWCNTs, their intensity attenuates depending on the absorption coefficient (α), optical path length (L) and concentration (c) of the absorbing species [17]. The optical absorption spectroscopy measures attenuation in the intensity of electromagnetic radiations as a function of their frequency or wavelength. For the characterizations of SWCNTs, the relevant wavelength ranges from 200-2600 nm. Mathematically, attenuation in the intensity of electromagnetic radiations is an exponentially decaying function and is governed by Beer-Lambert law.

$$I = I_0 e^{-\alpha L c} \quad (2.5)$$

From Eq. 2.5, by measuring the relative intensity of transmitted light (I) at a particular frequency or wavelength with respect to the incident intensity (I_o) we can measure the absorbance (A) by the Eq. 2.6.

$$A = -\ln(I/I_o) \quad (2.6)$$

It's worth mentioning that unlike 3D solids, a typical optical absorption spectra (OAS) of SWCNT film contains sharp electronic-transitions peaks due to 1D nature of carbon nanotubes. The peaks in OAS arise from symmetric transition between van Hove singularities from i -th conduction to valance band and are denoted by E_{ii} (Fig. 2.3a and b) [18]. Optically, momentum conservation does not favor transitions from i -th valance to j -th conduction band or vice versa and they do not contribute much in OAS. A typical OAS of SWCNT film in the UV-Vis-NIR range has been shown in Fig. 2.3d. It contains three pronounced characteristic peaks associated with first optical-transition in semiconducting tubes (E_{11}^S), second transition in semiconducting tubes (E_{22}^S), and first transition in metallic nanotubes (E_{11}^M) [15,19]. Theoretically, it is a fact that a SWCNT has a very sharply peaked density of states [18], but experimentally (see Fig. 2.3d), it has been found that OAS of SWCNT film is broad due to heterogeneity of (n, m) in the sample. The energy of these optical transitions in a SWCNT is inversely proportional to the nanotube diameter and the mean diameter of SWCNTs bulk sample can be estimated by combining the energy of these transitions with the Kataura plot (Fig. 2.3c) [19–21].

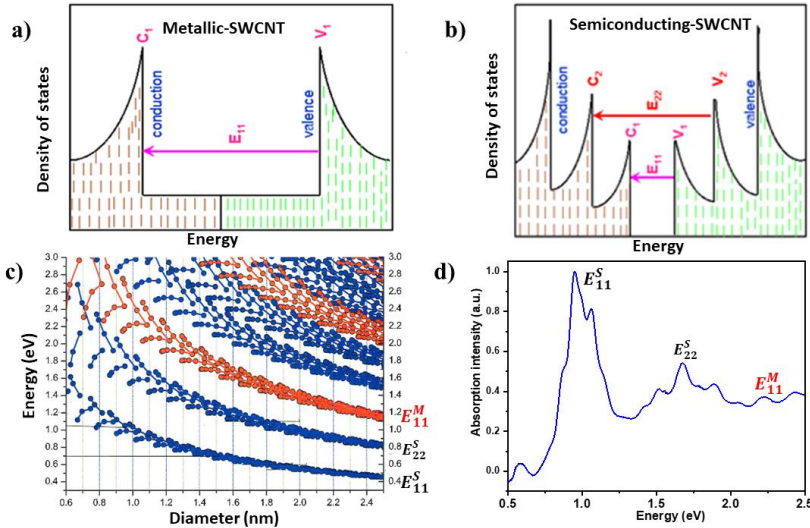


Fig. 2.3 Optical transitions in **a)** metallic-SWCNT **b)** semiconducting-SWCNT (transitions adapted from Wikipedia Commons as public domain [18]) **c)** Kataura plot of SWCNTs based on extended tight-binding approximation [20] showing E_{11}^S , E_{22}^S and E_{11}^M transitions. Each blue dot corresponds to one transition state of a specific diameter semiconducting-SWCNT and red dot of metallic-SWCNT. **d)** Typical absorption spectra of a SWCNT film having E_{11}^S , E_{22}^S and E_{11}^M transition peaks.

2.3.2 Raman spectroscopy

Raman spectroscopy is based on inelastic scattering of monochromatic light (laser), when it interacts with a sample under investigation and is usually used for the quantitative analysis and to know the structural fingerprint of the sample.

In Raman spectroscopy, photons of electromagnetic radiations on interaction with the sample are absorbed by the molecules of the sample and are re-emitted. The frequency of re-emitted photons is shifted up or down compared to the photons of incident light depending on the quantized vibrational or rotational energy levels (phonons) in the molecules and is known as Raman shift. Hence, detecting the frequency of scattered photons compared to the incident photons provides information about the elastic arrangement of atoms/molecules in the sample. Plotting intensity of the scattered light as a function of frequency down-shift of the scattered light gives us Raman spectra of the sample and hence, we acquire information of the phonon frequencies of the material depending on the vibrational energy levels of different functional groups [22]. However, the energy of a very small fraction roughly $10^{-5}\%$ of the total incident photons is exchanged in this interaction and the rest of the photons are elastically scattered. The probability of Raman shift increases by a factor of $\sim 10^3$ if the transition energy of either the absorbed or the re-emitted photon resonates with an electronic transition state of the molecule and this process is referred as resonant Raman spectroscopy.

Typically, the Raman spectra of a SWCNT consists of several characteristic peaks. The dominant peak at around 1582 cm^{-1} (Fig. 2.4b) originating from the in-plane vibrations in graphene lattice, reflecting the graphitic nature of SWCNTs is known as G band [22]. However, due to curvature in SWCNTs, G mode further splits into G^+ and G^- sub-bands representing vibrations along the nanotube axis and circumferential direction respectively. It's worth mentioning that G band excitation is 1st-order Raman scattering process (arising from one scattering event) but 2nd-order Raman scattering (arising from two scattering events) can also occur if excited phonons are scattered by defects or disorder structures in the crystal lattice. This is known as D mode and appears around 1350 cm^{-1} in Raman spectra of SWCNTs as has been indicated in the form of a hump in Fig. 2.4b.

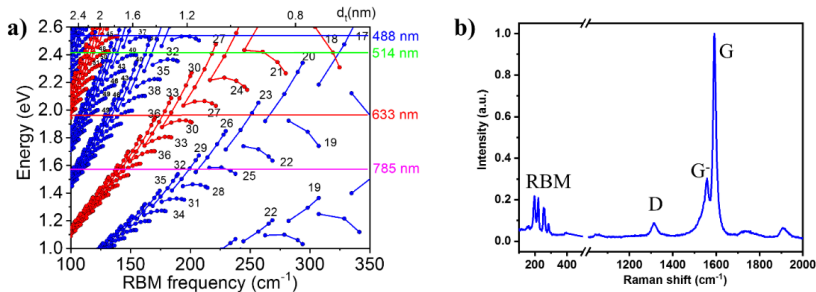


Fig. 2.4 a) Kataura plot of SWCNTs based on extended tight-binding approximation [20]. The numbers on blue lines and red lines indicate $2n+m$ family of semiconducting and metallic SWCNTs respectively, whereas corresponding dots represent specific chirality of a SWCNT. Four widely used excitation wavelengths i.e. 488, 514, 633 and 785 nm are shown by horizontal lines. **b)** A typical Raman spectrum of SWCNT film showing the most important features like radial breathing mode (RBM) in the region $<400\text{ cm}^{-1}$, G (1582 cm^{-1}) and D (1350 cm^{-1}) bands.

The last major feature in Raman spectra of SWCNTs is radial breathing mode (RBM) which lies roughly below 400 cm^{-1} and is only observed in double or single-walled carbon nanotubes. It arises from the out-of-plane vibrational modes in the crystal lattice and is attributed to the radial expansions and contractions in the SWCNTs. The RBM is a resonant Raman mode and it has been found that

the RBM frequency (ω_{RBM}) is inversely proportional to the diameter (d_t) of SWCNTs. Because of its dependence on SWCNTs diameter, the RBM is usually combined with the Kataura plot (Fig. 2.4a) [15,21,22] to characterize diameter, family (2n+m) and chirality of SWCNTs. However, Raman measurement can only activate SWCNTs having bandgap in resonance with a specific excitation laser and it can reveal structural information of only that kind of SWCNTs in the sample. Therefore, the complete Raman-characterization of SWCNT sample requires a tunable laser system that can provide different excitation lasers.

2.4 Electronic properties of SWCNTs

The electronic band structure of a material mainly determines electrical transport properties in the material. Interestingly, the electronic properties of SWCNTs depend on the orientation of hexagons along the nanotubes axis and can be described using the energy dispersion relation of graphene. In graphene, each carbon atom has four bonds, three σ -bonds (arising from 2s, 2p_x, 2p_y electrons) with each of its adjacent carbon atoms in the same plane and one π -bond (arising from 2p_z electron) oriented out of the plane. It is worth noting that the overlap between in-plane atomic orbitals (i.e. 2s, 2p_x, 2p_y) and the out of plane atomic orbital (2p_z) is zero. Therefore, the electron in 2p_z orbital can be treated independently. Moreover, the out of plane π -electrons of adjacent carbon atoms hybridize together to form the half-filled π - and π^* -bands which are responsible for the extraordinary electronic properties of the graphene [19]. The electronic band structure of π -orbitals of graphene can be calculated from tight-binding approximation where the conduction and valance band touch each other at the six corners of Brillouin zone (i.e. K and K' points) with nearly continuous variation along (k_x , k_y) plane.

$$E_{2D}(k_x, k_y) = \pm \gamma_0 \sqrt{\left[1 + 4 \cos\left(\frac{\sqrt{3}}{2} k_x a\right) \cos\left(\frac{k_y a}{2}\right) + 4 \cos^2\left(\frac{k_y a}{2}\right) \right]} \quad (2.7)$$

Where γ_0 is the nearest neighbor transfer integral and plus minus prefixes are for conduction and valance band respectively, whereas a is hexagonal lattice constant. The electronic band structure of SWCNTs is obtained by further quantization of 2D graphene sheet into 1D structure and imposing appropriate boundary conditions around the circumference of SWCNT. For a SWCNT of infinite length, the wave vector ($k_{||}$) in the direction of translation vector \mathbf{T} (Fig. 2.2) along SWCNT axis is continuous. However, the wave vector (k_{\perp}) around the circumference of SWCNT i.e. along chiral vector \mathbf{C}_h , becomes quantized [23]. Hence, cross-sectional cutting of the energy dispersion relation of graphene for allowed values of k_{\perp} gives us the band structure of SWCNTs. The cross-sectional sub-bands sliced from the dispersion of graphene are shown in Fig. 2.5 [24].

The 1D dispersion relation for j th sub-band of SWCNT is

$$E_j(k) = \pm \left[\left(\frac{\hbar}{2\pi} v_F k \right)^2 + \left(\frac{E_j^g}{2} \right)^2 \right]^{1/2} \quad (2.8)$$

Where E and k are distances from the center point of graphene dispersion cone in units of energy and wave vector. v_F is the Fermi velocity and the E_j^g is the j th

energy gap determined by the distance to nearest K point. For a specific (n, m) , if the cutting line passes through a K point of Brillouin zone then the energy bandgap is zero (Fig. 2.5b), and therefore SWCNTs are metallic.

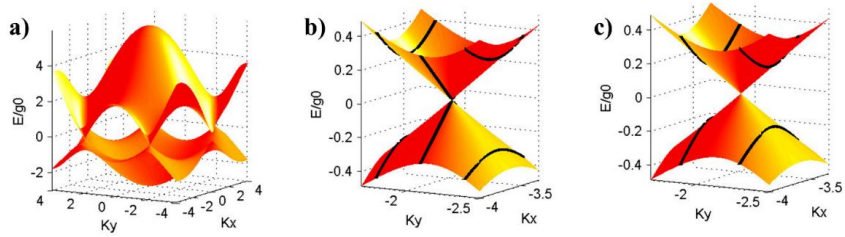


Fig. 2.5 **a)** The band structure of SWCNTs derived from energy dispersion relation of graphene where the valance and conduction bands are touching at the six corner of first Brillouin zone (K and K' points) **b)** The electronic band structure of metallic SWCNTs **c)** The diameter-dependent electronic band structure of semiconducting SWCNTs has been indicated by the distance of black cutting lines from K point (adapted from Wikipedia Commons as public domain [24]).

On the other hand, if the cutting line does not pass through a K point (Fig. 2.5c), then the SWCNT is semiconducting having a finite energy gap between the valence and conduction band. However, at the moment the well-controlled, scale-able synthesis of either pure metallic or semiconducting SWCNTs with a specific molecular structure has not been achieved which limits their applicability especially, in micro- and nano-electronic devices. On the other side, a complete control on SWCNT molecular structure is not needed in many other applications, such as in SWCNT-TCFs and CNTs composite materials. Therefore, keeping in mind the future industrial needs of SWCNTs, a lot of research efforts has been made for the production of SWCNTs on the industrial scale. A brief description of the most important processes tried so far is provided in **chapter 3**.

3. Synthesis technique and experimental set-up

3.1 Carbon nanotubes synthesis techniques

Since carbon nanotubes discovery in 1991 by Sumio Iijima [25], in the first few years, physical methods such as arc-discharge [25] and laser ablation [26] have been mainly utilized for their synthesis. In physical methods, the amount of carbon required for SWCNT growth is produced by physical evaporation of graphitic carbon alloyed with Ni or/and Co catalyst precursor. These processes are carried out in the presence of high temperature (~ 1200 °C) and a high-energy input is required to release carbon atoms from the target, which limits their practical application. Moreover, to obtain high quality and large-scale production of CNTs from physical methods were also highly challenging.

Synthesis of CNTs became simpler when in 1996 Richard Smalley and his coworkers at Rice University developed a chemical vapor deposition (CVD) method for the synthesis of SWCNTs. They produced SWCNTs by catalytic decomposition of carbon monoxide on pre-made molybdenum nanoparticles supported by temperature resistant substrate inside a heated reactor [27]. Later on, the CVD technique has been extensively employed for the production of SWCNTs and MWCNTs using a variety of carbon feedstocks and catalyst particles. Apart from CO typical hydrocarbons feedstock include methane (CH_4), ethylene (C_2H_4), acetylene (C_2H_2), benzene (C_6H_6), toluene (C_7H_8) and ethanol ($\text{C}_2\text{H}_5\text{OH}$). Whereas, typical catalyst particles include transition metals (Fe, Co, Ni, W and their alloy) [28,29], noble metals (Au, Ag, Cu) [30] and silicon dioxide (SiO_2) [31]. It has been observed that the proper choice of catalyst particles and their morphology plays a significant role in controlling the amount of SWCNTs and MWCNTs during synthesis. In addition, the morphology of as-produced CNTs greatly depends on the nature and size of catalyst particles. Despite the several advantages of the CVD method, being a batch-to-batch process achieving the repeatability of the similar CNTs samples is a major problem with CVD growth. Furthermore, in the CVD method, the catalysts particles are needed to synthesize and reduce before CNT growth on the substrate, which makes this multi-step method tedious. Moreover, the interactions between catalyst particles and temperature resistant support (such as MgO and Al_2O_3) make the synthesis process more complicated [32] resulting in as-grown CNTs sample hard to transfer. Therefore, scientists developed substrate free method for the large scale production of CNTs and this method has been discussed in following sections.

3.2 Floating catalyst CVD technique

Floating catalyst chemical vapor deposition (FC-CVD) is a single-step, continuous, scalable method in which the entire process of catalyst and SWCNTs formation takes place in a gaseous environment [9,33]. The aerosol nanoparticles suspended in non-reacting carrier gases without any support act as catalyst particles. In FC-CVD, the catalyst required for SWCNTs growth can be prepared inside the FC-CVD reactor (*in-situ* technique) or outside the FC-CVD reactor (pre-made catalysts) (Fig. 3.1). However, in both cases, catalytic decomposition of carbon feedstock and hence the growth of SWCNTs takes place inside the FC-CVD reactor in the presence of high temperature typically in the range from 700 to 1200 °C. Since in FC-CVD the formation of the SWCNTs take place in gas-suspension, the as-synthesized CNTs can be directly deposited on any surface in ambient temperature with an arbitrary thickness. This makes FC-CVD a highly promising technique for the large scale production and deposition of CNTs at industrial scale.

3.2.1 FC-CVD using *in-situ* catalyst particles

In-situ catalyst fabrication is the most commonly used approach for the FC-CVD growth of SWCNTs. In this technique, catalyst particles are obtained from thermal decomposition of volatile organometallic chemical precursors, such as ferrocene, nickelocene [8] and iron pentacarbonyl [34] in the presence of high temperature inside the FC-CVD reactor (Fig. 3.1a). The catalyst precursors and carbon feedstock are simultaneously introduced in the synthesis reactor. Unfortunately, in this conventional method due to the *in-situ* nucleation of catalyst particles, it is hard to get full control on composition, NC, size and structure of pure and mixed metallic nanoparticles. Therefore, this is not a reliable technique for the quantitative comparison of the catalyst composition, size and NC effects on CNTs growth. Moreover, the choice of catalyst composition is limited because of their highly toxic precursors.

3.2.2 FC-CVD using pre-made catalyst particles

Our group first time introduced the synthesis of SWCNTs in FC-CVD technique from pre-made catalysts. The purpose of pre-made catalyst synthesis is to get a precise control on size and NC of catalyst, and thus, SWCNT NC during growth [10,33]. In this technique, catalyst particles are pre-produced through the physical evaporation of the electrodes using hot wire generation (HWG) [9] or spark discharge generation techniques [33] (Fig. 3.1b). The size and NC of catalyst particles can be measured in real-time in the gas phase using a differential mobility analyzer (DMA) before feeding into the FC-CVD reactor. Therefore, these are reliable techniques for the comparative study of the catalyst composition, size and concentration effect on SWCNT synthesis. One drawback of HWG is that it is based on resistive-heating of metallic thin-wire and resistance of thin-wire changes with the increase in temperature. Therefore, it can hardly deliver constant power for material evaporation and the result is a shift in particle size distribution over the time. On the other hand, spark discharge generation is a versatile, cost-effective, simple and scale able technique for producing metallic and mixed metallic nanoparticles [35] which can give relatively more

time stable and narrow size distribution of nanoparticles for a longer time. The ease of producing bimetallic particles with two different metal electrodes is another advantage of using spark discharge generation rather than HWG. Therefore in this thesis, we utilized spark discharge generation technique for the synthesis of catalyst and hence SWCNTs synthesis.

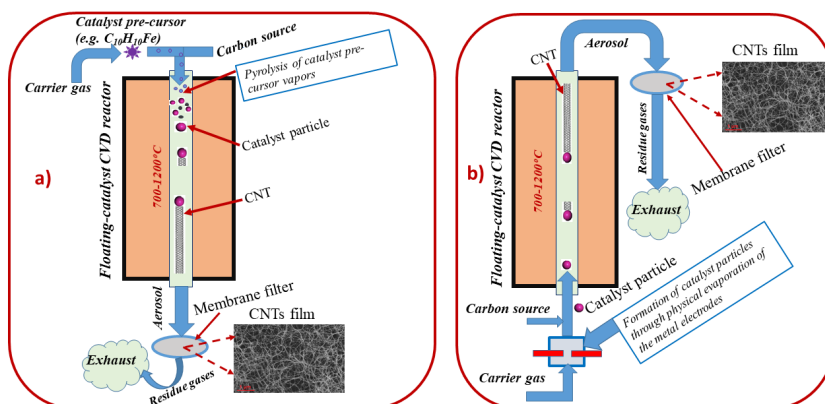


Fig. 3.1. General mechanism of growth of SWCNTs by floating-catalyst chemical vapor deposition using **a)** in-situ synthesized catalyst particles and **b)** pre-made catalyst particles.

3.3 Roles of catalyst particles in SWCNTs synthesis

Transition metal nanoparticles are widely used as a catalyst for the synthesis of SWCNTs because they are easily available, comparatively cheaper, and more efficient for SWCNT growth. However, a few research works have also reported the growth of SWCNTs from metal oxide [31,36] and semiconducting nanoparticles [37]. Various catalyst nanoparticles have different catalyzing activity towards the decomposition of the carbon precursors because the surface activity of the catalyst particle is generally associated with its both morphology and chemical composition. Ultimately, the properties of as-grown SWCNTs are highly dependent on the nature of the catalyst. Generally, it is believed that SWCNTs growth from metal nanoparticles is through a vapor-liquid-solid (VLS) mechanism [38,39]. According to the VLS model, firstly carbon-containing molecules are adsorbed on the surface of metal catalysts and are catalytically dissociate into atomic carbon. In the second step, carbon dissolves into the metal catalyst to form a liquid metal-carbon alloy and carbon diffuses from the liquid particle. In the third step, due to the super-saturation of dissolved carbon on the surface of the metal-carbon alloy, carbon starts to precipitate to form the cap of SWCNTs [38,39]. Hence, apart from playing the major role in decomposing carbon source, the catalyst also provides nucleation sites for the growth of the cap of SWCNTs. Since it is a fact that the structure of the cap of SWCNT determines the chirality of the nanotube, therefore, the morphology and structure of SWCNTs are highly dependent on the morphology and nature of the catalyst particle. However, the effect of growth conditions (temperature, pressure, carbon precursor, reaction intermediates and residence time) cannot be ignored because the change in growth conditions will directly influence carbon solubility and surface activity of the catalyst particles.

3.4 Synthesis with spark discharge generator

Spark discharge generation technique for SWCNTs synthesis utilizes an *ex-situ* spark discharge generator (SDG) for well-controlled and cost-effective gas-phase production of highly pure catalyst particles [35]. Catalyst particles are carried from SDG to the FC-CVD reactor by the carrier gas for the synthesis of SWCNTs.

3.4.1 Spark discharge generation of catalyst particles

In spark discharge generation technique two metal electrodes are used as a catalyst precursor on which a high voltage of the order of few kV is applied in the presence of inert or non-reacting carrier gas. The electrical circuit to provide high voltage consists of a power source, ballast resistor, inductor, and a high voltage capacitor (Fig. 3.2). The power source delivers a constant current to recharge the capacitor and when the voltage across the capacitor reaches the discharge voltage of the carrier gas, the dielectric breakdown of the gas occurs. The dielectric breakdown of the carrier gas forms a conducting plasma channel between the electrodes. During spark time local temperature is almost in the range 20,000 K to 30,000 K. This plasma evaporates the electrode material and then within a few microseconds spark in the electrode's gap disappears [35]. After the super saturation of the gap with the evaporated material nucleation of primary particles takes place. The primary particles cool down to room temperature due to adiabatic expansion after the spark is over and forms nanoparticles through gas-phase collisions. On the other hand due to adiabatic expansion of the aerosol, ions recombine to form neutral gas again. The nanoparticles are carried out from the electrode's gap by the carrier gas.

The size and morphology of spark-produced nanoparticles depend on many parameters like nature and flow rate of the carrier gas, the distance between electrodes, applied voltage, discharge frequency, and size and configuration of the electrodes etc. The electrode's configuration mainly determines the flow pattern (i.e. axial or transverse) of the carrier gas and jet speed at the point of spark generation. Conventional rod-to-rod (R-R) electrode configuration with the transverse flow of the carrier gas was previously employed by Mustonen et al. for the synthesis of SWCNTs [33]. However, it has been observed that at higher NC agglomeration of the nanoparticles is a major problem for less than 40 lpm of the carrier gas with this geometry. Therefore, they utilized 45 lpm nitrogen in SDG as a carrier gas to achieve suitable catalyst size (roughly < 5 nm) for SWCNTs synthesis. However, out of 45 lpm only 0.25 lpm (0.06%) was introduced into the FC-CVD reactor for SWCNTs growth and the remaining flow was guided to exhaust. Moreover, Mustonen et al. only utilized spark-produced Fe catalyst nanoparticles for SWCNTs growth.

3.4.2 Designing novel rod-to-tube type SDG

In **publication-I**, to obtain higher NC of catalyst particles with a small flow rate (< 2 lpm) of the carrier gas and for more time consistent generation of catalyst particles without degradation of the shape of the electrodes, we designed a novel rod-to-tube type SDG (R-T SDG) [10]. The major change in the design comes from the shape of the electrodes and flow pattern (i.e. axial) across the

spark discharge generation point. Instead of conventional R-R configuration (Fig. 3.2a), we utilized a metal rod and a metal tube as electrodes, where the tube electrode was also employed as an exit for the aerosol particles (Fig. 3.2b). The axial flow at spark discharge generation point provides much faster transport speed to the aerosol particles compared to transverse flow [40] reducing agglomeration probability of nanoparticles. The transport speed in the flow range 1 to 45 lpm for R-T configuration having rod diameter 2.4 mm and tube internal diameter 2.6 mm is in the range 7.9-373 m/s. On the other hand, for R-R configuration having diameter 2.5 mm in the same flow range is 3.3-152 m/s. Hence, axial flow is capable of producing less-agglomerated catalyst particles compared to transverse counterparts under the similar experimental conditions.

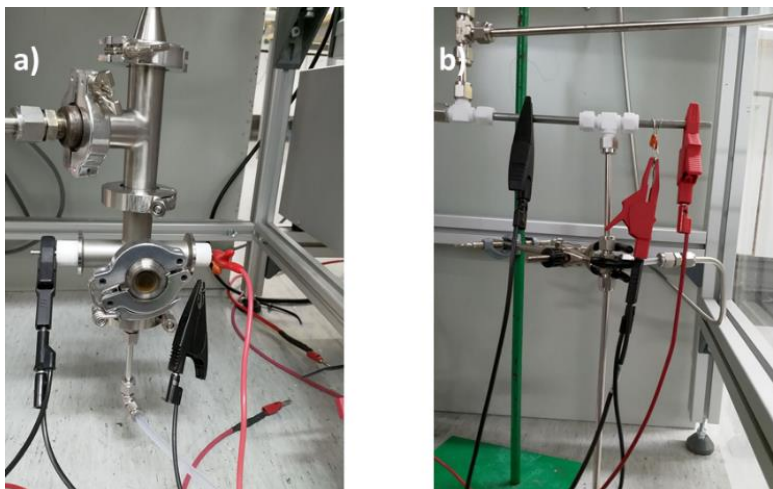


Fig. 3.2. Image of **a)** conventional rod to rod (R-R) electrodes configuration having a set of reducers at the inlet and outlet of the spark chamber and **b)** newly built rod to tube (R-T) electrodes configuration having very simple and compact size of spark chamber.

The detailed schematic of R-T SDG is shown in the Fig. 3.3. The two major parts of any kind of spark discharge generator are spark chamber and an electrical feedback circuit. For electrical insulation and to make SDG of compact size, we used polytetrafluoroethylene (PTFE) tee as the chamber. Rod and tube electrodes were fixed in two opposite sides of the tee and carrier gas was introduced from the third side of the tee. Using different combinations of electrode's material we synthesized various monometallic (Fe, Co, Ni, and Cu) and bimetallic (Co-Fe, and Co-Ni) catalyst nanoparticles. The energy required to produce periodic sparks across the electrodes gap was provided by a high voltage external capacitor (C_{ext}) (0.1-1 nF) connected parallel to the electrodes gap. For charging external capacitor a high voltage power source (HV) (Heinzinger PNC 20000-10 ump) through 1 M Ω ballast resistor (R) was employed. A mass flow controller (Aalborg GFC37 (N₂)) regulated the flow rate of carrier gas inside the spark chamber. In **publication-I**, flow rate of nitrogen or argon in R-T SDG was varied in the range 0.5-3.3 lpm to study the effects of carrier gas flow on catalyst size and NC. However, in **publications-II, III and IV** for the synthesis of SWCNTs, nitrogen was used as a carrier gas in the range 1.5-2 lpm. Hence, R-

T SDG owing to its improved design consumes roughly less than 10% of the carrier gas compared to the conventional R-R SDG for the synthesis of catalyst particles.

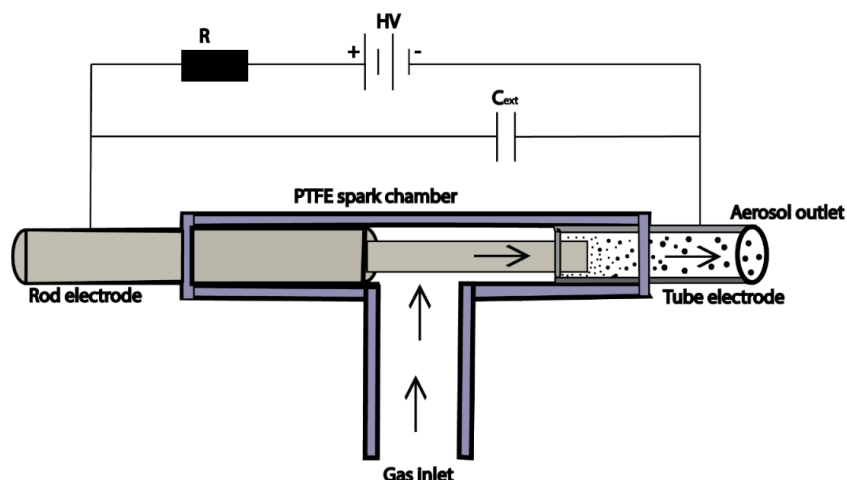


Fig. 3.3. Rod to tube type spark discharge generator (SDG) for producing time consistent, high number concentration (NC) and small-sized monometallic and bimetallic nanoparticles under a small flow rate of the carrier gas. The rod electrode is connected to the positive terminal of the high voltage source through a ballast resistor and the tube electrode was grounded. Polytetrafluoroethylene Swagelok tee was used as SDG chamber. Copyright © 2018 Elsevier [10], used with permission.

3.4.3 Experimental set-up for SWCNTs synthesis

For the synthesis of SWCNTs, various spark generated catalyst particles were introduced in FC-CVD reactor. The FC-CVD reactor consists of a quartz tube (inner diameter 22 mm) vertically placed inside a 90 cm high temperature furnace (Fig. 3.4). In **publication-I** 200 sccm of N₂ (99.995%) or Ar (99.995%) containing Fe catalyst particles were introduced into the FC-CVD reactor along with 250 sccm CO (99.999%, AGA) as carbon source and 50 sccm H₂ (99.999%, AGA). The temperature of the furnace was set at 880 °C. The two major problems of using CO as a carbon source are its low conversion rate and high toxicity.

Therefore, in **publications-II, III and IV** ethylene (C₂H₄) (99.999%, AGA) in the flow range 0.1-0.4 sccm (200-800 ppm) was used as carbon source along with optimum H₂ concentrations in the range 50-120 sccm at set furnace temperature of 1050 °C. In **publication-II**, effects of catalyst composition on SWCNTs synthesis were systematically studied using various monometallic (Fe, Co, Ni) and bimetallic (Co-Fe, Co-Ni) catalyst particles. In **publication-III** and **IV**, monometallic Fe and Co were employed as catalyst particles and H₂S (0.01 vol. % H₂S in N₂, 99.999%, AGA) in the range 0-10 ppm was used as a growth promoter. In all the cases, the total gas flow inside the FC-CVD reactor was 500 sccm and average residence time in the SWCNTs growth region is about 10 seconds. The complete experimental set-up for SWCNTs growth including schematic for gas flows, arrangement for gas-phase measurement of catalyst and SWCNTs NC by differential mobility analyzer (DMA), and temperature profile of the FC-CVD reactor is shown in Fig. 3.4.

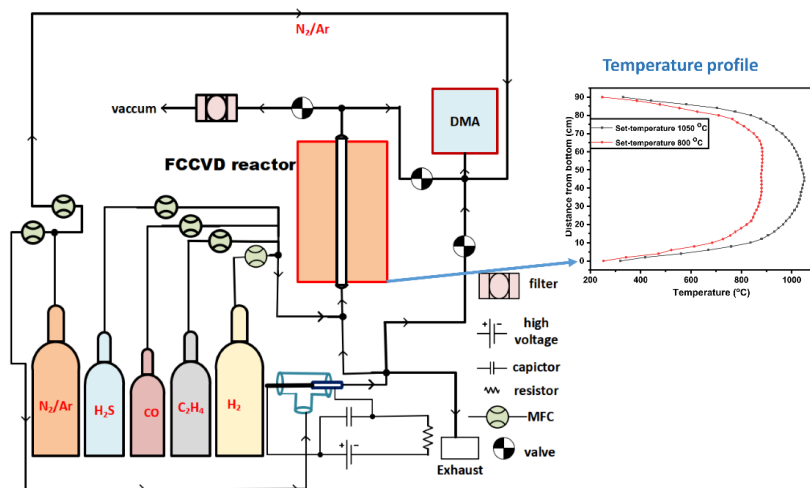
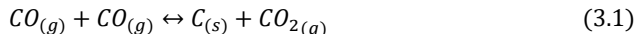


Fig. 3.4. Complete experimental set-up for the FC-CVD growth of SWCNTs using spark discharge produced catalyst particles and ethylene (C₂H₄) in **publication-II, III and IV** or carbon monoxide (CO) in **publication-I** as carbon sources. Hydrogen sulfide (H₂S) was utilized as a growth promotor in **publications-III and IV**. Schematic for gas-phase measurement of catalyst and SWCNTs NC by differential mobility analyzer (DMA). On right hand side temperature profile of the FC-CVD reactor at a set furnace temperature of 880 °C for CO and 1050 °C for C₂H₄.

3.4.4 Carbon source decomposition and SWCNTs synthesis

As-mentioned above we used CO as a carbon source in **publication-I** and C₂H₄ as a carbon source in **publications-II to IV**. The reaction mechanism of both processes is completely different. The key factor of selecting suitable carbon precursor is the thermodynamic stability of the chemical reaction at a given temperature and pressure. In chemical reactions, the change in Gibbs free energy (ΔG) determines the favorable direction of the reaction. For example, in Fig. 3.5 the ΔG for CO decomposition is positive when the temperature is above roughly 750 °C, meaning that its decomposition through Boudouard's reaction (Eq. 3.1) is favored in the forward direction below this temperature on metal catalysts [41]. Above 750 °C, the backward reaction is more favorable.



On the other hand, C₂H₄ decomposition has ΔG negative for the temperature range 100-1400 °C. Comparative to CO, the decomposition of C₂H₄ (being unsaturated hydrocarbon) is thermodynamically easier especially, at higher temperatures (above 1000 °C). Therefore, C₂H₄ can give more amount of carbon for the growth of SWCNTs. Possible reaction pathway of C₂H₄ decomposition on the metal catalyst for SWCNTs synthesis is given in the Eq. 3.2.

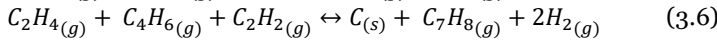
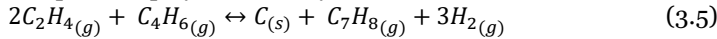


Moreover, the decomposition of C₂H₄ on such a high temperature can form higher hydrocarbons through the following possible reactions which have been observed in gas-phase Fourier transform infrared spectroscopy (FTIR) in our experiments.

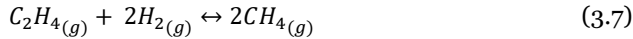




This reaction can produce poly aromatic hydrocarbons (PAHs)



Or C_2H_4 on its decomposition in the presence of H_2 can form saturated hydrocarbons



Therefore, it can be concluded that C_2H_4 on its decomposition inside the FC-CVD reactor not only provides carbon for SWCNTs growth but can give higher hydrocarbons as byproducts through their polymerization reactions.

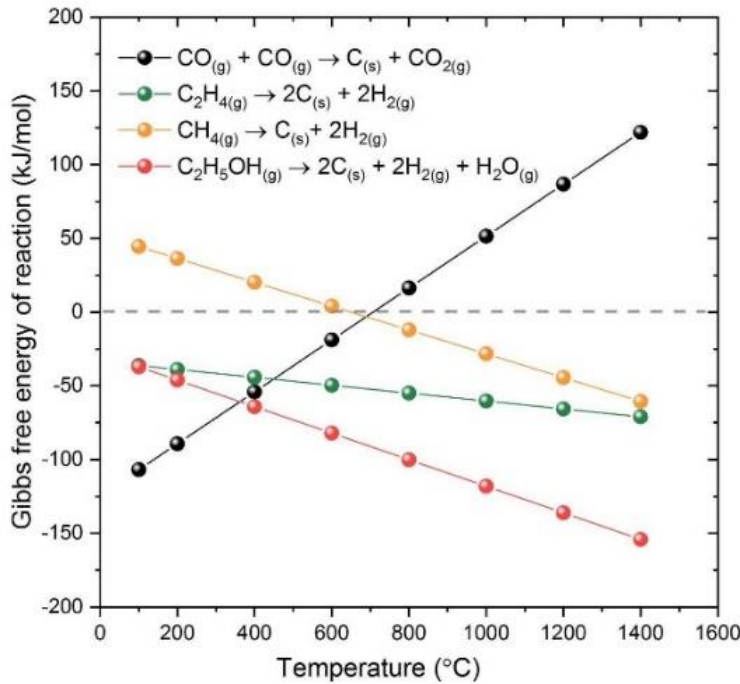


Fig. 3.5. Gibbs free energy (ΔG) of various carbon sources utilized for SWCNTs synthesis in FC-CVD method as a function of temperature. Image Copyright © 2019 Aalto University [42], used with permission.

3.4.5 Sample collection and deposition

As-produced SWCNTs inside the FC-CVD reactor were directly collected in gas-phase at the outlet of the FC-CVD reactor in the form of thin films on membrane filters (Merck Millipore, France, diameter 13 mm). The thin films from membrane filters were directly transferred on transparent quartz slides (HQS300, Heraeus) through well-established dry press-transfer technique [43] for their optical characterizations. However, for X-ray photoelectron spectroscopy analysis in **publication-III** sample was transferred on a gold substrate. Whereas for electron microscopy characterizations, of catalyst particles in **publication-I**

or SWCNTs in **publications-II, III** and **IV** were directly collected on transmission electron microscope copper grid, or were deposited onto Si/SiO₂ substrate or mica substrate using thermophoresis technique [44].

3.5 SWCNTs based transparent conductive films

Transparent conducting films (TCFs) are the essential components for many optoelectronic devices that pervade modern technology [45,46]. Generally, the materials for TCFs should have both high electrical conductivity and optical transparency. Conductive metal oxide especially, indium tin oxide (ITO), offering excellent opto-electronic properties, has been the most extensively used material for TCFs applications. However, its brittle nature [47] and limited resources [46] have presented many challenges for ITO applications in next generation flexible electronics. SWCNT films, known for their low refractive index [1], excellent mechanical flexibility, low haze [6] and better optical transparency [7], have made themselves one of the most appealing materials for the replacement of ITO in future flexible electronics. However, compared to the commercial ITO, SWCNT-TCFs suffer from low conductivity. Therefore, in the past decades, much efforts [7,43,48] have been devoted to improve the performance of the SWCNT-TCFs. Specifically, sulfur-assisted SWCNTs grown by the FC-CVD technique have been extensively employed to fabricate high-performance SWCNT-TCFs [48,49]. Unfortunately, in the literature the concrete impact of sulfur addition in enhancing the conductivity of the SWCNT films is ambiguous. Since, in most of the cases without sulfur, no information about SWCNT yield, morphology, structure and also the performance of the SWCNTs based films has been provided [48,49]. Consequently, the real out-turn of the sulfur addition on yield, morphology and structure of SWCNTs is ambiguous. Therefore, in **publication-III** we systematically investigated the effects of sulfur addition on various growth characteristics of SWCNTs, which might affect the performance of SWCNT-TCFs. For this purpose, the pristine SWCNT films with various thicknesses and transmittances were transferred from the membrane filter onto transparent quartz slides. To improve the conductivity of pristine SWCNT films they were doped with 16 mM solution of AuCl₃ (99.99%, Sigma-Aldrich) in acetonitrile (99.999%, Sigma-Aldrich) [50]. The detail of the doping processes has been summarized in Fig. 3.6.

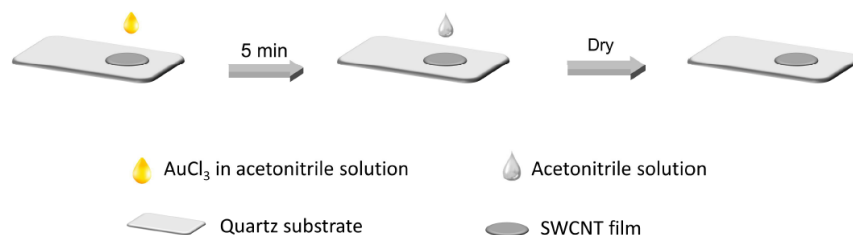


Fig. 3.6. A sequence of steps to improve the conductivity of SWCNT-TCFs by doping them with AuCl₃ using drop casting technique followed by washing with acetonitrile and drying with air. Image Copyright © 2019 Aalto University [42], used with permission.

Firstly, few drops of AuCl_3 solution were added on SWCNT films using drop casting technique. After 5 minutes of doping, pure acetonitrile was used to wash the AuCl_3 from the films and films were dried using compressed air before further characterizations and applications. The doping improves conductivity of SWCNT films by increasing carrier concentration in SWCNTs network and by reducing tube-tube junction resistance.

4. Characterizations

4.1 Differential mobility analysis

Scanning mobility particle sizer (SMPS) is an aerosol measurement technique for the size classification of submicron aerosol particles. It is a highly particle size and shape sensitive technique and roughly can classify particles down to 2 nm. The SMPS measurement is based on classifying charged aerosol particles (CAPs) by DMA according to their electrical mobility. When a CAP is placed in an external electric field, it experiences an electric force depending on the strength of the field. The electric force causes the CAP to accelerate in the direction of the field. The viscous drag force ($F_D = 6\pi\eta r v_t$) in the medium opposes this acceleration depending on the CAP size (r), velocity (v_t) and viscosity (η) of the medium. Hence, a known charge distribution particle with a smaller size have higher mobility. The measurement system is arranged in a way that particles lying in a selected mobility range pass through the DMA and are introduced into the particle counter (Fig. 4.1). Practically, the applied voltage is varied as a function of time to classify particles with different mobility sizes. The NC of the particle in each bin size is counted either by condensation particle counter (CPC) or by Faraday cup electrometer (FCE).

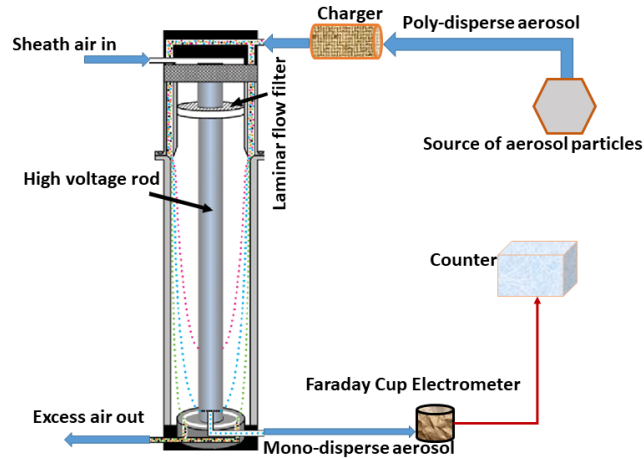


Fig. 4.1. Schematic arrangement for aerosol particles classification by Differential mobility analyzer with Faradays Cup Electrometer (DMA+FCE).

Since CPC cannot detect particle roughly less than 7 nm and we were interested in the detection of spark produced catalyst particles having a diameter roughly

2 nm. Therefore, in this dissertation, we used SMPS+FCE (the GRIMM Aerosol Technic GmbH, Germany with a sensitivity of 0.1 fA) to measure number size distributions (NSDs). In **publication-I**, SMPS+FCE was employed to monitor time stability, total NC, and effect of carrier gas (N_2 or Ar) flow rate on NSDs of various types of catalyst particles. In **publication-II** SMPS+FCE was utilized to monitor the effect of change in the catalyst composition on gas-phase real-time NC and yield of SWCNTs. Whereas in **publication-III** it was employed to get total NC and yield of SWCNTs as a function of sulfur concentration. Typical DMA measurements for catalyst particles and SWCNT's NSDs are shown in Fig. 4.2. To measure NC of the catalyst particles, 1 lpm flow of the aerosol from R-T SDG was directly introduced into SMPS+FCE. For CNTs NC, in all the cases, total flow (0.5 lpm) from the FC-CVD reactor was diluted with an additional 0.5 lpm of the pure carrier gas (N_2 or Ar). The mobility diameter (D_{ME}) of nanoparticles (spherical objects) is equivalent to the volumetric diameter. But D_{ME} of SWCNTs, apart from bundle diameter also depends on bundle length (l_b) (i.e. $D_{ME} \propto \sqrt[3]{l_b}$). Therefore, for spark-produced SWCNTs we observed D_{ME} greater than 30 nm as shown in Fig. 4.2b.

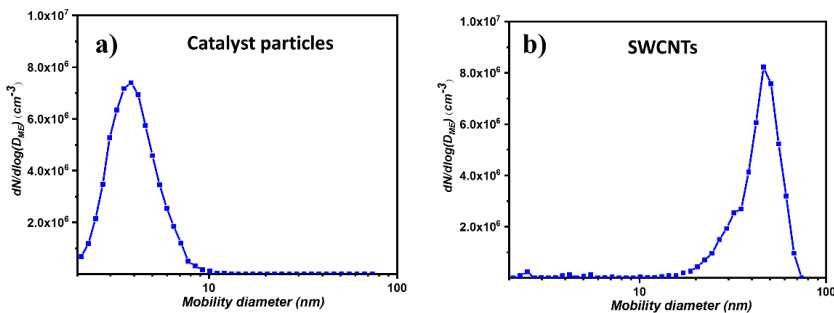


Fig. 4.2. Typical DMA pattern of **a)** spark-produced catalyst particles **b)** FC-CVD grown SWCNTs from spark-produced catalyst particles.

4.2 Optical spectroscopy

As mentioned in **chapter 2**, optical absorption spectroscopy and resonant Raman spectroscopy are two powerful techniques for the optical characterizations of SWCNT films. In the following sections, the details of the measurement setup of these two techniques have been provided.

4.2.1 Uv-Vis-NIR absorption spectroscopy

Uv-Vis-NIR absorption spectra of SWCNTs were obtained by transferring SWCNT thin film from membrane filter onto an optically transparent 1 mm thick quartz substrate (HQ5300, Heraeus) by dry press-transfer technique. In **publication-I** UV-Vis-NIR spectrometer (Perkin-Elmers Lambda 950) equipped with deuterium lamp and halogen lamp (wavelength ranging from 175 to 3300 nm) having dual-beam path (Fig. 4.3) was employed to get optical absorption spectra (OAS) of SWCNTs and transmittance (%) of the film at 550 nm (wavelength). Before the start of the measurement, 100% transmission baseline was calibrated without anything in the sample and reference pans. After calibration, a clean quartz substrate in the reference pan was employed to eliminate

the possible effects of the substrate and to get the absorption spectra of SWCNTs without any additional artifacts from the substrate.

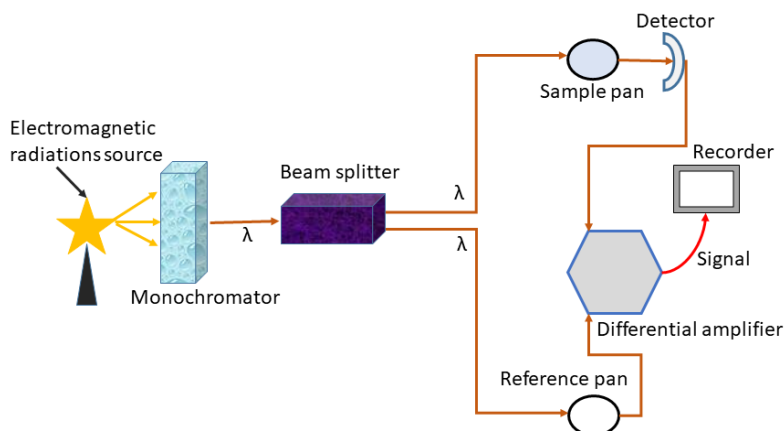


Fig. 4.3. General schematic of UV-Vis-NIR spectrometer.

In **publications-II, III** and **IV** OAS of SWCNTs and transmittance (%) were acquired from UV-Vis-NIR spectrometer (Agilent Carry 5000; Agilent Technologies, Inc.) in a similar method. We utilized OAS to estimate the mean diameter of SWCNTs using the Kataura plot as has been described in **chapter 2**. Furthermore, in **publications-II** and **III** transmittance of the film at various film thickness was determined by optical absorption spectroscopy. The SWCNTs normalized yield in **publication-II** for various catalyst particles and in **publication-III** for different concentrations of sulfur promoter was quantified based on the transmittance of the film. For a fixed time and collection area of the membrane filter (13 mm diameter), film thickness depends on the yield of SWCNTs. From Beer–Lambert law the transmittance of the film (T) at a fixed wavelength depends on its thickness (L) (i.e. $L \propto -\ln T$). Therefore, by knowing the transmittance of the film using OAS we can determine the thickness and normalized yield of SWCNTs.

4.2.2 Resonant Raman spectroscopy

In all the **publications** from **I** to **IV** resonant Raman spectra of SWCNTs was acquired using Horiba Labram-HR 800 Raman spectrometer (Horiba Jobin-Yvon, Japan). The spectrometer has a charge-coupled detector (CCD) and a microscope equipped with 10 \times , 20 \times , 50 \times , and 100 \times magnification objective lenses. The scan area is 75 \times 50 mm with a step size of 0.1 μ m. Three different excitation lasers 488 nm (argon), 514 nm (argon) and 633 nm (helium-neon) were utilized to get Raman spectra of SWCNT films (RBM, G and D modes) deposited on the quartz substrate.

4.3 Elemental analysis of SWCNTs film

Elemental analysis of sulfur-assisted SWCNT film in **publication-III** was carried out by using X-ray photoelectron spectroscopy (XPS). XPS is a surface-sensitive spectroscopic quantitative technique that can provide information about composition, chemical and electronic state of the material under investigation.

However, XPS can only reveal the surface composition of the top 1 to 10 nm thickness of the material. In XPS analysis, the material being analyzed is exposed to X-rays (having an energy roughly 1-15 keV) beam and the number of emitted electrons from the material along with their kinetic energy (K.E) are recorded. This process takes place in a high vacuum of the order of 10^{-8} millibar and the detection limit of the instrument is in the range parts per million (ppm) [51]. XPS can only detect those electrons that after escaping from the sample can pass through the vacuum of the instrument and finally reach the detector. Therefore, the number of electrons reaching the detector decreases exponentially with the increase in depth of the sample. The K.E of the emitted electrons combined with the work function (Φ) of the material and energy of the incident photons (E_{photon}) determines the binding energy of the electrons ($E_{\text{binding}} = E_{\text{photon}} - (E_{\text{K.E}} + \Phi)$) in the material. Since binding energy depends on the chemical environment to which atom is bonded therefore; it is used as a fingerprint to trace out the composition of the material in XPS analysis. A typical XPS spectrum is a plot of the number of detected electrons versus the binding energy of the electrons (Fig. 4.4).

In this dissertation (**publication-III**), elemental analysis of sulfur-assisted SWCNT films was carried out by using a Kratos Axis Ultra spectrometer with monochromatic Al K_{α} -radiation, a pass energy of 40 eV, X-ray power of 225 W and an analysis area of approximately $700 \mu\text{m} \times 300 \mu\text{m}$. The analysis was carried out to investigate the effect of sulfur addition on the composition of catalyst particles and to determine atomic concentrations of different species in the SWCNT sample.

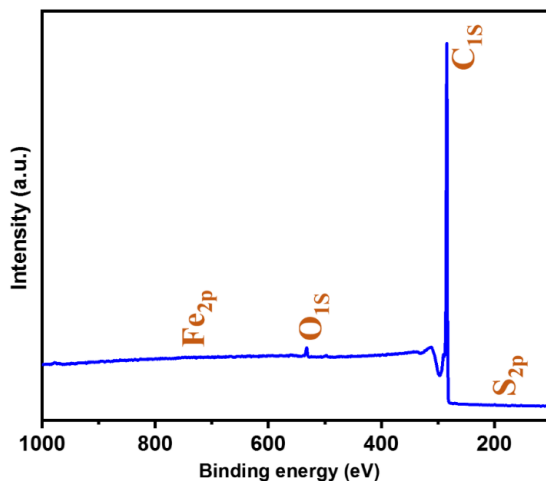


Fig. 4.4. X-ray photoelectron spectra of sulfur-assisted SWCNT film indicating the presence of carbon (SWCNT) by C_{1s} , sulfur (promotor) S_{2p} , oxygen (impurity) O_{1s} and iron (catalyst) Fe_{2p} peaks.

4.4 Sheet resistance measurement

Sheet resistance (R_s) is an important parameter to characterize TCFs and is a direct determination of the film resistance without measurement of its thickness. Mathematically the resistance (R) of a 3D regular conductor slab depends

on its resistivity (ρ), cross sectional area (A) and length (L) by the following formula.

$$R = \rho \frac{L}{A} = \frac{\rho}{t} \frac{L}{W} = R_s \frac{L}{W} \quad (4.1)$$

Where t is film thickness, which is often very difficult to measure experimentally, and W is the film width. R_s has unit Ω but it is usually expressed in Ω/sq to specify that it is the resistance between two opposite sides of a square and independent of the size of the square.

In this dissertation (**publications-II and III**) R_s of SWCNT-TCFs were characterized by a linear four-point probe (Jandel Engineering Ltd; UK having tip spacing 1.0 mm and tip radius 250 μm) combined with a multi-meter (HP/Hewlett Packard 3485A). The measurement current (I) was applied through the outer pair and the voltage drop (V) was measured by the inner pair of the probes (Fig. 4.5).

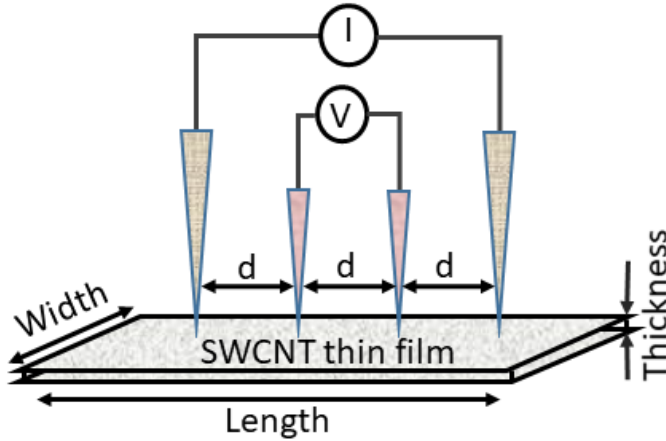


Fig. 4.5. Linear four probe set-up for the sheet resistance measurement of SWCNT thin films. The current is continuously supplied through the outer pair and voltage drop is measured from inner pair of the probes. Where d is the internal distance of two consecutive probes.

The R_s value was evaluated by the following relation.

$$R_s = \frac{\rho}{t} = \frac{\pi}{\ln(2)} \frac{V}{I} = 4.532 \frac{V}{I} \quad (4.2)$$

To compare the performance of SWCNT-TCFs with various catalysts in **publication-II** and at different sulfur concentrations in **publication-III**, SWCNT-films with varying thicknesses and transmittance were deposited on quartz slides. The R_s values of the SWCNT films were measured and a set of data points for transmittance versus R_s values were obtained. The data points were nonlinearly fitted using a well-established fitting method [43] to quantify the quality of SWCNT -TCFs.

4.5 Electron microscopy

Electron microscopic techniques are more direct and powerful tools to investigate the detailed structure, morphology and composition of nanoparticles and

SWCNT. In an electron microscope, an accelerated beam of electrons is used as a source of illumination. The wavelength associated with the accelerated electrons is much shorter (roughly 100, 000 times) than visible light. Therefore compared to optical microscopes, electron microscopes have higher resolving power and can reveal the fine structure of nanomaterials.

4.5.1 Scanning electron microscopy

Scanning electron microscope (SEM) utilizes a highly focused beam of electrons to scan the surface of the specimen and to produce an image of the surface. The accelerated electrons interact with the atoms of the specimen and lose their energy through a variety of mechanisms such as heat loss, backscattering of electrons, emission of light, X-rays and secondary electrons. Each of the signals can be detected by a specified detector giving information about the physical features of the surface or composition of the specimen.

In this work, we utilized SEM (Zeiss Sigma VP, Carl Zeiss GmbH, Germany) at accelerating voltage 1-2 kV in **publications-II** and **III** to measure bundle length distributions of SWCNTs at different experimental conditions and to examine the surface morphology of SWCNT-TCFs. For SEM observations, SWCNTs were directly deposited on Si/SiO₂ substrate using the thermophoresis technique [38]. The bundle length distributions of SWCNTs was obtained by using ImageJ software and counting all the SWCNTs in SEM image. A typical SEM image of SWCNTs is shown in Fig. 4.6. In **publication-IV**, we employed SEM at accelerating voltage of 5-10 kV to compare the relative number density of SWCNT and graphene flakes in the sample.

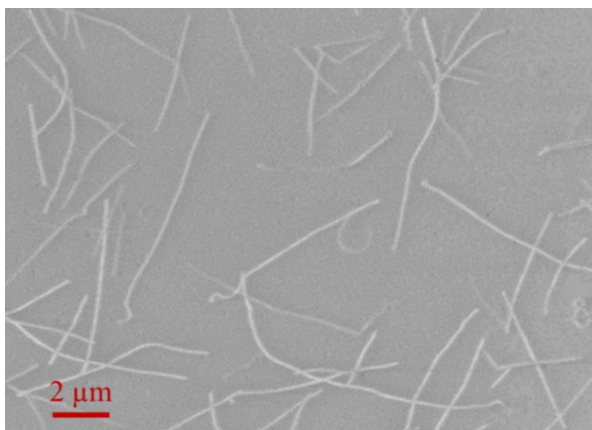


Fig. 4.6. A typical scanning electron microscope (SEM) image of SWCNTs.

4.5.2 Transmission electron microscopy

Transmission electron microscopy (TEM) utilizes a beam of transmitted electrons through an ultrathin specimen (roughly < 100 nm thick) to form a highly magnified image of the specimen. The beam interacts with the atoms of the specimen and the transmitted electrons are focused by the objective lens on a fluorescent screen or on charge-coupled device (CCD) camera to form the image. The resultant TEM image from these transmitted electrons is called a bright-field (BF) image. In BF image, the darker regions show those areas of the

specimen through which fewer electrons are transmitted and brighter regions show those areas through which more electrons are transmitted. On the other hand, if the scattered electrons are focused by the objective lens and transmitted electrons are blocked then we get dark-field (DF) images. Since, the thicker regions of the specimen scatter more electrons compare to thinner ones, therefore, in DF images thicker region of the specimen appears brighter in the image. Another type of TEM is scanning-TEM (STEM) in which an electron beam is focused on a fine spot (typically 0.05-0.2 nm) and is scanned over the sample in a raster. The scanning of the electron beam over the sample makes STEM a more suitable technique for analytical spectroscopy such as X-rays energy dispersive spectroscopy (EDS), high-angle annular dark-field (HAADF) imaging, and electron energy loss spectroscopy (EELS).

In this thesis double aberration-corrected high-resolution TEM (HR-TEM) (JEOL-2200FS, JEOL Ltd., Japan) equipped with an EDX spectrometer has been used in **publications-I, II and III** to observe the structure, size and composition of different catalyst nanoparticles. In **publications-II and III** HR-TEM was used to determine the bundle diameter of the SWCNTs. Typical HR-TEM images of an individual and bundled SWCNT are provided in Fig. 4.7.

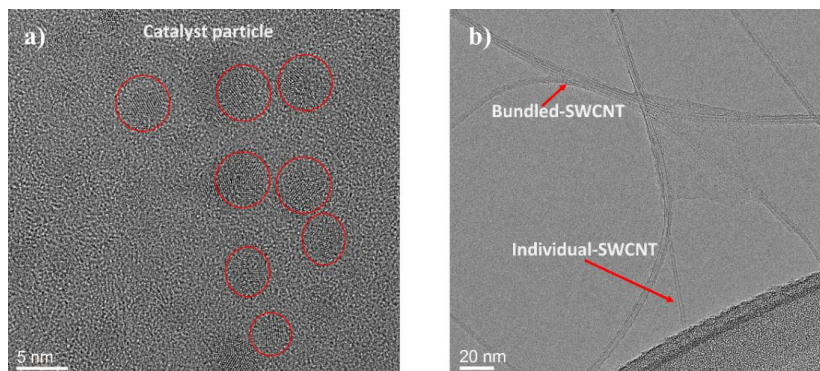


Fig. 4.7. High-resolution transmission electron microscope (HR-TEM) image of **a)** catalyst particles **b)** individual and bundled SWCNTs.

In **publications-II, III and IV** electron diffraction patterns (EDPs) of SWCNTs and graphene-flakes were acquired from HR-TEM. In **publications-II and III** EDPs (Fig. 4.8) were employed to determine the chirality of SWCNT by using the intrinsic layer line spacing method [52].

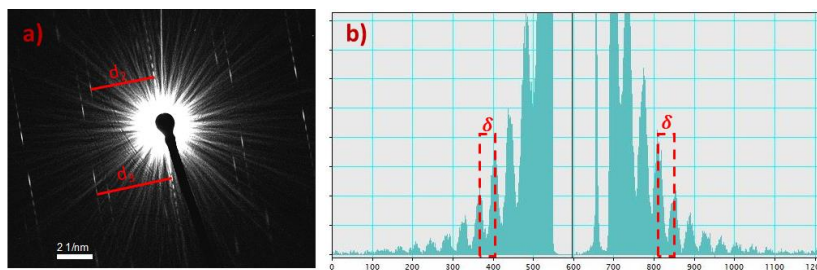


Fig. 4.8. **a)** The electron diffraction pattern (ED) of an individual SWCNT. **b)** The corresponding image of equilateral line in software Gatan Digital Micrograph.

The pseudo-period of equilateral line (δ) and layer line spacing (d_2 and d_3) can be acquired by using software Gatan DigitalMicrograph. In **publication-IV** atomic-resolved STEM imaging was done using aberration-corrected Nion UltraSTEM 100 operated with 60 keV beam energy to observe the number of graphene layers and structure of as-synthesized graphene carbon nanotubes hybrid.

4.6 Atomic force microscopy

Atomic force microscopy (AFM) is a sub-nanometer resolution scanning probe microscopy technique for the 3D imaging of the specimen. In AFM, the information about surface topography is gathered by a tip fixed on a stiff cantilever either by touching the surface or by feeling the force between the tip and surface. The deflection in the tip movement on interaction with the specimen is measured with the help of a reflected laser beam from the cantilever. The reflected laser beam is constantly monitored by the position-sensitive photo-detectors and is controlled by a feedback loop during the whole scanning process to get topography images. In this dissertation (**publication-IV**), we utilized AFM dimension icon (Scan asyst mode: Bruker nano surfaces U.S.A.) to characterize SWCNT-graphene hybrid structures at various growth conditions. For this purpose, the samples were directly collected at the outlet of the reactor in gas-phase on cleaved muscovite mica (V-4 grade electron microscopy sciences, U.S.A.) substrate using thermophoresis technique [38]. Fig. 4.9 a and b are typical AFM images of SWCNT graphene hybrid at two different experimental conditions displaying a very high number density of isolated graphene flakes and very low number density of graphene flakes in the samples respectively.

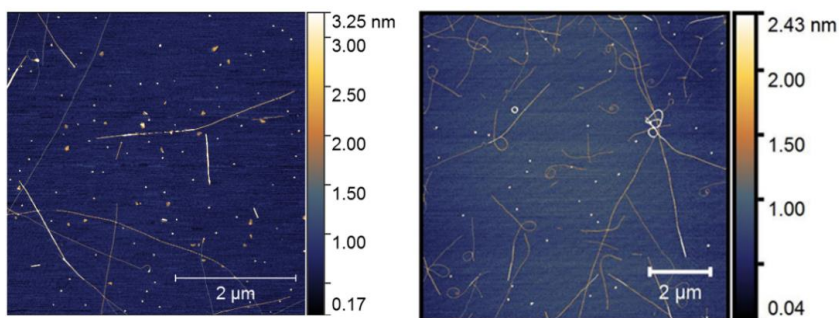


Fig. 4.9. Representative AFM images of **a)** SWCNT-graphene hybrid and **b)** pure-SWCNTs without graphene flakes.

Hence, in our case, AFM is a highly promising technique to characterize SWCNT graphene hybrid structure and to compare the relative number density of SWCNTs and graphene in the sample.

5. Results and discussion

5.1 Gas-phase synthesis of time consistent catalyst particles

As mentioned in **chapter 3**, we designed R-T SDG to produce highly time consistent metallic and bimetallic catalyst particles for a long time in gas-phase for the synthesis of SWCNTs. We found that R-T SDG is capable of producing less agglomerated nanoparticles under relatively small flow rate of the carrier gases compared to the conventional rod to rod (R-R) [35] configuration and is more stable configuration compared to pin to plate [53], wire in hole and wire to hole electrode configurations [54]. The time stability of as produced nanoparticles from R-T SDG in terms of their total NC and particle size distribution was monitored in gas-phase by DMA for 24 hours. Fig. 5.1 shows stability in total NC cm^{-3} of catalyst particles, their geometric mean diameter (d_g), and also geometric standard deviation (σ_g) of various monometallic (Fe, Ni, Cu) and bimetallic (Co-Ni) catalyst particles for one day (24 hrs). At the start of the experiment d_g of Fe particles was recorded 5.17 nm which reduced to 5.09 nm in one day. On the other hand, the total NC cm^{-3} decreased roughly from 1.5×10^7 to 1.4×10^7 . For Ni nanoparticles, d_g varied in the range 5.46 nm to 5.72 nm in 24 hrs with a variation in total NC cm^{-3} from roughly 1.0×10^7 to 1.06×10^7 .

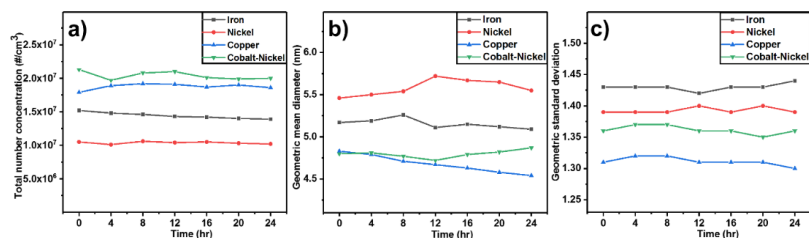


Fig. 5.1. Time stability observed from DMA in **a)** total NC, **b)** geometric mean diameter and **c)** geometric standard deviation of monometallic Fe, Ni, Cu, and bimetallic Co-Ni, nanoparticles in the flow rates (0.5-2.2 lpm) of nitrogen or argon as carrier gases. Image Copyright © 2018 Elsevier [10], used with permission.

Bimetallic Co-Ni nanoparticles were synthesized using rod electrode of Co and tube electrode of Ni. Production of Co-Ni nanoparticles in gas-phase from R-T SDG also showed high time consistency with respect to their d_g and total number concentration cm^{-3} . The experimental conditions including applied current (~ 0.01 - 0.1 mA), voltage (~ 1 - 3 kV), external capacitor (~ 100 - 330 pF) and flow rate of carrier gases (~ 2 - 2.2 lpm) for the synthesis of pure Fe, Ni and mixed Co-

Ni nanoparticles having $d_g < 5$ nm were found very similar to each other. However, we found that for the time stable synthesis of copper nanoparticles having similar NC and d_g as that of pure Fe, Ni and mixed Co-Ni requires completely different experimental conditions. For the synthesis of Cu nanoparticles, we employed roughly 3 times higher external capacitor (1 nF) and current (0.15 mA) under roughly 0.5 lpm flow rate of Ar as the carrier gas. It's worth mentioning that the stability in total NC cm^{-3} of Cu nanoparticles and their d_g under the above-mentioned conditions also indicated that R-T SDG is a more suitable design for the gas-phase production of catalyst particles.

5.1.1 Material dependent electrode's evaporation

The different experimental conditions required for the synthesis of Cu nanoparticles compared to the other catalysts indicated that the amount of material evaporated from the electrodes per spark in the ionization process is highly sensitive to the surface of the electrodes material. In this regard, the thermal conductivity of the material is an important parameter that highly influences the amount of material evaporated per spark [55]. Mathematically, the amount of eroded mass from the electrodes in SDG is related to the various physical properties of the material by the following equation.

$$m = \frac{1/2C_{ext}V_d^2 - bT_b^4 - gk(T_b - T)}{C_{ps}(T_m - T) + \Delta H_m + C_{pl}(T_b - T_m) + \Delta H_v} \quad (5.1)$$

In Eq. 5.1, the first term in numerator shows effective spark energy, the second term is for heat loss due to radiation with boiling point T_b of the metal, and term $gk(T_b - T)$ is for heat transfer due to conduction with thermal conductivity (k) of the metal and T is ambient temperature. Whereas, in denominator $C_{ps}(T_m - T)$ and $C_{pl}(T_b - T_m)$ show the energy required to heat the material to their melting point (T_m) and boiling points, respectively. Also, the term ΔH_m represents enthalpy of melting and ΔH_v enthalpy of evaporation [56]. From Eq. 5.1, materials having higher thermal conductivity are more resistive to evaporation in SDG because they are easily cooled after the spark is over. Therefore, in our case Cu having higher thermal conductivity (401 W/m K) compared to Fe (80 W/m K), Co (69 W/m K), and Ni (91 W/m K) needs a higher amount of energy for material ablation.

5.1.2 Tuning size and concentration of catalyst particles

To utilize SDG produced nanoparticles as catalyst for the synthesis of advanced materials such as SWCNTs it is highly desired to precisely control their NC and size distributions. Therefore, in **publication-I** we tuned the NC and NSDs of catalyst particles through changing flow rate and nature of carrier gases. Keeping applied current and external capacitor constant, for Fe catalyst particles the effect of carrier gas flow rate on d_g and total NC in the flow range 1.1 lpm to 3.3 lpm of N_2 and Ar is shown in Fig. 5.2a and b, respectively. In both cases, the mobility diameter decreased with an increase in flow rate of the carrier gases. Because, the higher gas flow rate increases transport velocity as well as the cooling rate at the spark generation point which reduces the probability of agglomeration of primary particles [56]. Hence, we observed a reduction in particle size

with an increase in carrier gas flow rate. However, for both N₂ and Ar, NC of catalysts increased with the increase in the amount of carrier gases. The reason behind the increase in NC is decrease in the agglomeration rate of the particles through collision and reduction in the size of catalyst particles.

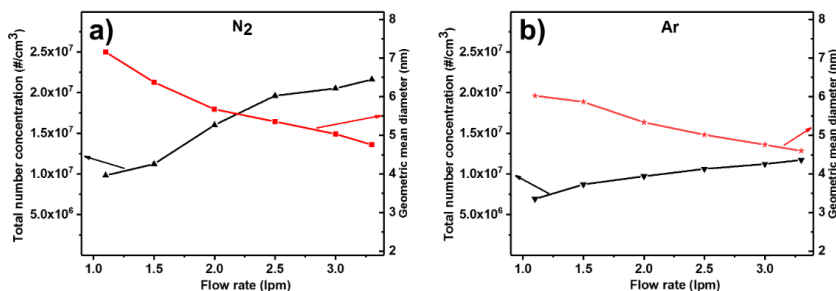


Fig. 5.2. A reduction in geometric mean diameter and increase in total NC of Fe catalyst particles measured from DMA in the flow range 1.1 lpm to 3.3 lpm of **a)** nitrogen and **b)** argon as carrier gases. Image Copyright © 2018 Elsevier [10], used with permission.

We also found that the changing nature of carrier gas in R-T SDG has also a pronounced effect on the catalyst size and NC. The nature of carrier gas mainly affects discharge voltage depending on thermal, chemical, and physical properties of the gases. For example, in our case for Fe electrodes under fixed flow rate (2 lpm) of N₂ and Ar, the discharge voltage for N₂ is roughly 2.5-fold higher than that of Ar. The most important reason for the drastic change in discharge voltage is the higher breakdown voltage of N₂ compared to Ar [57]. Resulting in a higher amount of the effective discharge energy per spark ($E = 1/2 C_{ext} V_d^2$) compared to Ar. Therefore, in the case of N₂ comparatively more amount of energy per spark is available for the material ablation from the electrodes. In SDG, the mass evaporation rate from the electrodes mainly depends on the amount of energy delivered per spark. Therefore, more material should be evaporated from the electrodes in case of N₂ as the carrier gas compared to Ar. DMA measurements (Fig. 5.2a and b) also indicated that if all the experimental conditions are kept constant and only carrier gas is changed from N₂ to Ar, then mobility diameter of catalysts for N₂ is larger than that in case of Ar, and total NC cm⁻³ is higher as compared to Ar due to enhanced mass loss of the electrodes. Interestingly, when we produced Fe nanoparticles using N₂ or Ar as carrier gas having similar NSDs and employed them for the synthesis of SWCNTs, we found that carrier gas has no role in tuning the morphology and chirality of SWCNTs. It verified that spark produced catalyst particles and their catalytic activity depends on their size and concentration, not on the nature of the ionization process for their formation in the spark discharge generation chamber.

5.1.3 Morphology and composition of catalyst particles

HR-TEM was employed to investigate the morphology and composition of spark-produced catalyst nanoparticles. Fig. 5.3a, displays a typical high-angle annular dark-field (HAADF) STEM image of monometallic Fe catalyst particles. Most of the catalyst particles were found individual and very few were found agglomerated. The mean size of catalyst particles observed from HR-TEM is

4.37±1.27 nm. To produce bimetallic catalyst particles electrodes of known composition of two different metals were utilized. Fig. 5.3b, shows STEM image of bimetallic Co-Fe nanoparticles with a mean size of 4.41±1.58 nm.

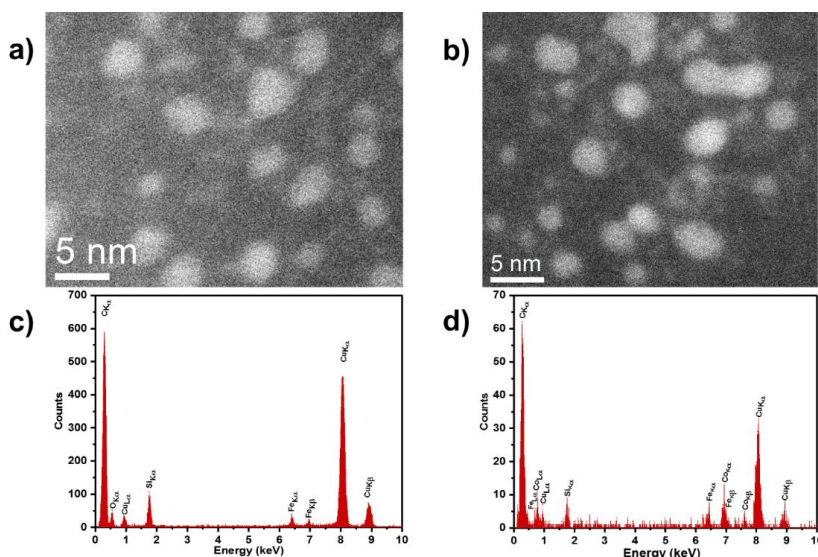


Fig. 5.3. High-angle annular dark-field (HAADF) STEM image of spark discharge produced **a)** monometallic Fe **b)** bimetallic Co-Fe nanoparticles. X-rays energy dispersive spectrum (EDS) of **c)** Fe (monometallic) **d)** Co-Fe (bimetallic) catalyst nanoparticles, collected on holy carbon-coated TEM copper grid. Image Copyright © 2018 Elsevier [10], used with permission.

Using STEM, EDS analysis of monometallic and bimetallic nanoparticles was carried out to know their composition. In EDS of monometallic Fe (Fig. 5.3c), Fe_{Kα} and Fe_{Kβ} peaks confirmed the formation of pure Fe nanoparticles. The O_{Kα} peak in this EDS is due to the surface oxidation of Fe nanoparticles. The EDS of Co-Fe bimetallic catalyst particle (Fig. 5.3d) apart from Fe peaks (i.e. Fe_{Lα}, Fe_{Kα}, and Fe_{Kβ}) contains additional Co peaks (Co_{Lα}, Co_{Kα}, and Co_{Kβ}) indicating the formation of bimetallic Co-Fe nanoparticles. From EDS analysis, bimetallic Co-Fe nanoparticles are inhomogeneous alloy. It's worth mentioning that all the peaks having carbon, Cu and Si in EDS are background peaks which are the consequence of the presence of these materials in the holy carbon-coated TEM copper grid. Hence, EDS analysis revealed that the catalyst particles of the desired composition of both monometallic or mixed metallic having high purity can be synthesized in gas-phase with R-T SDG, by proper choice of the electrodes material. However, the percentage composition and homogeneity of the alloy materials are hard to control in the spark discharge generation process due to the difference in evaporation rate of the two different materials.

Moreover, we investigated the effects of post-synthesis annealing on the structure and morphology of spark-produced catalyst particles. The effects of post-synthesis annealing are of great importance where spark-produced catalyst particles are utilized for the synthesis of more advanced structures such as SWCNTs, in the presence of high temperature inside the FC-CVD reactor. Since for SWCNTs, it is commonly believed that their chirality and structure is mainly

controlled by the structure, size, and nature of catalyst particles. Therefore, we annealed catalyst particles at 700 °C in the FC-CVD reactor without adding any carbon precursor. The purpose of the experiment was to know the possible effects of temperature on morphology of catalyst particles. Fig. 5.4a and b, are HR-TEM images of Co-Ni catalyst particles before and after annealing in the FC-CVD reactor, respectively.

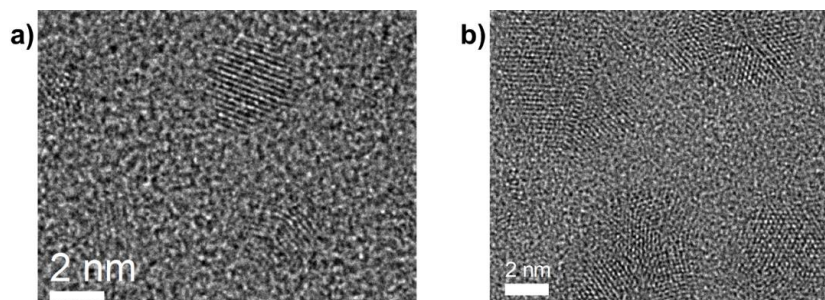


Fig. 5.4. HR-TEM image of Co-Ni bimetallic nanoparticles **a)** collected directly from SDG before annealing and **b)** collected after annealing at 700 °C at the outlet of the FC-CVD reactor in the presence of nitrogen as carrier gas. Image Copyright © 2018 Elsevier [10], used with permission.

From Fig. 5.4a, it is obvious that without annealing spark produced Co-Ni particles have comparatively small size and polycrystalline structure having polyhedral shape. Whereas in Fig. 5.4b, it can be seen that after annealing at 700 °C the particles are more accumulated and they have polycrystalline structure. They could be in the form of small agglomerates having a polycrystalline structure or cluster of smaller nano-crystallites. However, a very prominent change in particle size (bigger in size) and shape was observed with the post-annealing treatment.

5.2 Catalyst composition effects on FC-CVD growth of SWCNTs

A better control of SWCNTs morphology and structure is a big challenge for their many potential applications. It has been observed that the catalyst composition plays a vital role in the controllable synthesis of SWCNTs [5,8,58]. Specifically, the bimetallic catalysts particles with highly controlled structure and catalytic activity have been utilized to get a narrow chirality of SWCNTs [8]. However, for the scalable synthesis of SWCNTs by the FC-CVD method, the modulation in the catalyst composition has remained limited due to many challenges in the gas-phase preparation of catalysts particles. Therefore, very few research groups investigated [5,8] the effects of metallic and bimetallic catalyst particles on FC-CVD grown SWCNTs. Furthermore, all the existing techniques for investigating the effects of catalyst composition on FC-CVD grown SWCNTs are not capable to produce highly pure SWCNTs [5,58]. The SWCNTs are separated through a multi-step, liquid-based, post-synthesis, sonication-centrifugation and annealing process from carbon black powder containing a mixture of SWCNTs and MWCNTs before their further characterizations and applications.

In this dissertation (**publication-II**), we synthesized SWCNT through a single-step, direct and gas-phase method using a variety of spark produced monometallic (Fe, Co, Ni) and bimetallic (Co-Ni and Co-Fe) catalyst particles. We quantitatively investigated the effects of catalyst composition on different growth characteristics of SWCNT which have been discussed in detail in the following sections.

5.2.1 Optimization of the growth conditions

The growth conditions of SWCNTs with various catalysts were optimized based on the SWCNT-TCFs performance i.e. the R_s of 90% transparent SWCNTs films (@ 550 nm wavelength). For quantitative comparison, all the catalyst particles (Fe, Co, Ni, Co-Ni and Co-Fe) were fixed to a similar NSD using DMA as shown in Fig. 5.5a. The optimum amount of C_2H_4 for monometallic Fe and Co is 0.1 sccm (200 ppm), and for Ni is 0.4 sccm (800 ppm). On the other hand, for bimetallic Co-Ni and Co-Fe is 0.3 sccm (600 ppm). The required H_2 flow is 80 sccm with 420 sccm N_2 from R-T SDG containing catalyst particles at a setting temperature 1050 °C of the FC-CVD reactor.

5.2.2 SWCNT yield dependence on catalyst composition

The yield of SWCNTs was compared by DMA and was found highly sensitive to the composition of catalyst particles. The yield order for various catalyst is Fe>Co-Fe> Co>Co-Ni>Ni, as has been shown in Fig. 5.5b. For all above-mentioned catalysts, the geometric mean D_{ME} was adjusted to roughly 3.5 nm having total NC $\sim 4.3 \times 10^6 \text{ cm}^{-3}$ (Fig. 5.5a) before feeding into the vertical FC-CVD reactor. The D_{ME} for Fe, Co, Co-Fe and Co-Ni SWCNTs were found $\sim 45 \text{ nm}$. Interestingly, the NC of Fe, Co, Co-Fe SWCNTs are comparable, but NC of Co-Ni SWCNT is slightly lower. However, we found that SWCNTs from Ni catalyst were utterly different. Compared to SWCNTs from other catalysts, Ni SWCNTs have very small $D_{ME} \sim 15 \text{ nm}$ and lower NC. The D_{ME} of SWCNTs depend on their bundle length and bundle diameter. Therefore, DMA measurements indicated that SWCNTs from Ni have shorter bundle length compared to SWCNTs from Fe, Co, Co-Fe and Co-Ni catalysts. The variation in yield with the change in catalyst composition was also observed by comparing the optical transmittance of SWCNT-TCFs for a fixed time and collection area. The data quantitatively revealed that yield of Fe SWCNTs is ~ 10 times higher than that of Ni SWCNTs. The possible reason behind poor catalytic activity of Ni towards SWCNT synthesis might be its lower carbon solubility compared to Fe and Co [37,59].

Surprisingly, the opto-electronic performance of SWCNT-TCFs was also found catalyst composition dependent. The R_s of the pristine, 90% transparent SWCNT films from various catalysts has been plotted in Fig. 5.5c. It can be seen that the opto-electronic performance of Fe, Co, Co-Fe and Co-Ni based SWCNT-TCFs is superior to that of Ni based SWCNT-TCFs. Hence, spark produced Ni-SWCNTs due to their shorter bundle length are not a preferable choice for TCF applications. The OAS of SWCNTs with various catalysts did not show any remarkable change in the diameter of SWCNTs as can be seen from the S_{11} and M_{11}

peaks positions in Fig. 5.5d. The mean diameter of as-synthesized SWCNTs with various catalysts, analyzed from Kataura plots [19] is around 1 nm and was found primarily controlled by the NSDs of catalyst particles rather than their composition. Hence, we conclude that catalyst size is more effective to control the diameter of SWCNTs in FC-CVD method.

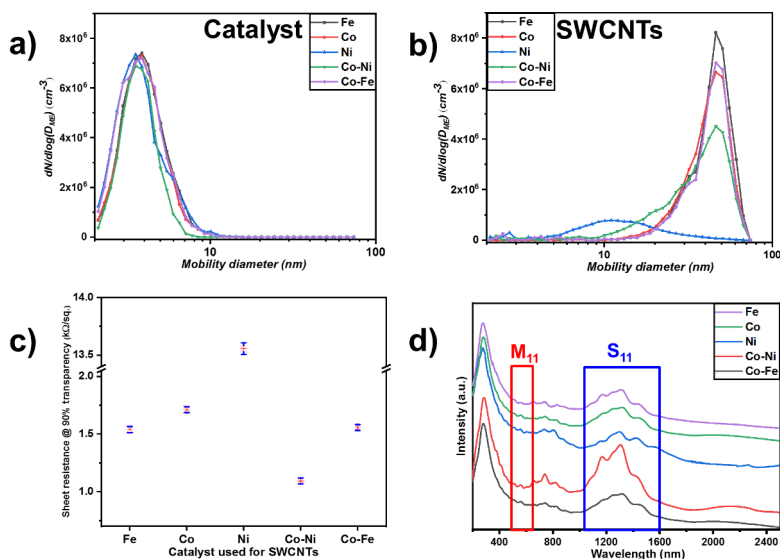


Fig. 5.5. Number size distributions of **a)** Fe, Co, Ni, Co-Ni and Co-Fe catalyst particles before feeding into the FC-CVD reactor and **b)** as-synthesized SWCNTs from various spark produced catalysts measured in gas-phase by DMA at the outlet of the FC-CVD reactor. **c)** A comparison in sheet resistance values of pristine Fe, Co, Ni, Co-Ni and Co-Fe SWCNT-TCFs at 90% transmittance (@ 550 nm wavelength). **d)** OAS of as-grown SWCNTs indicating no prominent shift in the mean diameter of SWCNTs with the change in the catalyst composition. Image Copyright © 2019 Elsevier [11], used with permission.

Transition metals Fe, Co and Ni have been mainly utilized as catalysts for the synthesis of SWCNTs in supported-CVD processes because they are comparatively cheap, abundant and highly active metals [37] for the growth of SWCNTs. Moreover recent studies showed that Fe, Co and Ni have strong adhesion with growing CNTs and thus they are very useful to get high curvature CNTs (small diameter nanotubes i.e. SWCNTs) [60]. On the contrary, our results showed that spark-produced Ni has poor catalytic activity towards the synthesis of SWCNTs in the FC-CVD method. Also, Fe is widely explored catalyst for the synthesis of SWCNTs in the FC-CVD method [48,49]. Therefore, we synthesized bimetallic catalyst particles of Co with Fe and Ni which have never been studied in the FC-CVD growth of SWCNTs. The composition of the resulting bimetallic catalysts were verified by STEM-EDS analysis.

Interestingly, Co based bimetallic catalysts compared to pure Co gave a lower yield of SWCNTs but the better opto-electronic performance of SWCNT-TCFs. Specifically, Co-Ni based SWCNT-TCFs exhibits better performance than Co and Co-Fe based SWCNT film (Fig. 5.5c). It's worth noticing that at optimized conditions with similar NSDs of five different types of catalysts (i.e. Fe, Co, Ni,

Co-Ni and Co-Fe) there are pronounced changes in NC of SWCNTs. It indicates that catalyst composition significantly affects the decomposition of C_2H_4 and also nucleation and growth of SWCNTs. More importantly, from OAS we observed that Co-Ni based SWCNTs have a relatively higher S_{11} peak compared to the SWCNTs from other catalysts (Fig. 5.5d). The higher S_{11} peak might be an indication for the production of chirality enriched SWCNTs with Co-Ni catalyst. On the other hand, SWCNTs from bimetallic Co-Fe apparently don't have any unique optical absorption features compared to that of pure Co based SWCNTs. Based on the above mentioned experimental results of five kinds of SWCNTs yield, OAS and opto-electronic performance of their TCFs, we selected three most promising kinds of SWCNTs (i.e. Fe, Co and Co-Ni) for further characterizations to investigate in detail the effect of catalysts composition on SWCNTs morphology, chirality and film conductivity.

5.2.3 Catalyst composition effects on SWCNTs morphology

The opto-electronic performance of SWCNT-TCFs largely depends on the morphology of SWCNTs including diameter of individual nanotubes, their average bundle length and bundle diameter. SWCNTs in gas-phase can collide with each other forming their bundles inside the FC-CVD reactor or while moving from the FC-CVD reactor to the collection point. Therefore, we investigated the effect of change in catalyst composition on bundle length and diameter of Fe, Co, and Co-Ni SWCNTs. The bundle length comparison was made by measuring the length of 200-220 bundles in each case, deposited on Si/SiO₂ substrate [38] using SEM. The results acquired from SEM analysis for Fe, Co and Co-Ni SWCNTs have been plotted as bundle length distributions in Fig. 5.6. A typical SEM image utilized for measuring bundle length has been provided in Fig. 5.6a.

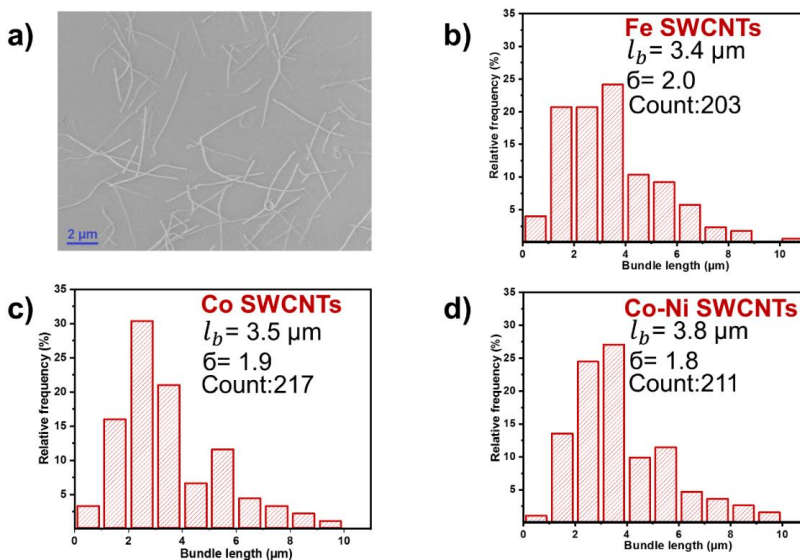


Fig. 5.6. **a)** A typical SEM image of SWCNTs bundles on Si/SiO₂ substrate. Bundle length distributions of **b)** Fe ($l_b \approx 3.4 \mu m$), **c)** Co ($l_b \approx 3.5 \mu m$) and **d)** Co-Ni ($l_b \approx 3.8 \mu m$) SWCNTs. Image Copyright © 2019 Elsevier [11], used with permission.

We observed that change in catalyst composition has no significant effect on average bundle length (l_b) of SWCNTs. The SWCNTs produced by Fe catalyst particles have the shortest l_b of 3.4 μm whereas, Co based SWCNTs have l_b of 3.5 μm . The longest CNTs were found from Co-Ni catalyst having the average bundle length of 3.8 μm . The measurement of bundle diameter distribution of SWCNTs was carried out by utilizing HR-TEM and by carefully analyzing 170-180 HR-TEM micrographs for all the three catalysts. The largest average bundle diameter (d_b) was found 4.4 nm for Co SWCNTs with 12% individual SWCNTs (see Fig. 5.7). A typical HR-TEM image of an individual and a bundled SWCNT bundle is also displayed in Fig. 5.7a. A nominal reduction in bundle size was observed with Fe ($d_b \approx 4.1$ nm) and Co-Ni ($d_b \approx 4.0$ nm) catalysts with a slight increase in percentage ($\approx 14\%$) of individual SWCNTs in both cases.

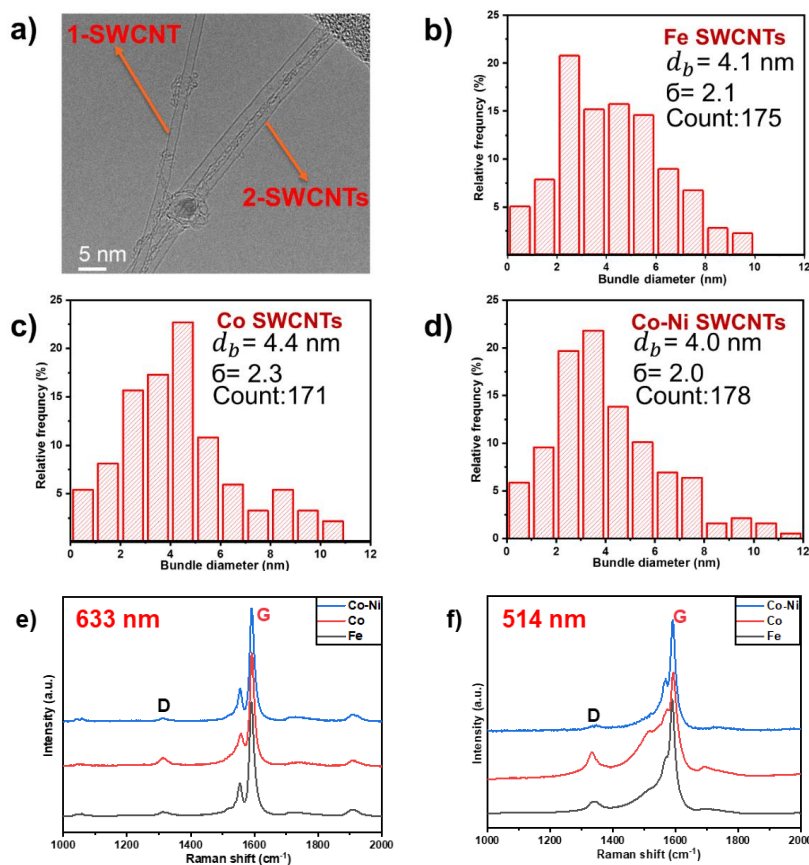


Fig. 5.7. a) HR-TEM image of an individual and a bundled SWCNT. Bundle diameter distribution of **b)** Fe ($d_b \approx 4.1$ nm), **c)** Co ($d_b \approx 4.4$ nm) and **d)** Co-Ni ($d_b \approx 4.0$ nm) based FC-CVD synthesized SWCNTs. Raman spectra of as grown- SWCNTs from Fe, Co & Co-Ni having G (1589 cm^{-1}) and D (1348 cm^{-1}) modes, with **e)** 633 nm and **f)** 514 nm lasers. Showing higher quality of Co-Ni SWCNTs. Image Copyright © 2019 Elsevier [11], used with permission.

Another very important parameter of SWCNTs for their many potential applications is the diameter, which has been investigated here. We compared the diameter of the Fe, Co and Co-Ni SWCNTs by using OAS, Raman spectra and analyzed statistically by using EDPs of SWCNTs. In OAS the highest intensity S_{11}

peak of Fe and Co SWCNTs was found roughly at 1322 nm (Fig. 5.5d), corresponding to *ca.* mean diameter of 1.01 nm. Hence, our result is consistent with the result obtained from different ratios of Co and Fe used as a catalyst in the supported-CVD method [61], where it has been observed that catalyst composition does not affect the diameter of SWCNTs. However, a tiny shift in the highest intensity S_{11} peak towards smaller diameter (at 1305 nm, corresponding to *ca.* 0.98 nm mean diameter) was observed with Co-Ni as catalyst. The small diameter nanotubes (≈ 1 nm) due to their large bandgap could have many potential applications, for example, in photovoltaic devices [62]. The RBM peaks in Raman spectra (Fig. 5.8) with 633, 514 and 488 nm lasers indicated that our SWCNTs have diameter in the range from 0.75 nm to 1.65 nm. However, it can be seen that with the change in catalyst composition there is a change in the relative abundance of different diameter nanotubes.

We compared Raman spectra (with excitation lasers 514 nm and 633 nm) of as-synthesized SWCNTs with different catalyst particles to know about their quality. We found that Co-Ni SWCNTs have comparatively less defects or disorder structures compared to Fe and Co based SWCNTs. It can be seen from Fig. 5.7e and f that the I_G/I_D ratio for Co-Ni SWCNTs > Fe SWCNTs > Co SWCNTs. Maximum value of 21, was observed for Co-Ni and minimum value of 13 for Co SWCNTs. These results indicate smaller number of defects or disorder structures in Co-Ni SWCNTs and higher quality compared to others.

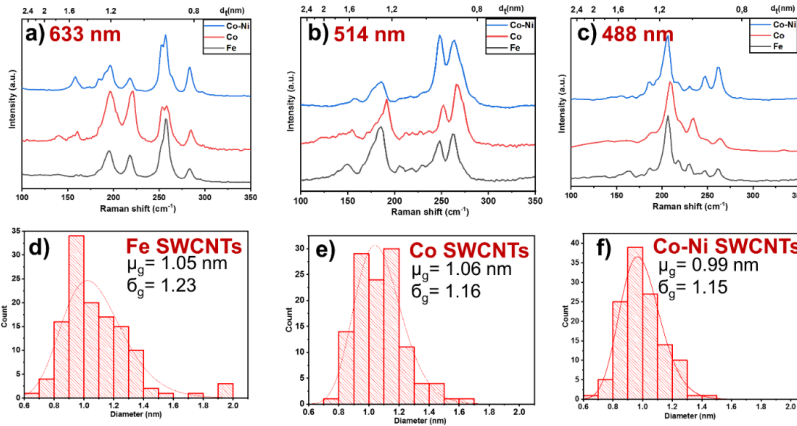


Fig. 5.8. RBM of as-synthesized Fe, Co and Co-Ni SWCNTs with **a)** 633 **b)** 514 and **c)** 488 nm lasers. SWCNTs diameter distribution obtained from the analysis of the electron diffraction patterns of SWCNTs and their geometric mean diameter (μ_g) with **d)** Fe (1.05 nm), **e)** Co (1.06 nm) and **f)** Co-Ni (0.99 nm) as catalyst particles. Image Copyright © 2019 Elsevier [11], used with permission.

We also utilized EDPs of various kinds of SWCNTs to quantitatively analyze the diameter distribution of various types of SWCNTs [52]. For this purpose, 115 to 130 randomly selected individual SWCNTs from each catalyst (i.e. Fe, Co, and Co-Ni) were characterized. The statistics obtained from EDPs for diameter distribution with Fe, Co and Co-Ni SWCNTs have been plotted in Fig. 5.8d, e and f, respectively. Consistent with OAS, we found that there is no significant change in the geometric mean diameter (μ_g) of Fe and Co SWCNTs ($\mu_g \approx 1.05$ nm). However, Fe SWCNTs have broader diameter distribution having geometric standard deviation (σ_g) of 1.23 compared to Co SWCNTs with σ_g of 1.16. The

Fe SWCNTs lie in the range from 0.67 to 2.0 nm with 45% SWCNTs having $d < 1$ nm. On the other hand, Co SWCNTs lie in between 0.78 to 1.65 nm diameter range having 36% SWCNTs with $d < 1$ nm. From electron diffraction analysis, we found that SWCNTs from Co-Ni catalyst have comparatively smaller μ_g of 0.99 nm and narrower diameter distribution (σ_g of 1.15). The abundance of SWCNTs having $d < 1$ nm increased to 57 with Co-Ni. Therefore, a comparative study of SWCNTs from various catalysts through ED technique revealed that Co and Co-Ni can produce narrower diameter distribution compared to Fe catalyst. Such small-diameter SWCNTs having narrow distribution obtained in this work through a scalable FC-CVD method have never been reported before.

5.2.4 Tuning chirality of SWCNTs with catalyst composition

We found that the chirality of as-grown SWCNTs depends on the catalyst composition. The chiral structure of SWCNTs was determined by analyzing more than 115 individual, straight and clean SWCNTs from each sample using ED technique. The results obtained with three catalysts (i.e. Fe, Co and Co-Ni) have been plotted as chirality maps in Fig. 5.9(a-c) along with their corresponding chiral angle distributions in Fig. 5.9(d-f). The representative EDPs of the zig-zag, chiral and armchair nanotubes and their chiral indices i.e. (n,m) are displayed in Fig. 5.9(g-i). The data revealed that 12% of Fe SWCNTs have chirality (8, 6), (9, 5) and (10, 4). Most of the Fe SWCNTs were found close to 1 nm diameter region, however, a small fraction has either very small (≈ 0.67 nm) or large (≈ 1.85 nm) diameter. Moreover, the Fe SWCNTs were found randomly distributed from zig-zag to armchair edges with the mean chiral angle of $16.06 \pm 8.35^\circ$ having 61% of semiconducting nanotubes. This result is consistent with the ferrocene ($\text{Fe}(\text{C}_5\text{H}_5)_2$) based Fe SWCNTs using ethylene as a carbon source [63]. Hence, our result demonstrated that in the FC-CVD method, for the similar composition of catalyst particles, choice of the catalyst precursor has no significant effect in tuning the chirality distribution of SWCNTs.

Interestingly, using Co as catalyst produced a relatively narrow chirality distribution of SWCNTs (Fig. 5.9b) compared to Fe catalyst. 71% of Co SWCNTs lie in the diameter range from 0.9-1.2 nm with 15% enriched with (9, 8), (11, 5) and (9, 7) chiralities. Some specific chiralities, such as (8, 1), (8, 2), (7, 4), (21, 2) and (17, 11) etc. having comparatively small or big diameter, were disappeared when we used Co as a catalyst. However, similar to Fe SWCNTs, Co SWCNTs were also found everywhere in the periodic table of CNTs from zig-zag to armchair edges having 60% semiconducting SWCNTs.

The most promising results were obtained from bimetallic Co-Ni catalyst particles. In this case, 73% of the SWCNTs lie in the diameter range from 0.8-1.1 nm. More importantly, 71% of the SWCNTs lie near the armchair edge in the chiral angle range of $15-30^\circ$ having the mean value of $20.18 \pm 6.08^\circ$. The fraction of semiconducting SWCNTs with Co-Ni slightly increased to 69% compared to the semiconducting ratio of around 60% with pure Fe or Co catalysts. With Co-Ni, 20% of the total SWCNTs have (8, 5), (8, 6) and (9, 5) chiralities. Some specific small diameter SWCNTs such as (6, 4), (6, 5), and (6, 6) were only found with Co-Ni catalyst. Surprisingly only a single carbon nanotube was found with zig-zag structure of (12, 0). The possible reason behind getting the narrow chirality with bimetallic Co-Ni might be the activation of small area on catalyst surface due to synergistic effects of two different metals, as has been proposed in

the substrate supported-CVD processes [64]. The higher fraction of near-armchair SWCNTs might be attributed to their thermodynamic stability as has been observed in the chiral-selective growth of SWCNTs [65]. Hence, we concluded that the bimetallic Co-Ni catalyst is more effective for chirality control compared to monometallic Co or Fe. Moreover, similar to supported-CVD processes [28,29] chirality of SWCNTs can be tuned in the FC-CVD method with the change in the catalyst composition. However, for chirality selective growth of SWCNTs in FC-CVD a more precise control on the size and structure of catalyst particles is needed to investigate. Interestingly, by comparison of the chirality distribution of spark discharge based Fe SWCNTs with ethylene produced in this dissertation and in our earlier work with CO [33] as carbon source revealed that carbon source plays a significant role in determining the chirality of as-synthesized SWCNTs. The possible reason could be different products resulting from CO and ethylene decomposition at elevated temperature inside the FC-CVD reactor.

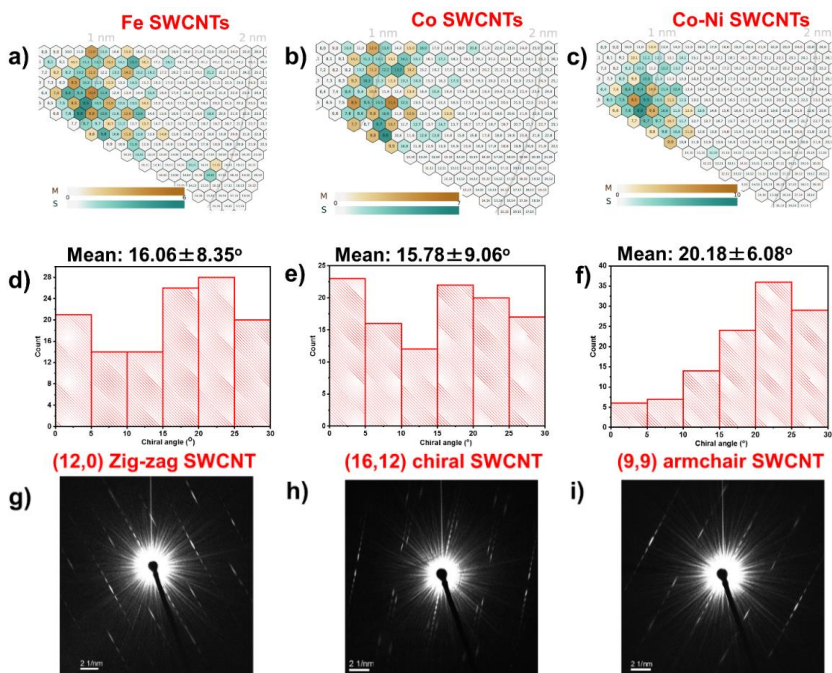


Fig. 5.9. Chirality distribution maps and chiral angle distribution of **a) & d)** Fe SWCNTs, **b) & e)** Co SWCNTs **c) & f)** Co-Ni SWCNTs. Selective EDPs of **g)** (12, 0) zig-zag SWCNT, **h)** (16, 12) chiral SWCNT, and **i)** (9, 9) armchair SWCNT. Image Copyright © 2019 Elsevier [11], used with permission.

5.2.5 SWCNT-TCFs performance and catalyst composition

The opto-electronic performance of SWCNT-TCFs is mainly determined by the morphology and molecular structure of individual SWCNTs in the sample [66]. As we discussed in **chapter 5** of this thesis, that the change in catalyst composition significantly affects yield, morphology and chirality of SWCNTs. Therefore, for comparison of opto-electronic performance of Fe, Co and Co-Ni SWCNT-TCFs, we fabricated SWCNT films with various thicknesses and transparencies by collecting samples for different collection times. For better opto-

electronic performance, SWCNTs having a high fraction of individual nanotubes, large tube diameter and long bundle length are preferred [7]. A set of data points at different % T versus sheet resistance (R_s) of the SWCNT films with various catalysts is shown in Fig. 5.10. The data points were non-linearly fitted by the relation between sheet resistance and optical transmittance (*i. e.* $R_s = -1/K \ln T$). In this relation, K is a constant of proportionality depending on the opto-electronic properties of SWCNTs in the film [43].

It is obvious from Fig. 5.10a, that the pristine R_s value for the 90%T (at 550 nm wavelength) Co-Ni SWCNT-TCF is 1090 Ω/sq which is much better than Fe having 1512 Ω/sq and Co having 1704 Ω/sq at the same value of film transmittance. From the comparison of SWCNT morphology with various catalysts, it can be concluded that Co-Ni SWCNT-TCFs have the lowest R_s value because of their comparatively better quality, long bundle length, low defects and small bundle diameter. After AuCl_3 doping @ 90% transparency, R_s values reduced by a factor of ~ 6 and corresponding R_s value of AuCl_3 doped Co-Ni, Fe and Co SWCNT-TCFs is 172, 243, and 274 Ω/sq , respectively. However, we could not observe any appreciable difference in the doping factor with the change in catalyst.

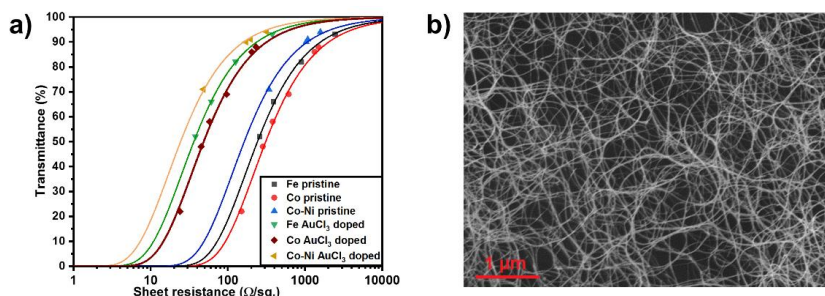


Fig. 5.10. a) The sheet resistance (Ω/sq) versus optical transmittance (%) (at 550 nm wavelength) of pristine and AuCl_3 doped Fe, Co and Co-Ni SWCNT-TCFs. **b)** Representative SEM image of 97% transparent SWCNT-TCF having a randomly oriented network of clean and long SWCNTs. Image Copyright © 2019 Elsevier [11], used with permission.

5.3 Improving conductivity of SWCNT-TCFs by sulfur addition

In **chapter 3** we briefly discussed that sulfur is one of the most important growth promoters for growing SWCNTs, especially for the fabrication of high-performance TCFs applications. In this dissertation (**publication-III**) we have for the first time systematically investigated the roles of sulfur on various growth characteristics of SWCNTs including their yield, morphology, chirality and film conductivity using *ex-situ* catalyst particles. The pre-made catalyst particles synthesized in our SDG technique, benefited us to explore independently the roles of sulfur on morphology and structure of SWCNTs, without affecting catalyst formation from their nucleation stage which is possible in conventional FC-CVD methods [48,49]. The change in catalyst composition and structure with sulfur addition itself can largely influence the growth mechanism of SWCNTs and can make sulfur role on SWCNT growth more ambiguous. Hence,

for a deep understanding of sulfur's role in FC-CVD, sulfur addition should be more controllable in SWCNTs synthesis. The experimental conditions for the synthesis of sulfur-assisted SWCNTs are the same as in **publication-II** except the addition of 0-10 ppm H_2S as a sulfur source. H_2S served as a sulfur source to make the synthesis process well-controlled and purely in gas-phase. For the purpose of the comparative study of the catalyst composition effects on sulfur-assisted FC-CVD, two catalysts i.e. Fe and Co were utilized.

5.3.1 Variation in yield and diameter of SWCNTs

At each step throughout the experiments, to eliminate the possible effects of catalyst size and concentration on SWCNTs growth, the NSDs of catalyst particles (Fig. 5.5a) were carefully fixed by DMA. We found the SWCNT yield is highly sensitive to the sulfur concentration. With an increase in H_2S amount, the SWCNT yield increases first and then it starts decreasing. The yield was quantified on the basis of the transmittance of as-produced SWCNT films (under a fixed area of the filter and collection time) with 1-10 ppm H_2S concentrations to the yield at 0 ppm H_2S as has been shown in Fig. 5.11a. With the appropriate amount of sulfur addition, the SWCNTs yield can be improved by around 2.5 times. The optimum H_2S concentrations for the maximum yield are different for Fe and Co catalysts, i.e. 1 ppm for Fe-SWCNTs and 2 ppm for Co-SWCNTs. This diversity of the yield indicates that effect of sulfur on SWCNT growth is also catalyst composition dependent. Afterwards, yield declined with the addition of more amount of H_2S , which means the excess H_2S will suppress the yield, e.g. 10 ppm H_2S can decrease the yield to ~15% of that without H_2S . Moreover, the total NC of SWCNTs from DMA versus H_2S concentration (Fig. 5.11b) follows a similar trend as the yield variation. The total NC of SWCNTs increased by ~37% with the introduction of 1 ppm H_2S for Fe and by ~34% with 2 ppm H_2S for Co catalysts. Afterward, the total NC of SWCNT starts decreasing with the increase of H_2S amount. Compared to that without H_2S , around 90% reduction in total NC of SWCNTs with 10 ppm H_2S was recorded for both Fe and Co catalysts. This variation trend of total NC suggests that the sulfur can tune the proportion of active catalyst nanoparticles. Hence, real-time measurements of the NC of SWCNTs showed that H_2S addition first enhances the growth of SWCNTs up to a certain fixed amount then begins to suppress SWCNT growth.

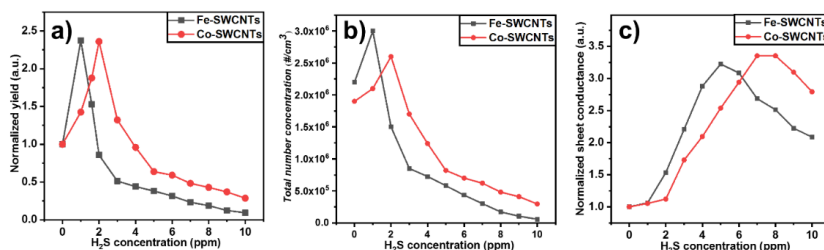


Fig.5.11. a) Normalized yield of SWCNTs with Fe and Co as the catalyst. **b)** Total number concentration ($\# \text{cm}^{-3}$) of Fe- and Co-SWCNTs measured in gas-phase by DMA. **c)** The change in the sheet conductance of 90% transparent (@ 550 nm wavelength) pristine Fe- and Co-SWCNT-TCFs with the addition of 0-10 ppm H_2S concentration, showing the highest conductance at 5 ppm for Fe-SWCNTs and at 8 ppm H_2S for Co-SWCNTs. Image Copyright © 2019 Elsevier [12], used with permission.

More importantly, we observed H_2S addition effectively tune the conductivity of SWCNT based TCFs. As shown in Fig. 5.11c, the SWCNT film conductivity increases first and then decreases with the increase in H_2S amount. For both catalysts, at optimum H_2S concentration, the conductivity of the pristine SWCNT films drastically increased by a factor of 3. The optimum H_2S concentration to acquire maximum sheet conductance was 5 ppm for Fe-SWCNTs and 8 ppm for Co-SWCNTs.

H_2S addition has also pronounced effect on diameter of the SWCNTs. It is obvious from the OAS (Fig. 5.12a and b) of as-synthesized SWCNT films that S_{11} peak shifts from smaller wavelength region (1322 nm) to larger wavelength region (1525 nm) with the addition of 1 ppm H_2S . Using Kataura plot and OAS, the mean diameter of SWCNTs was calculated and we found that for both Fe and Co catalysts, the mean diameter of SWCNTs increased from 1.05 nm to 1.26 nm with H_2S addition. However, from 2-10 ppm H_2S , apparently there is no shift of S_{11} compared to 1 ppm H_2S , disclosing that SWCNT diameter is not continuously varying with H_2S amount (from 1 to 10 ppm). The enhancement in SWCNTs diameter was also observed by Raman spectra (using 633 nm laser) of SWCNT films. It can be seen from Fig. 5.12a that without H_2S , SWCNTs which are in resonance with the applied laser were found in the range of 0.8-1.7 nm. However, with the addition of H_2S (1 to 10 ppm), SWCNTs having a diameter (d) greater than 1.1 nm were detected. Furthermore, with sulfur addition, an increase in the I_G/I_D ratio of SWCNTs (Fig. 5.12d) indicated the enhancement in quality of SWCNTs. Hence, sulfur apart from increasing diameter of SWCNTs is also useful to decrease the number of defects in SWCNTs or to decrease the amount of amorphous carbon in the sample.

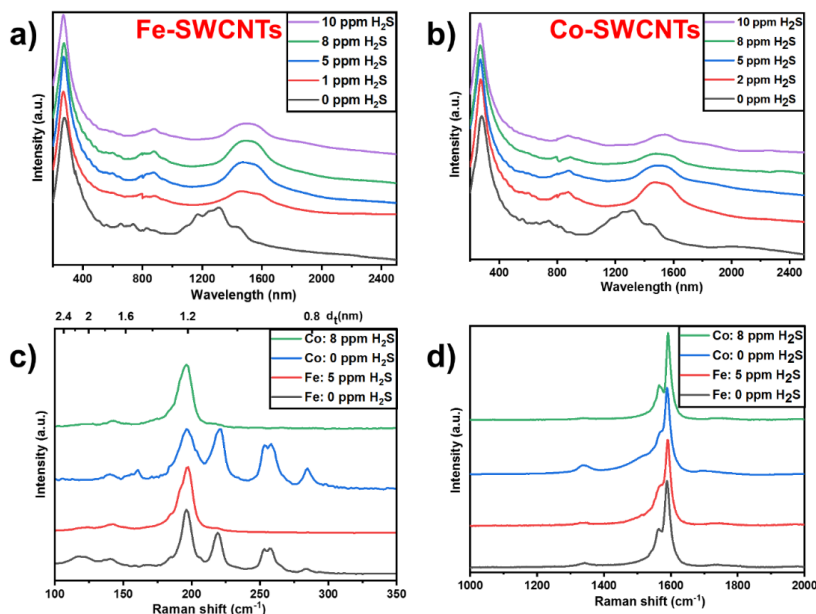


Fig. 5.12. The OAS of **a)** Fe-SWCNTs & **b)** Co-SWCNTs, indicating a very clear shift towards larger diameter SWCNTs with sulfur addition. **c)** Corresponding RBM of Raman spectra (using 633 nm laser) and **d)** the G and D mode of Raman spectra revealing an increase in I_G/I_D ratio of Fe-SWCNTs from 13 to 19 and 11 to 21 in case of Co-SWCNTs. Image Copyright © 2019 Elsevier [12], used with permission.

The diameter distribution and μ_g of the SWCNTs were quantitatively analyzed by ED technique [52]. For the said purpose, around 120 individual SWCNTs were randomly characterized from each sample. The results obtained from ED data analysis for both Fe and Co-SWCNTs are plotted as diameter distribution in Fig. 5.13. A reasonable increase from 1.06 nm to 1.26 nm in μ_g of Fe-SWCNTs was observed with the 5 ppm H_2S addition. The Fe-SWCNTs with H_2S were found in comparatively narrow diameter range from 0.95-1.95 nm compared to 0.70-1.95 nm without H_2S . Similarly, μ_g of Co-SWCNTs increased from 1.05 nm to 1.24 nm with 8 ppm H_2S addition. But in this case, diameter distribution became wider with H_2S addition. Since the large diameter SWCNTs have a small bandgap, therefore formation of large diameter SWCNTs after sulfur addition is one of the possible reasons for the improvement in conductivity of the SWCNT-TCFs with sulfur addition. Therefore, all the characterizations applied for the measurement of the diameter of SWCNTs i.e. optical absorption spectroscopy, Raman spectroscopy and ED techniques disclosed that the addition of sulfur significantly increased diameter of SWCNTs.

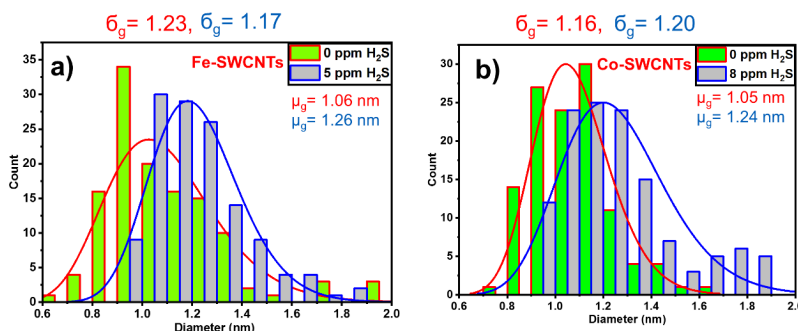


Fig. 5.13. Quantitative analysis of variation in SWCNTs diameter distribution with and without H_2S at optimized conditions using ED technique for **a)** Fe-SWCNTs and **b)** Co-SWCNTs. Image Copyright © 2019 Elsevier [12], used with permission.

5.3.2 Mechanism behind sulfur-assisted growth of SWCNTs

The variation in yield and diameter of CNTs with the addition of sulfur have been previously reported in the FC-CVD growth processes [67,68]. The mechanism proposed in other works is that the sulfur changes the size and composition of the catalyst nanoparticles by the formation of a sulfur-enriched layer on the catalyst surface. However, the *in-situ* catalyst synthesis makes it hard to understand the concrete role of sulfur. In our case, we did not observe a significant changes in either catalyst particle size or composition with the addition of H_2S , which is distinct from the results from other reported works [67,68]. For comparison, we measured the size of catalyst particles using HR-TEM micrographs and found that the size distribution of catalysts particle is fairly consistent with and without sulfur addition (Fig. 5.14c). Moreover, EDS and XPS analysis were carried out to investigate the effect of sulfur on catalyst composition. From EDS analysis of Fe catalyst particles with H_2S , we could not find any detectable sulfur peak in the spectrum, indicating that their composition is sulfur independent (Fig. 5.14b).

On the other hand, XPS analysis of SWCNT films (Fig. 5.15), indicated the presence of both Fe (0.04 at. %) and sulfur (0.05 at. %) peaks. The Fe 2p peaks

(Fig. 5.15a) in XPS are found at roughly 707.2 ($2p_{3/2}$) and 720.1 eV ($2p_{1/2}$) which are consistent with metallic Fe. For sulfur in Fig. 5.15b, there are two broad S 2p features around 163.6 eV and 168.9 eV. These binding energy features are most likely related to S-S bonding or C-S bonding, whereas the 168.9 eV feature could be related to C-SO_x type bonding [69,70]. However, iron sulfide or sulfur-containing iron alloy can be mostly ruled out since no direct Fe-S bonding at S2p binding energies between 161-163 eV is observed in XPS. Therefore, we propose that H₂S mainly influence the interaction between the metal catalyst and carbon. Thermodynamically, H₂S adsorption on the catalyst surface is a favorable reaction on such a high temperatures. Therefore, it can decompose into the activated fragments like -SH and -H species [71,72].

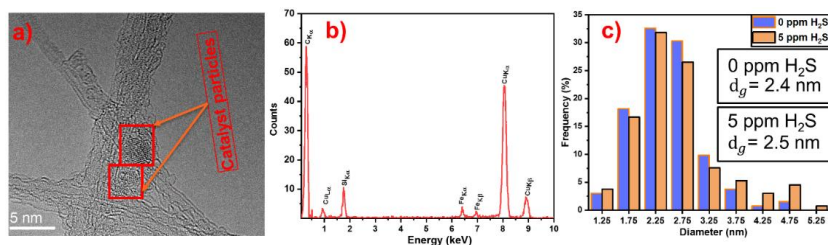


Fig. 5.14. **a)** A typical HR-TEM image of Fe catalyst particles used for the analysis of the sulfur effect on the NSDs of catalyst particles and for EDS analysis. **b)** EDS of Fe catalyst nanoparticle in sulfur-assisted SWCNTs indicating that their composition is independent of sulfur. **c)** NSD of catalyst particles obtained from HR-TEM measurements. Image Copyright © 2019 Elsevier [12], used with permission.

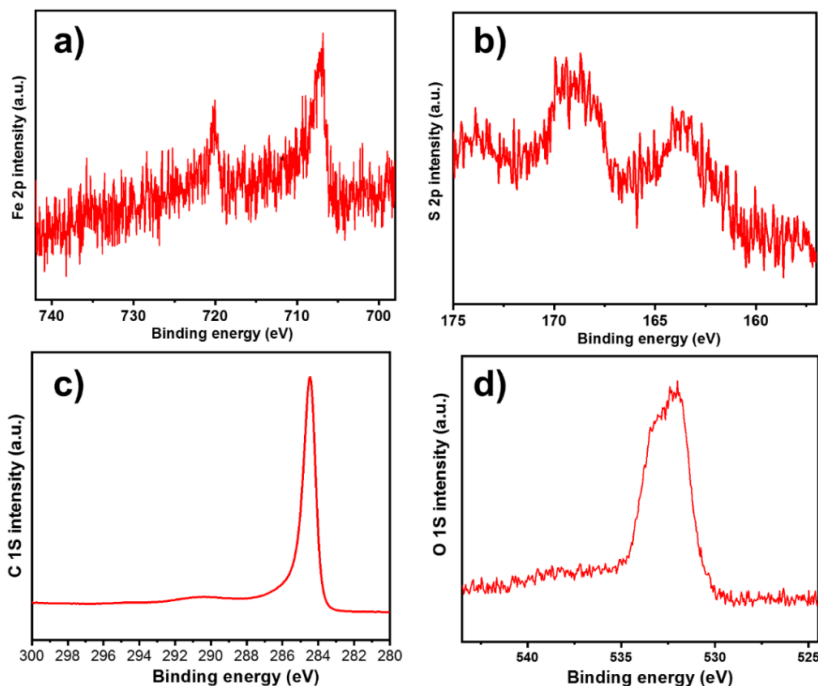


Fig. 5.15. **a)** The Fe 2p (0.04 at. %), **b)** S 2p (0.05 at. %), **c)** C 1s (98.6 at. %) and **d)** O 1s (1.13 at. % as an impurity) XPS from sulfur-assisted SWCNT film. Image Copyright © 2019 Elsevier [12], used with permission.

These activated species on catalysts surface might be providing more active catalyst sites for the growth of SWCNTs, resulting in an increase in their length and yield. In addition, the large active catalyst surface area with sulfur might also result in the formation of large diameter SWCNTs [68,73]. On the other side, the excess amount of sulfur may result in an imbalance between the carbon dissolution and its precipitation, which can decrease the activity of the catalyst and even can deactivate them. Therefore, the yield will decline with excessive H_2S .

5.3.3 Change in morphology of SWCNTs with sulfur

As discussed in **section 5.2.3**, the bundle length and bundle diameter are two substantial parameters that have a pronounced effect on opto-electronic performance of SWCNT-TCFs. Therefore, we investigated the effects of sulfur addition on SWCNTs bundle length and bundle diameter distributions. The l_b of both Fe- and Co-SWCNTs roughly increased by 25% with the addition of an optimized amount of H_2S (Fig. 5.16a & b). As mentioned above, sulfur may lower the barrier of carbon precipitation from catalysts and increase the SWCNTs growth speed to produce longer SWCNTs bundles. It's worth noting that our results provide statistical data on bundle length distributions of SWCNTs with and without sulfur addition. In the existing literature for most of the cases, without adding sulfur no CNT or very short CNTs have been reported [74,75] which made this comparison practically impossible. For TCFs applications, at the same transmittance, the long bundle length nanotubes show better performance due to less number of contact junctions, and hence improving overall opto-electronic performance of the film.

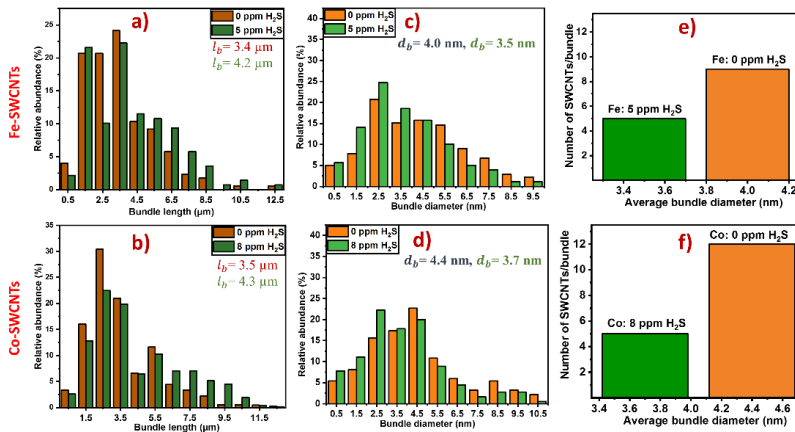


Fig. 5.16. Comparison in bundle length distribution of **a)** Fe-SWCNTs (0 & 5 ppm H_2S) and **b)** Co-SWCNTs (0 & 8 ppm H_2S). Corresponding comparison in bundle diameter distribution of **c)** Fe-SWCNTs and **d)** Co-SWCNTs. The number of **e)** Fe-SWCNTs and **f)** Co-SWCNTs in average bundle size at optimized conditions with and without sulfur addition. Image Copyright © 2019 Elsevier [12], used with permission.

The bundle diameter distributions with and without sulfur addition has been provided in Fig. 5.16c & d for bot Fe- and Co-SWCNTs, respectively. We found that the number of individual SWCNTs in the sample significantly increased with the sulfur addition from 13% to 21%, and from 11% to 18% for Fe- and Co-SWCNTs, respectively. Additionally, the bundle diameter distribution revealed that sulfur addition reduced d_b for Fe-SWCNTs by 0.5 nm and for Co-SWCNTs

0.7 nm. More importantly, from Fig. 5.16e & f, it can be seen that the number of SWCNTs in an average bundle size in the case of Fe-SWCNTs reduced from 9 to 5 with the introduction of 5 ppm H_2S , whereas for Co-SWCNTs it reduced from 12 to 5 with 8 ppm H_2S addition. Since narrower bundles and a higher fraction of individual nanotubes was found with H_2S addition therefore, sulfur-assisted SWCNT-TCFs could exhibit better opto-electronic performance [7].

5.3.4 Sulfur modulates the chirality of SWCNTs

The chiral structure of SWCNTs was determined by ED method. To the best of our knowledge, we reported for the first time the effect of sulfur addition on SWCNT's chirality distribution from ED technique. In contrast, previously, the synthesis of high-quality and clean SWCNTs without sulfur addition has remained a big challenge for making this comparison possible. Thus, only absorption, Raman and photoluminescence (PL) spectroscopies were adopted to determine SWCNT chiralities, among which Raman and PL techniques have severe drawbacks, leading to incomplete chirality maps [76]. The chirality maps from ED of Fe-SWCNTs and Co-SWCNTs are shown in Fig. 5.17. ED analysis revealed that Fe-SWCNTs for both 0 and 5 ppm H_2S are randomly distributed from zig-zag to armchair edges. However, it can be seen in the chirality map (Fig. 5.17a) with 0 ppm H_2S , most of the SWCNTs are clustered around 1 nm region with 45% having $d < 1$ nm. With the addition of 5 ppm H_2S the SWCNTs enclosed in the rectangle in Fig. 5.17a having d roughly < 0.95 nm, were totally disappeared. With 5 ppm H_2S 17% of the SWCNTs have chiralities (9, 6), (10, 4) and (10, 6) compared to most abundant (12%) chiralities (10, 4), (8, 6) and (9, 5) without addition of H_2S . Some large diameter SWCNTs for example (16, 4), (16, 10) and (18, 8) etc. marked in Fig. 5.17b, were only found with H_2S addition.

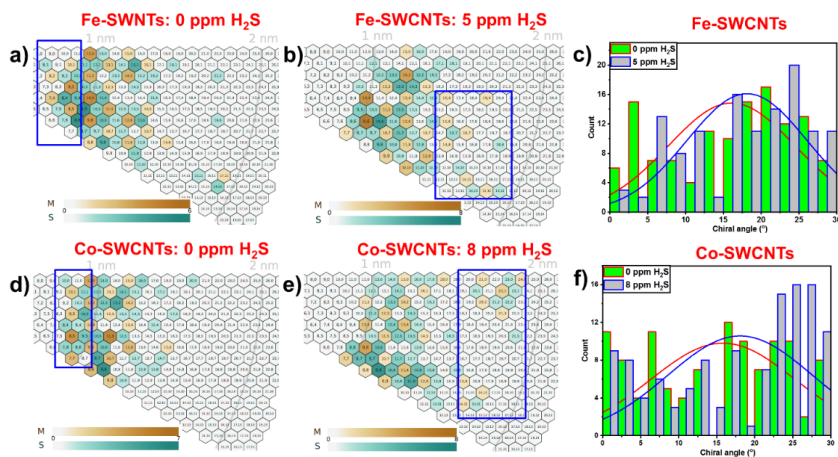


Fig. 5.17. A comparison in chirality distribution of SWCNTs with and without sulfur addition at optimum conditions with **a)** and **b)** Fe-catalyst, **d)** and **e)** Co-catalyst. Corresponding chirality angle distributions showing the effect of sulfur on **c)** Fe-SWCNTs and **f)** Co-SWCNTs. Image Copyright © 2019 Elsevier [12], used with permission.

Importantly, sulfur did not tune too much the chiral angle distribution (Fig. 5.17c) of SWCNTs and a moderate change in the mean chiral angle from

16.06 ± 8.350 to 18.11 ± 7.920 was observed. In addition, the ratio of semiconducting SWCNTs slightly decreased from 61% to 59% with addition of 5 ppm H_2S .

For Co-SWCNTs with 0 and 8 ppm H_2S the major changes in (n,m) indices have been highlighted with the rectangles in Fig. 5.17d and e. The most abundant chiralities (16%) with 8 ppm H_2S are (9, 8), (9, 7) and (11, 5) compared to (9, 8), (9, 7), (11, 9) with 0 ppm H_2S . It's worth mentioning that with the addition of sulfur for Co catalyst we obtained relatively higher fraction (8%) of the zig-zag (n,0) SWCNTs which are considered to be more difficult to synthesize [65]. Otherwise, similar to Fe-SWCNTs, there are negligible changes in the mean chiral angle (Fig. 5.17f) as well as the ratio of semiconducting nanotubes with the addition of sulfur for Co catalyst. Hence, the ED analysis quantitatively revealed that there is a shift in smaller to larger diameter SWCNTs with the sulfur addition, but it is not an effective promotor for the chirality control of SWCNTs. This result is in contradiction to many studies in the literature for supported-CVD processes, where sulfur-containing compounds have been employed as a growth promoter to get high selectivity as well as for tuning metallic to semiconducting ratio of the SWCNTs [77,78]. The reason might be the use of inadequate measurement methods for chirality determination in the earlier works.

5.3.5 Highly conductive SWCNT-films with sulfur addition

From the above analysis, we conclude that an appropriate amount of sulfur increased the diameter of SWCNTs, elongated the average bundle length, reduced the average bundle size and enhanced the quality of SWCNTs, which can give the SWCNT films better opto-electronic performance. The plots of R_s versus T are shown in Fig. 18a for the comparison of the opto-electronic performance of SWCNT-TCFs with and without H_2S addition. The pristine Fe- and Co- SWCNT films without H_2S at 90% $T_{550 \text{ nm}}$, the R_s is 1512 Ω/sq and 1704 Ω/sq respectively. The conductivity of the pristine SWCNT-TCFs drastically decreased by 6 times after doping with AuCl_3 . The doped Fe- and Co-SWCNT films have R_s values as low as 243 Ω/sq and 274 Ω/sq at 90% $T_{550 \text{ nm}}$, respectively.

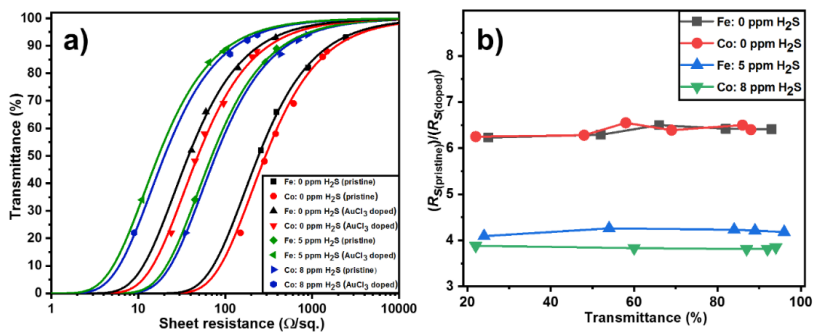


Fig.5.18. a) A plot of sheet resistance of SWCNT-TCFs vs. % transmittance at 550 nm wavelength under the optimized growth conditions (with and without the addition of sulfur) with pre- and post- AuCl_3 doping. **b)** A reduction in the ratio of pristine to doped sheet resistance values of Fe- and Co-SWCNTs with sulfur addition at various % transmittance of the TCFs. Image Copyright © 2019 Elsevier [12], used with permission.

However, with sulfur addition at optimized conditions, the R_s values of pristine SWCNT-TCFs significantly reduced by a factor of approximately 3 for both

Fe- and Co-SWCNTs. The R_s values with sulfur for 90% transparent TCFs for Fe- and Co-SWCNTs are 469 Ω/sq and 508 Ω/sq , respectively. The reduction of R_s value with sulfur could be the result of large diameter SWCNTs, long bundle length, better quality and small bundle size. It's worth noting, that the doping factor with sulfur addition reduced from ~ 6 to ~ 4 (Fig. 18b). The difference of doping factors can be attributed to the small bandgap of large diameter SWCNTs and in a decrease in the number of contact junctions due to long bundle length with sulfur addition. The minimum R_s value for doped Fe- and Co-SWCNTs at 90% $T_{550\text{ nm}}$ was found 116 Ω/sq and 132 Ω/sq , respectively. SWCNT-TCFs having sheet resistance in the range 100-200 Ω/sq at 90% $T_{550\text{ nm}}$ can be utilized for touch sensor applications.

5.4 Simultaneous growth of 0D- 1D-2D carbon nanostructures

The single step growth of carbon nanostructure including 0D-fullerene, 1D-CNT and 2D-graphene has remained a subject of great interest due to their widespread potential applications [79,80]. These low-dimensional carbon nanostructures (i.e. fullerene, CNT and graphene) share the same structure of sp^2 bonded carbon atoms. Yet, their synthesis differs in many aspects, including the shape and size of the catalyst. In **publication-IV**, we demonstrated a single-step FC-CVD technique for the substrate-free growth of 0D-1D-2D carbon nanostructures. The experimental conditions for the growth of hybrid structure are the same as utilized in **publication-III** except amount of H_2S which is 2 ppm. Furthermore, we tuned the amount of H_2 in the range 50-120 sccm to control relative number density of graphene nanoflakes in the sample. Our technique is unique because it provides a direct and dry route for the deposition of as-produced material practically on any substrates [44] under ambient temperature and pressure for different applications or the film of desired thickness can be directly collected on low-adhesion membrane filter, which can be easily transferred on the targeted substrate through well-established room temperature, dry-press transfer technique [43]. It opens up new avenues towards the ultra-fast manufacturing of the 0D-1D-2D hybrid material at industrial scale and provides scientific community new insights into the synthesis mechanism of low dimensional carbon nanostructures especially that of graphene.

5.4.1 Morphology and structure of the hybrid material

The morphology and structure of the as-produced hybrid material were studied by HR-TEM, STEM and AFM. The formation of 0D-1D-2D is directly evidenced by lattice-resolved STEM and electron diffraction experiments, corroborated by AFM. Typical HR-TEM images of hybrid structures are shown in Fig. 5.19a. The HR-TEM images revealed that we have simultaneously 0D, 1D and 2D carbon nanostructures in the sample. Since the structure and growth mechanism of 0D-1D hybrid carbon nano structures i.e. carbon nano bud (CNB) in FC-CVD method has been widely studied and well-understood [81,82]. Therefore, in this work we emphasized on the gas-phase synthesis of 1D-2D hybrid carbon nanostructures. The crystallographic structure of 1D-2D hybrid was investigated by selected area electron diffraction technique. The EDP of some of the

representative hybrid structure are provided in Fig. 5.19e and f whereas, EDP of an individual SWCNT has been shown in Fig. 5.19g. EDPs of 1D-2D hybrid structure concurrently displayed features of both SWCNTs and graphene.

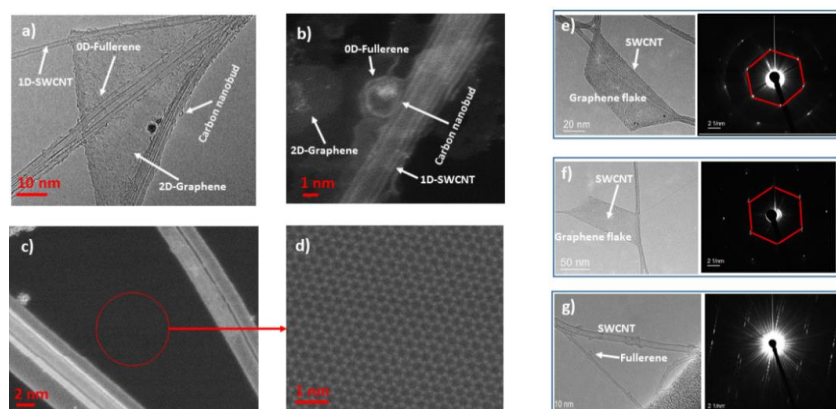


Fig. 5.19. **a)** Typical HR-TEM image of 0D, 1D and 2D carbon nanostructures **b)** STEM image of hybrid structure **c)** STEM image of 1D-2D hybrid structure **d)** high-resolution STEM image of graphene flake and **e), f)** EDPs of 1D-2D hybrid structure and **g)** EDP of an individual SWCNT.

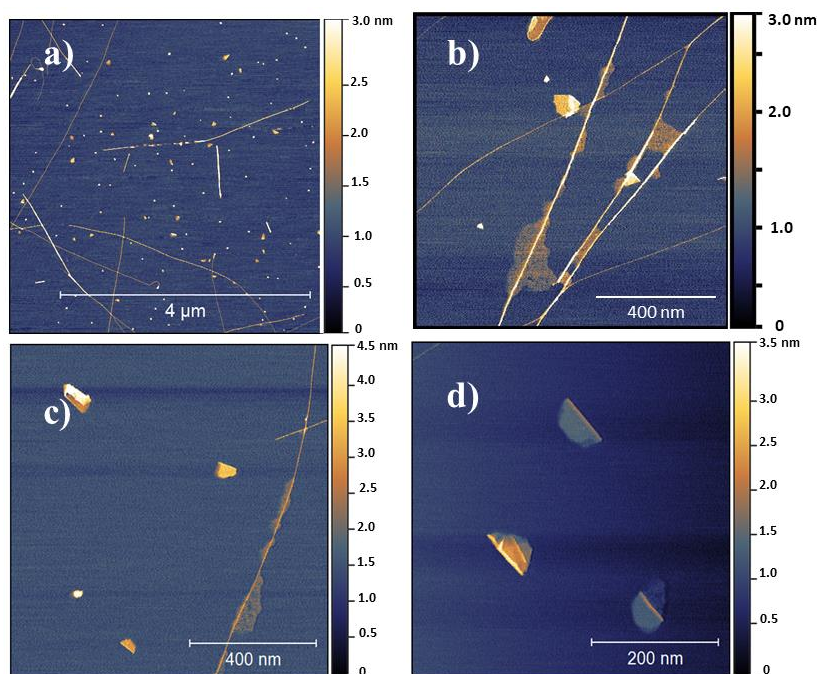


Fig. 5.20 a and d). AFM images of some of the isolated graphene nano flakes grown in the FC-CVD method without any attachment with CNTs. **b)** Graphene nano flakes bridging between adjacent CNTs bundles and **c)** An example of individual and attached graphene nano flakes with CNTs.

In particular, in some cases the manifold diffraction spots arising from graphene flakes indicates an existence of two or more layers twisted into certain

angles. The reason might be either we don't have purely single-layer graphene or while moving in gas-phase from the FC-CVD reactor to the collection point, a single-layer is wrinkled to form multi-layer graphene-nanoflake. Furthermore, the graphene-nanoflakes were found edge-enriched (*ca.* surface area 3100 nm²) which might offer more sites for functionalization of dopant atoms/molecules. Since, our process provides single-step in-situ growth of the hybrid material, therefore it has higher possibility of covalent C-C bonding in between 1D and 2D structures. The more direct evidence of formation of 1D-2D hybrid structure was obtained by atomic-resolution STEM. Fig. 5.19b and c show typical STEM images of as-synthesized 0D-1D-2D and 1D-2D hybrid structures respectively. In Fig. 5.19c we can clearly see a single layer graphene underneath SWCNTs. A magnified image of the graphene flake (Fig. 5.19d) clearly shows hexagonal lattice of graphene which confirmed the formation of free-standing, graphene nanoflakes through FC-CVD method. Furthermore, from STEM and AFM images (Fig. 5.20b and c) it is obvious that some of the graphene flakes are wrapped around SWCNTs and some of them are making bridge between adjacent SWCNTs. Surprisingly, AFM results also revealed that we have some isolated graphene flakes (Fig. 5.20) and it is not necessary that they are always wrapped around or supported by SWCNTs.

5.4.2 Role of hydrogen

The synthesis of 1D-2D hybrid structure via purely gas-phase method is unexpected here. As it is commonly believed in the existing methods for graphene synthesis (e.g. CVD growth on Cu foils [83] or epitaxial growth on Ge(110) wafer [84]) that the substrate is always required for graphene growth. However, we believe that the formation of poly aromatic hydrocarbons (PAHs) through the pyrolysis of hydrocarbons [85] and then their chain polymerization play leading role in the initial formation of graphene nanoflakes. The addition of more active carbon species at the edges of new-born graphene nanoflakes increases the size of the flakes. As the variation in H₂ concentration can suppress or enhance the pyrolysis of hydrocarbons, therefore we tuned H₂ flow in the FC-CVD reactor in the range 50-120 sccm. Interestingly, we observed pronounced effect of H₂ concentration on the relative abundance of graphene-nanoflakes in the 1D-2D hybrid structure. As shown in Fig. 5.21 a-c, increasing H₂ from 50 sccm to 120 sccm significantly change the amount and size of graphene-nanoflakes in the samples. The highest amount of graphene is from the 80 sccm H₂, whereas the graphene nanoflakes were disappeared when H₂ flow exceeds 120 sccm. Although the relative abundance of graphene-nanoflakes is very sensitive to the H₂ amount, but no obvious difference was found in optical characterizations (UV-Vis-NIR and Raman spectroscopy) as shown in Fig. 5.21d-f. Based on the Kataura plot and OAS, the mean diameter of SWCNTs was calculated as 1.2 nm and from Raman spectra we found that hybrid material has very high-quality (IG /ID ~ 15 to 20) and low defects.

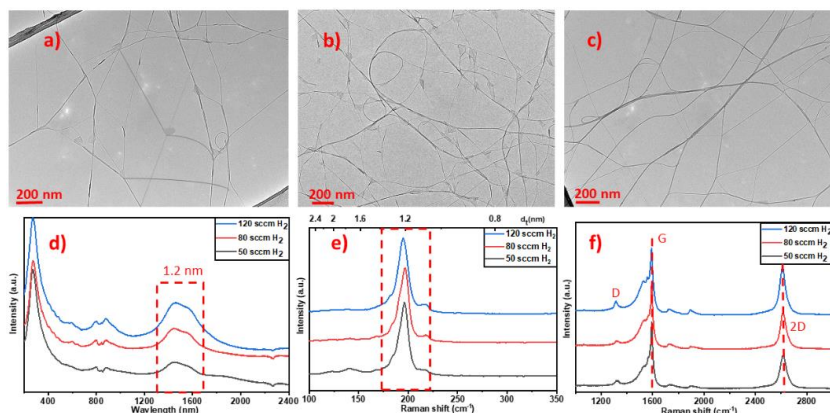


Fig.5.21. **a)-c)** HR-TEM images of oD-1D-2D hybrid material with 50, 80 and 120 sccm of H_2 indicating a higher number density of graphene flakes compared to CNTs with 80 sccm and lower with 120 sccm. Corresponding **d)** OAS and **e)** RBM of Raman spectra showing negligible effect on the diameter of SWCNTs with H_2 variation. **f)** G and D mode of Raman spectra indicating high-quality ($I_G/I_D \sim 15-20$) of SWCNTs and graphene.

5.4.3 Universality of the growth process

The synthesis of graphene nanoflakes has been realized in other FC-CVD systems with various catalysts and carbon sources. It includes both through pre-made catalyst particles and in-situ catalyst synthesis processes. The growth has been observed in Fe, Co, Ni, Co-Ni catalysts from spark discharge generator with C_2H_4 as a carbon source [11] and from Fe catalyst particles obtained from in-situ decomposition of ferrocene ($FeCp_2$) with C_2H_4 [63], C_2H_5OH [48] and CH_4 as carbon sources (see Table 5.1). However, it's worth mentioning that in all these systems growth conditions of purely CNTs and graphene-CNTs hybrid material are different and one can get graphene-CNTs hybrid by precisely controlling growth parameters. These results suggest that this process has strong universality and also support the proposed mechanism that the active carbon species from pyrolysis of carbon sources directly add to the open edge sites for gas-phase graphene synthesis. Few selected HR-TEM images of the hybrid material obtained using various recipes and set-ups are provided in Fig. 5.22.

Table 5.1

FC-CVD set-ups for the growth of CNT or CNT-Graphene (CNT-Gr) hybrid.

Catalyst precursor	C_2H_4	CO	C_2H_5OH	CH_4
Fe-spark	CNT- Gr [11]	CNT [33]		
Fe- $FeCp_2$	CNT- Gr [63]	CNT [86]	CNT-Gr [48]	CNT-Gr
Ni-spark	CNT-Gr [11]			
Co-spark	CNT- Gr [11]			
Co-Ni spark	CNT-Gr [11]			

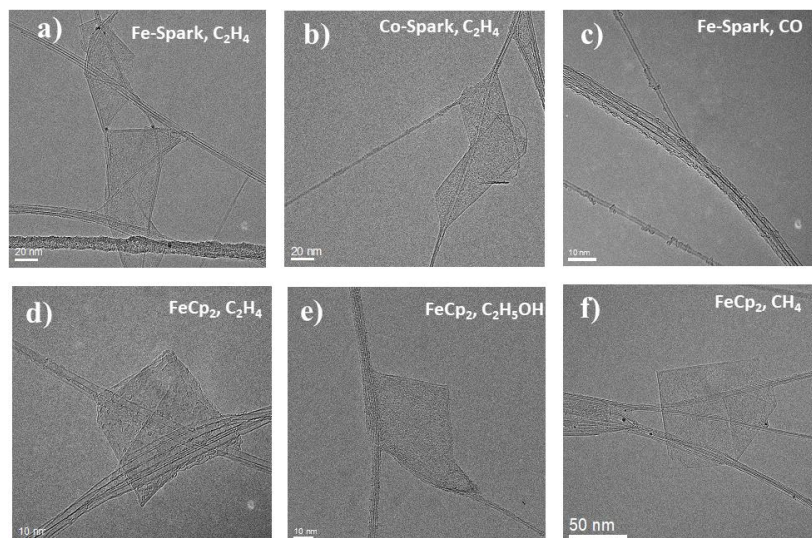


Fig. 5.22. Gas-phase synthesis of SWCNT-graphene hybrid from **a)** Fe-spark, C_2H_4 [11], **b)** Co-spark, C_2H_4 [11], **d)** Fe-FeCp₂, C_2H_4 [63], **e)** Fe-FeCp₂, C_2H_5OH [48] and **f)** Fe-FeCp₂, CH_4 indicating a strong universality of the process. Whereas **c)** Fe-spark, CO [86] produced SWCNTs without graphene flakes.

However, when we used carbon monoxide as a carbon source we were not able to produce simultaneously SWCNTs and graphene nano flakes. Typical examples are spark produced Fe catalyst [33] (5.22c) and ferrocene based Fe catalyst [86] along with CO as a carbon source as indicated in Table 5.1. The reason is CO cannot decompose itself without metal catalysts and is not a hydrocarbon which can produce poly aromatic hydrocarbons in the presence of high temperature. Therefore, we conclude that under carefully chosen gas atmosphere with suitable growth conditions one can synthesize graphene flakes in the gas phase without any substrate.

6. Conclusions and outlook

In summary, in this dissertation, we have developed a novel rod to tube design of SDG (R-T SDG) for the time consistent gas-phase synthesis of catalyst nanoparticles. We synthesized a variety of monometallic and bimetallic catalyst particles with R-T SDG which utilized much smaller gas flow rate compared to conventional rod to rod SDG. These particles can be directly applied for the synthesis of SWCNTs and also other nano-carbon materials in FC-CVD. The R-T SDG and FC-CVD systems were online monitored by DMA. The time consistency of the R-T SDG is attributed to its long-term quasi-stability state. Rod to tube electrodes configuration needs a relatively small flow rate (< 2 lpm) of the carrier gas due to the axial flow of the carrier gas at spark discharge generation point which provides higher transport speed and lower probability of the agglomeration of as-produced catalyst particles compared to rod to rod configuration.

We for the first time successfully synthesized SWCNTs in the FC-CVD method using pre-made Fe, Co, Ni, Co-Ni, Co-Fe catalyst particles and ethylene as a carbon source. We quantitatively compared diameter distributions, yield, morphology and chirality of as-synthesised SWCNTs using various types of catalyst particles. It was observed that in FC-CVD method the mean diameter of SWCNTs is independent of catalyst composition if the number size distributions of catalyst particles are consistent. However, their yield, bundle length and chirality is highly sensitive to the catalyst composition. Electron diffraction analysis demonstrated that as-grown SWCNTs from bimetallic Co-Ni catalyst are slightly skewed favouring large chiral angles nanotubes with 71% SWCNTs lying in the range from 15 - 30° . Moreover, fraction of semiconducting SWCNTs from Co-Ni is 69% compared to 61% with other catalysts.

In addition, we systematically investigated the roles of sulfur on the different growth characteristics of SWCNTs. For comparison, firstly we synthesized high-quality SWCNTs without sulfur and after that H_2S was added as a sulfur promoter. Our results showed that the yield of SWCNTs greatly depends on the amount of sulfur promoter and catalyst composition. Sulfur addition enhanced the growth of larger diameter nanotubes and the average diameter of the SWCNTs was increased from 1 to 1.2 nm. Moreover, bundle length of SWCNTs was slightly increased and bundle diameter decreased by sulfur addition. Furthermore, ED analysis revealed that sulfur promoter has little influence in tuning chirality of SWCNTs. We found that sulfur promoter enhanced the performance of SWCNT-TCFs by increasing diameter, average bundle length and

quality of SWCNTs. At the same time, it decreased average bundle size and increased fraction of individual nanotubes. Moreover, the doping ratio of SWCNTs film conductivity was suppressed by sulfur addition. In our case, after doping with AuCl_3 the minimum sheet resistance of sulfur-assisted Fe-SWCNTs film is $116 \, \Omega/\text{sq}$ and Co-SWCNTs film is $132 \, \Omega/\text{sq}$ at 90% $T_{550 \text{ nm}}$.

Furthermore we have developed a single-step, in-situ gas-phase growth process for the free-standing 0D-1D-2D carbon nano structures by using various catalyst particles, carbon sources, and FC-CVD set-ups. Atomic-resolution STEM images of the as-synthesized material confirmed the formation of 0D-1D-2D hybrid carbon nanostructures. The EDPs of 2D material confirmed the formation of substrate-free graphene nano flakes. HR-TEM images revealed that as-synthesized graphene-nanoflakes are edge-enriched and might offer more sites for the functionalization of dopant atoms/molecules. The average size of the graphene flakes in the sample is roughly $70 \times 40 \text{ nm}$ and that of fullerene is 2.2 nm . The relative number density of graphene-nanoflakes can be optimized in the hybrid material by tuning H_2 amount in the FC-CVD reactor. Our method is purely in gas-phase and has potential to be scaled-up for the production of high-quality, single step growth of free-standing 0D-1D-2D carbon nano structures and their dry and direct deposition at industrial scale.

For future research, although we have designed a novel R-T SDG for the production of time consistent pre-made catalyst particles for SWCNTs synthesis, the design needs more improvement so that it can generate catalyst particles with $< 0.5 \text{ lpm}$ flow of the carrier gas. In that case, one might be able to introduce all the generated catalyst particles from SDG to the FC-CVD reactor and that will be a more cost-effective method. Furthermore, one can generate catalyst particles in SDG by using tungsten and other high melting point metals (e.g. platinum) to achieve narrow chirality of SWCNTs in FC-CVD method. Moreover, the addition of oxygen-containing molecules such as O_2 , CO_2 and H_2O in the synthesis process might also be helpful to narrow down the chirality distribution of SWCNTs. In addition, to replace industrial ITO by SWCNT-TCFs further improvement in films performance through optimization of the synthesis parameters is still needed.

In this thesis successful synthesis of single step growth of 0D-1D-2D carbon nano structures is a big breakthrough. But the mechanism behind the growth of graphene nanoflakes without substrate need more investigations. Particularly the role of catalyst size, furnace temperature and wall conditions of the reactor should be studied more systematically. As the process has strong universality, we believe that with the proper optimization of the growth parameters it can be extended for the synthesis of free-standing graphene nanoflakes by the FC-CVD method. This can overcome the difficulties involving in the multi-step growth of graphene at industrial scale and it's multi-step transferring processes from the substrate for further applications.

References

- [1] Z. Wu, Z. Chen, X. Du, J.M. Logan, J. Sippel, M. Nikolou, K. Kamaras, J.R. Reynolds, D.B. Tanner, A.F. Hebard, A.G. Rinzler, Transparent, Conductive Carbon Nanotube Films, *Science* 305 (2004) 1273–1276. doi:10.1126/science.1101243.
- [2] Z. Yao, C.L. Kane, C. Dekker, High-field electrical transport in single-wall carbon nanotubes, *Phys. Rev. Lett.* 84 (2000) 2941–2944. doi:10.1103/PhysRevLett.84.2941.
- [3] C.T. White, T.N. Todorov, Carbon nanotubes as long ballistic conductors, *Nature*. 393(1998) 240–242. doi:10.1038/30420.
- [4] L. Hu, D.S. Hecht, G. Grüner, Carbon Nanotube Thin Films: Fabrication, Properties, and Applications, *Chem. Rev.* 110 (2010) 5790–5844. doi:10.1021/cr9002962.
- [5] W.H. Chiang, M. Sakr, X.P.A. Gao, R.M. Sankaran, Nanoengineering Ni xFe 1-x catalysts for gas-phase, selective synthesis of semiconducting single-walled carbon nanotubes, *ACS Nano*. 3(2009) 4023–4032. doi:10.1021/nn901222t.
- [6] D.S. Hecht, D. Thomas, L. Hu, C. Ladous, T. Lam, Y. Park, G. Irvin, P. Drzaic, Carbon-nanotube film on plastic as transparent electrode for resistive touch screens, *J. Soc. Inf. Disp.* 17/11 (2009) 941–946. doi:10.17660/ActaHortic.2002.575.61.
- [7] K. Mustonen, P. Laiho, A. Kaskela, T. Susi, A.G. Nasibulin, E.I. Kauppinen, Uncovering the ultimate performance of single-walled carbon nanotube films as transparent conductors, *Appl. Phys. Lett.* 107 (2015) 143113. doi:10.1063/1.4932942.
- [8] W.H. Chiang, R.M. Sankaran, Linking catalyst composition to chirality distributions of as-grown single-walled carbon nanotubes by tuning Ni x Fe 1x nanoparticles, *Nat. Mater.* Nov 8 (2009) 882–886. doi:10.1038/nmat2531.
- [9] A.G. Nasibulin, A. Moisala, D.P. Brown, H. Jiang, E.I. Kauppinen, A novel aerosol method for single walled carbon nanotube synthesis, *Chem. Phys. Lett.* 402 (2005) 227–232. doi:10.1016/j.cplett.2004.12.040.
- [10] S. Ahmad, P. Laiho, Q. Zhang, H. Jiang, A. Hussain, Y. Liao, E.X. Ding, N. Wei, E.I. Kauppinen, Gas phase synthesis of metallic and bimetallic catalyst nanoparticles by rod-to-tube type spark discharge generator, *J. Aerosol Sci.* 123 (2018) 208–218. doi:10.1016/j.jaerosci.2018.05.011.
- [11] S. Ahmad, Y. Liao, A. Hussain, Q. Zhang, E.-X. Ding, H. Jiang, E.I. Kauppinen, Systematic investigation of the catalyst composition effects on single-walled carbon nanotubes synthesis in floating-catalyst CVD, *Carbon* 149 (2019) 318–327. doi:10.1016/j.carbon.2019.04.026.
- [12] S. Ahmad, E.-X. Ding, Q. Zhang, H. Jiang, J. Sainio, M. Tavakkoli, A. Hussain, Y. Liao, E.I. Kauppinen, Roles of sulfur in floating-catalyst CVD growth of single-walled carbon nanotubes for transparent conductive film applications, *Chem. Eng. J.* 378 (2019) 122010. doi:10.1016/j.cej.2019.122010.
- [13] T. Rabenau, A. Simon, R.K. Kremer, E. Sohmen, The energy gaps of fullerene C60 and C70 determined from the temperature dependent microwave conductivity, *Zeitschrift Für Phys. B Condens. Matter.* 90 (1993) 69–72. doi:10.1007/BF01321034.
- [14] R. Mirzayev, K. Mustonen, M.R.A. Monazam, A. Mittelberger, T.J. Pennycook, C. Mangler, T. Susi, J. Kotakoski, J.C. Meyer, Buckyball sandwiches, *Sci. Adv.* 3 (2017) 1700176. doi:10.1126/sciadv.1700176.
- [15] M.S. Dresselhaus, G. Dresselhaus, A. Jorio, A.G. Souza Filho, R. Saito, Raman spectroscopy on isolated single wall carbon nanotubes, *Carbon* 40 (2002) 2043–2061. doi:10.1016/S0008-6223(02)00066-0.

- [16] M.S. Dresselhaus, G. Dresselhaus, R. Saito, Physics of carbon nanotubes, *Carbon* 33 (1995) 883–891. doi:10.1016/0008-6223(95)00017-8.
- [17] J.M. Parnis, K.B. Oldham, Beyond the beer-lambert law: The dependence of absorbance on time in photochemistry, *J. Photochem. Photobiol. A Chem.* 267 (2013) 6–10. doi:10.1016/j.jphotochem.2013.06.006.
- [18] File:SSPN41.PNG - Wikipedia, the free encyclopedia,” en.wikipedia.org. [Online]. Available:https://en.wikipedia.org/wiki/Optical_properties_of_carbon_nanotubes#/media/File:SSPN41.PNG [Accessed: 12-May-2019].
- [19] Y. Tian, H. Jiang, J. V. Pfaler, Z. Zhu, A.G. Nasibulin, T. Nikitin, B. Aitchison, L. Khriachtchev, D.P. Brown, E.I. Kauppinen, Analysis of the size distribution of single-walled carbon nanotubes using optical absorption spectroscopy, *J. Phys. Chem. Lett.* 1 (2010) 1143–1148. doi:10.1021/jz100161p.
- [20] M. Ohfuchi, Y. Miyamoto, Optical properties of oxidized single-wall carbon nanotubes, *Carbon* 114 (2017) 418–423. doi:10.1016/j.carbon.2016.12.052.
- [21] H. Kataura, Y. Kumazawa, Y. Maniwa, I. Umez, S. Suzuki, Y. Ohtsuka, Y. Achiba, Optical properties of single-wall carbon nanotubes, *Synth. Met.* 103 (1999) 2555–2558. doi:10.1016/S0379-6779(98)00278-1.
- [22] M.S. Dresselhaus, A. Jorio, M. Hofmann, G. Dresselhaus, R. Saito, Perspectives on carbon nanotubes and graphene Raman spectroscopy, *Nano Lett.* 10 (2010) 751–758. doi:10.1021/nl904286r.
- [23] J.C. Charlier, X. Blase, S. Roche, Electronic and transport properties of nanotubes, *Rev. Mod. Phys.* 79 (2007) 677–726. doi:10.1103/RevModPhys.79.677.
- [24] Band_structure_CNT- Wikipedia, the free encyclopedia,” en.wikipedia.org. [Online]. Available:https://upload.wikimedia.org/wikipedia/commons/a/a5/Band_structure_CNT.jpg [Accessed: 14-May-2019].
- [25] S. Iijima, T. Ichihashi, Single-shell carbon nanotubes of 1-nm diameter, *Nature*. 363 (1993) 603–605. doi:10.1038/363603a0.
- [26] T. Guo, P. Nikolaev, A. Thess, D.T. Colbert, R.E. Smalley, Catalytic growth of single-walled nanotubes by laser vaporization, *Chem. Phys. Lett.* 243 (1995) 49–54. doi:10.1016/0009-2614(95)00825-O.
- [27] H. Dai, A.G. Rinzler, P. Nikolaev, A. Thess, D.T. Colbert, R.E. Smalley, Single-wall nanotubes produced by metal-catalyzed disproportionation of carbon monoxide, *Chem. Phys. Lett.* 260 (1996) 471–475. doi:10.1016/0009-2614(96)00862-7.
- [28] M. He, A.I. Chernov, E.D. Obraztsova, J. Sainio, E. Rikkinen, H. Jiang, Z. Zhu, A. Kaskela, A.G. Nasibulin, E.I. Kauppinen, M. Niemelä, O. Krause, Low Temperature Growth of SWNTs on a Nickel Catalyst by Thermal Chemical Vapor Deposition, *Nano Res.* 4 (2011) 334–342. doi:10.1007/s12274-010-0088-3.
- [29] F. Yang, X. Wang, D. Zhang, J. Yang, D. Luo, Z. Xu, J. Wei, J.Q. Wang, Z. Xu, F. Peng, X. Li, R. Li, Y. Li, M. Li, X. Bai, F. Ding, Y. Li, Chirality-specific growth of single-walled carbon nanotubes on solid alloy catalysts, *Nature*. 510 (2014) 522–524. doi:10.1038/nature13434.
- [30] D. Takagi, Y. Homma, H. Hibino, S. Suzuki, Y. Kobayashi, Single-walled carbon nanotube growth from highly activated metal nanoparticles, *Nano Lett.* 6 (2006) 2642–2645. doi:10.1021/nl061797g.
- [31] B. Liu, W. Ren, L. Gao, S. Li, S. Pei, C. Liu, C. Jiang, H.M. Cheng, Metal-catalyst-free growth of single-walled carbon nanotubes, *J. Am. Chem. Soc.* 131 (2009) 2082–2083. doi:10.1021/ja8093907.
- [32] W. Zhou, L. Ding, J. Liu, Role of catalysts in the surface synthesis of single-walled carbon nanotubes, *Nano Res.* 2 (2009) 593–598. doi:10.1007/s12274-009-9068-x.
- [33] K. Mustonen, P. Laiho, A. Kaskela, Z. Zhu, O. Reynaud, N. Houben, Y. Tian, T. Susi, H. Jiang, A.G. Nasibulin, E.I. Kauppinen, Gas phase synthesis of non-bundled, small diameter single-walled carbon nanotubes with near-armchair chiralities, *Appl. Phys. Lett.* 107 (2015) 013106. doi:10.1063/1.4926415.
- [34] P. Nikolaev, M.J. Bronikowski, R.K. Bradley, F. Rohmund, D.T. Colbert, K.A. Smith, R.E. Smalley, Gas-phase catalytic growth of single-walled carbon nanotubes from carbon monoxide, *Chem. Phys. Lett.* 313 (1999) 91–97. doi:10.1016/S0009-2614(99)01029-5.

- [35] S. Schwyn, E. Garwin, A. Schmidt-Ott, Aerosol generation by spark discharge, *J. Aerosol Sci.* 19 (1988) 639-642. doi:10.1016/0021-8502(88)90215-7.
- [36] Y. Chen, J. Zhang, Diameter controlled growth of single-walled carbon nanotubes from SiO₂ nanoparticles, *Carbon* 49 (2011) 3316-3324. doi:10.1016/j.carbon.2011.04.016.
- [37] V. Jourdain, C. Bichara, Current understanding of the growth of carbon nanotubes in catalytic chemical vapour deposition, *Carbon* 58 (2013) 2-39. doi:10.1016/j.carbon.2013.02.046.
- [38] M. V. Kharlamova, Investigation of growth dynamics of carbon nanotubes, *Beilstein J. Nanotechnol.* 8 (2017) 826-856. doi:10.3762/bjnano.8.85.
- [39] J. Gavillet, J. Thibault, O. Stéphan, H. Amara, A. Loiseau, C. Bichara, J.-P. Gaspard, F. Ducastelle, Nucleation and Growth of Single-Walled Nanotubes: The Role of Metallic Catalysts, *J. Nanosci. Nanotechnol.* 3 (2004) 346-359. doi:10.1166/jnn.2004.068.
- [40] B.O. Mueller, M.E. Messing, D.L.J. Engberg, A.M. Jansson, L.I.M. Johansson, S.M. Norlén, N. Tureson, K. Deppert, Review of spark discharge generators for production of nanoparticle aerosols, *Aerosol Sci. Technol.* 46 (2012) 1256-1270. doi:10.1080/02786826.2012.705448.
- [41] G. Lanzani, A.G. Nasibulin, K. Laasonen, E.I. Kauppinen, CO dissociation and CO+O reactions on a nanosized iron cluster, *Nano Res.* 2 (2009) 660-670. doi:10.1007/s12274-009-9069-9.
- [42] Y. Liahio, Carbon dioxide-assisted synthesis of single-walled carbon nanotubes and their thin film properties, *Dep. Appl. Physics, Dr. Philos. Aalto Univ. Espoo.* (2019). <https://aaltodoc.aalto.fi/handle/123456789/40231>.
- [43] A. Kaskela, A.G. Nasibulin, M.Y. Timmermans, B. Aitchison, A. Papadimitratos, Y. Tian, Z. Zhu, H. Jiang, D.P. Brown, A. Zakhidov, E.I. Kauppinen, Aerosol-synthesized SWCNT networks with tunable conductivity and transparency by a dry transfer technique, *Nano Lett.* 10 (2010) 4349-4353. doi:10.1021/nl101680s.
- [44] P. Laiho, K. Mustonen, Y. Ohno, S. Maruyama, E.I. Kauppinen, M. Arnold, Direct Deposition of Aerosol-Synthesized Single-Walled Carbon Nanotubes by Thermophoresis, *ACS Appl. Mater. Interfaces.* 9 (2017) 20738-20747. doi:10.1021/acsami.7b03151.
- [45] R. Rao, C.L. Pint, A.E. Islam, R.S. Weatherup, S. Hofmann, E.R. Meshot, F. Wu, C. Zhou, N. Dee, P.B. Amama, J. Carpena-Nuñez, W. Shi, D.L. Plata, E.S. Penev, B.I. Yakobson, P.B. Balbuena, C. Bichara, D.N. Futaba, S. Noda, H. Shin, K.S. Kim, B. Simard, F. Mirri, M. Pasquali, F. Fornasier, E.I. Kauppinen, M. Arnold, B.A. Cola, P. Nikolaev, S. Arepalli, H.-M. Cheng, D.N. Zakharov, E.A. Stach, J. Zhang, F. Wei, M. Terrones, D.B. Geohegan, B. Maruyama, S. Maruyama, Y. Li, W.W. Adams, A.J. Hart, Carbon Nanotubes and Related Nanomaterials: Critical Advances and Challenges for Synthesis toward Mainstream Commercial Applications, *ACS Nano.* 12 (2018) 11756-11784. doi:10.1021/acs.nano.8b06511.
- [46] K. Ellmer, Past achievements and future challenges in the development of optically transparent electrodes, *Nat. Photonics.* 6 (2012) 809-817. doi:10.1038/nphoton.2012.282.
- [47] L. Yu, C. Shearer, J. Shapter, Recent Development of Carbon Nanotube Transparent Conductive Films, *Chem. Rev.* 116 (2016) 13413-13453. doi:10.1021/acs.chemrev.6b00179.
- [48] E.X. Ding, H. Jiang, Q. Zhang, Y. Tian, P. Laiho, A. Hussain, Y. Liao, N. Wei, E.I. Kauppinen, Highly conductive and transparent single-walled carbon nanotube thin films from ethanol by floating catalyst chemical vapor deposition, *Nanoscale*, 9 (2017) 17601-17609. doi:10.1039/c7nr05554d.
- [49] S. Jiang, P.X. Hou, M.L. Chen, B.W. Wang, D.M. Sun, D.M. Tang, Q. Jin, Q.X. Guo, D.D. Zhang, J.H. Du, K.P. Tai, J. Tan, E.I. Kauppinen, C. Liu, H.M. Cheng, Ultrahigh-performance transparent conductive films of carbon-welded isolated single-wall carbon nanotubes, *Sci. Adv.* 4 (2018) aap9264. doi:10.1126/sciadv.aap9264.
- [50] K.K. Kim, S.M. Yoon, H.K. Park, H.J. Shin, S.M. Kim, J.J. Bae, Y. Cui, J.M. Kim, J.Y. Choi, Y.H. Lee, Doping strategy of carbon nanotubes with redox chemistry, *New J. Chem.* 34 (2010) 2183-2188. doi:10.1039/conj00138d.
- [51] H. Seyama, M. Soma, B.K.G. Theng, X-Ray Photoelectron Spectroscopy, in: *Dev.*

- Clay Sci., 2013. doi:10.1016/B978-0-08-098259-5.00007-X.
- [52] H. Jiang, A.G. Nasibulin, D.P. Brown, E.I. Kauppinen, Unambiguous atomic structural determination of single-walled carbon nanotubes by electron diffraction, *Carbon* 45 (2007) 662-667. doi:10.1016/j.carbon.2006.07.025.
- [53] K. Han, W. Kim, J. Yu, J. Lee, H. Lee, C. Gyu Woo, M. Choi, A study of pin-to-plate type spark discharge generator for producing unagglomerated nanoaerosols, *J. Aerosol Sci.* 52 (2012) 80-88. doi:10.1016/j.jaerosci.2012.05.002.
- [54] S. Chae, D. Lee, M.-C. Kim, D.S. Kim, M. Choi, Wire-in-Hole-Type Spark Discharge Generator for Long-Time Consistent Generation of Unagglomerated Nanoparticles, *Aerosol Sci. Technol.* 49 (2015) 463-471. doi:10.1080/02786826.2015.1045444.
- [55] R.N. Szenté, R.J. Munz, M.G. Drouet, Copper-niobium and copper-tungsten composites as plasma torch cathodes, *J. Phys. D. Appl. Phys.* 27 (1994) 1443-1447. doi:10.1088/0022-3727/27/7/015.
- [56] N.S. Tabrizi, M. Ullmann, V.A. Vons, U. Lafont, A. Schmidt-Ott, Generation of nanoparticles by spark discharge, *J. Nanoparticle Res.* 11 (2009) 315-332. doi:10.1007/s11051-008-9407-y.
- [57] M.M. Pejovic, G.S. Ristic, J.P. Karamarkovic, Electrical breakdown in low pressure gases, *J. Phys. D. Appl. Phys.* 35 (2002) R91-R103. doi:10.1088/0022-3727/35/10/201.
- [58] W.H. Chiang, R.M. Sankaran, Microplasma synthesis of metal nanoparticles for gas-phase studies of catalyzed carbon nanotube growth, *Appl. Phys. Lett.* 91 (2007) 121503. doi:10.1063/1.2786835.
- [59] O. V. Yazyev, A. Pasquarello, Effect of metal elements in catalytic growth of carbon nanotubes, *Phys. Rev. Lett.* 18 (2008) 156102. doi:10.1103/PhysRevLett.100.156102.
- [60] F. Ding, P. Larsson, J.A. Larsson, R. Ahuja, H. Duan, A. Rosen, K. Bolton, The importance of strong carbon-metal adhesion for catalytic nucleation of single-walled carbon nanotubes, *Nano Lett.* 8 (2008) 463-468. doi:10.1021/nl072431m.
- [61] I. Ibrahim, J. Kalbacova, V. Engemaier, J. Pang, R.D. Rodriguez, D. Grimm, T. Gemming, D.R.T. Zahn, O.G. Schmidt, J. Eckert, M.H. Rummeli, Confirming the Dual Role of Etchants during the Enrichment of Semiconducting Single Wall Carbon Nanotubes by Chemical Vapor Deposition, *Chem. Mater.* 27 (2015) 5964-5973. doi:10.1021/acs.chemmater.5b02037.
- [62] K. Cui, A. Kumamoto, R. Xiang, H. An, B. Wang, T. Inoue, S. Chiashi, Y. Ikuhara, S. Maruyama, Synthesis of subnanometer-diameter vertically aligned single-walled carbon nanotubes with copper-anchored cobalt catalysts, *Nanoscale*. 8 (2016) 1608-1617. doi:10.1039/C5NR06007A.
- [63] A. Hussain, Y. Liao, Q. Zhang, E.X. Ding, P. Laiho, S. Ahmad, N. Wei, Y. Tian, H. Jiang, E.I. Kauppinen, Floating catalyst CVD synthesis of single walled carbon nanotubes from ethylene for high performance transparent electrodes, *Nanoscale*. 10 (2018) 9752-9759. doi:10.1039/c8nr00716k.
- [64] M. He, A.I. Chernov, E.D. Obraztsova, H. Jiang, E.I. Kauppinen, J. Lehtonen, Synergistic effects in FeCu bimetallic catalyst for low temperature growth of single-walled carbon nanotubes, *Carbon* 52 (2013) 590-594. doi:10.1016/j.carbon.2012.10.029.
- [65] V.I. Artyukhov, E.S. Penev, B.I. Yakobson, Why nanotubes grow chiral, *Nat. Commun.* (2014) 5:4892. doi:10.1038/ncomms5892.
- [66] Y. Liao, H. Jiang, N. Wei, P. Laiho, Q. Zhang, S.A. Khan, E.I. Kauppinen, Direct Synthesis of Colorful Single-Walled Carbon Nanotube Thin Films, *J. Am. Chem. Soc.* 140 (2018) 9797-9800. doi:10.1021/jacs.8b05151.
- [67] B. Yu, C. Liu, P.X. Hou, Y. Tian, S. Li, B. Liu, F. Li, E.I. Kauppinen, H.M. Cheng, Bulk synthesis of large diameter semiconducting single-walled carbon nanotubes by oxygen-assisted floating catalyst chemical vapor deposition, *J. Am. Chem. Soc.* 133 (2011) 5232-5235. doi:10.1021/ja2008278.
- [68] W. Ren, F. Li, H.M. Cheng, Evidence for, and an understanding of, the initial nucleation of carbon nanotubes produced by a floating catalyst method, *J. Phys. Chem. B.* 110 (2006) 16941-16946. doi:10.1021/jp062526x.

- [69] J.J. Fan, Y.J. Fan, R.X. Wang, S. Xiang, H.G. Tang, S.G. Sun, A novel strategy for the synthesis of sulfur-doped carbon nanotubes as a highly efficient Pt catalyst support toward the methanol oxidation reaction, *J. Mater. Chem. A* 5 (2017) 19467-19475. doi:10.1039/c7ta05102f.
- [70] D.C. Higgins, M.A. Hoque, F. Hassan, J.Y. Choi, B. Kim, Z. Chen, Oxygen reduction on graphene-carbon nanotube composites doped sequentially with nitrogen and sulfur, *ACS Catal.* 4 (2014) 2734-2740. doi:10.1021/cs5003806.
- [71] D.R. Alfonso, First-principles studies of H₂S adsorption and dissociation on metal surfaces, *Surf. Sci.* 602 (2008) 2758-2768. doi:10.1016/j.susc.2008.07.001.
- [72] A.N. Startsev, N.N. Bulgakov, S.P. Ruzankin, O. V. Kruglyakova, E.A. Paukshtis, The reaction thermodynamics of hydrogen sulfide decomposition into hydrogen and diatomic sulfur, *J. Sulfur Chem.* 36 (2015) 234-239. doi:10.1080/17415993.2015.1010533.
- [73] J. Wei, H. Zhu, Y. Jia, Q. Shu, C. Li, K. Wang, B. Wei, Y. Zhu, Z. Wang, J. Luo, W. Liu, D. Wu, The effect of sulfur on the number of layers in a carbon nanotube, *Carbon* 45 (2007) 2152-2158. doi:10.1016/j.carbon.2007.07.001.
- [74] O. Reynaud, A.G. Nasibulin, A.S. Anisimov, I. V. Anoshkin, H. Jiang, E.I. Kauppinen, Aerosol feeding of catalyst precursor for CNT synthesis and highly conductive and transparent film fabrication, *Chem. Eng. J.* 255 (2014) 134-140. doi:10.1016/j.cej.2014.06.082.
- [75] M.S. Motta, A. Moisala, I.A. Kinloch, A.H. Windle, The Role of Sulphur in the Synthesis of Carbon Nanotubes by Chemical Vapour Deposition at High Temperatures, *J. Nanosci. Nanotechnol.* 8 (2008) 2442-2449. doi:10.1166/jnn.2008.500.
- [76] Y. Tian, H. Jiang, P. Laiho, E.I. Kauppinen, Validity of Measuring Metallic and Semiconducting Single-Walled Carbon Nanotube Fractions by Quantitative Raman Spectroscopy, *Anal. Chem.* 90 (2018) 2517-2525. doi:10.1021/acs.analchem.7b03712.
- [77] Y. Yuan, H.E. Karahan, C. Yildirim, L. Wei, Ö. Birer, S. Zhai, R. Lau, Y. Chen, Smart poisoning of Co/SiO₂ catalysts by sulfidation for chirality-selective synthesis of (9,8) single-walled carbon nanotubes, *Nanoscale* 8 (2016) 17705-17713. doi:10.1039/c6nr05938d.
- [78] Y. Yuan, L. Wei, W. Jiang, K. Goh, R. Jiang, R. Lau, Y. Chen, Sulfur-induced chirality changes in single-walled carbon nanotube synthesis by ethanol chemical vapor deposition on a Co/SiO₂ catalyst, *J. Mater. Chem. A* 3 (2015) 3310-3319. doi:10.1039/c4ta05917d.
- [79] R.H. Baughman, A.A. Zakhidov, W.A. De Heer, Carbon nanotubes - The route toward applications, *Science* 297 (2002) 787-792. doi:10.1126/science.1060928.
- [80] A.K. Geim, K.S. Novoselov, The rise of graphene, *Nat. Mater.* 6 (2007) 183-191. doi:10.1038/nmat1849.
- [81] A.G. Nasibulin, P. V. Pikhitsa, H. Jiang, D.P. Brown, A. V. Krashennnikov, A.S. Anisimov, P. Queipo, A. Moisala, D. Gonzalez, G. Lientschnig, A. Hassanien, S.D. Shandakov, G. Lolli, D.E. Resasco, M. Choi, D. Tománek, E.I. Kauppinen, A novel hybrid carbon material, *Nat. Nanotechnol.* 2 (2007) 156-161. doi:10.1038/nnano.2007.37.
- [82] Y. Tian, D. Chassaing, A.G. Nasibulin, P. Ayala, H. Jiang, A.S. Anisimov, E.I. Kauppinen, Combined Raman spectroscopy and transmission electron microscopy studies of a NanoBud structure, *J. Am. Chem. Soc.* 130 (2008) 7188-7189. doi:10.1021/ja801120u.
- [83] Y. Hao, M.S. Bharathi, L. Wang, Y. Liu, H. Chen, S. Nie, X. Wang, H. Chou, C. Tan, B. Fallahzad, H. Ramanarayan, C.W. Magnuson, E. Tutuc, B.I. Yakobson, K.F. McCarty, Y.W. Zhang, P. Kim, J. Hone, L. Colombo, R.S. Ruoff, The role of surface oxygen in the growth of large single-crystal graphene on copper, *Science* 342 (2013) 720-723. doi:10.1126/science.1243879.
- [84] J.H. Lee, E.K. Lee, W.J. Joo, Y. Jang, B.S. Kim, J.Y. Lim, S.H. Choi, S.J. Ahn, J.R. Ahn, M.H. Park, C.W. Yang, B.L. Choi, S.W. Hwang, D. Whang, Wafer-scale growth of single-crystal monolayer graphene on reusable hydrogen-terminated germanium, *Science* 344 (2014) 286-289. doi:10.1126/science.1252268.
- [85] H.B. Li, A.J. Page, S. Irle, K. Morokuma, Revealing the dual role of hydrogen for

- growth inhibition and defect healing in polycyclic aromatic hydrocarbon formation: QM/MD simulations, *J. Phys. Chem. Lett.* 4 (2013) 2323-2327. doi:10.1021/jz400925f.
- [86] Y. Liao, A. Hussain, P. Laiho, Q. Zhang, Y. Tian, N. Wei, E.X. Ding, S.A. Khan, N.N. Nguyen, S. Ahmad, E.I. Kauppinen, Tuning Geometry of SWCNTs by CO₂ in Floating Catalyst CVD for High-Performance Transparent Conductive Films, *Adv. Mater. Interfaces.* 5 (2018) 1801209. doi:10.1002/admi.201801209.

The catalyst particle being seed for the growth of SWCNTs is one of the most important parameter to determine morphology and chirality of SWCNTs. The development of spark discharge based FC-CVD technique in the present thesis has enabled decoupling of the catalyst and SWCNTs formation into two subsequent processes. We employed this technique to investigate the roles of catalyst composition on various characteristics of SWCNTs including their yield, morphology and chirality. Moreover, we found that the addition of sulfur promoter in the growth process of SWCNTs enhances the performance of SWCNT based transparent conductive films, which have potential applications in emerging flexible, bendable and stretchable display devices.

In addition, we developed a novel gas-phase method for the simultaneous growth of 0D-fullerene, 1D-SWCNTs and 2D-graphene in the presence of spherical catalyst nanoparticles. Fullerene and SWCNTs rise from graphene through selective removal of atoms that force the 2D-sheet into 1D-tubular or a 0D-spherical configuration. We demonstrated that under carefully chosen gas atmosphere along with SWCNTs and fullerenes, graphene flakes emerge within the gas-suspension and grow to a size as large as several hundreds of nanometers without folding or crumpling. Since, in the applied process the formation of the structures takes place in gas-suspension, the as-synthesized hybrid films can be directly deposited on any surface with an arbitrary thickness, which offers a new route towards ultra-fast manufacturing of the hybrid material at industrial scale.



ISBN 978-952-60-3795-0 (printed)

ISBN 978-952-60-3796-7 (pdf)

ISSN 1799-4934 (printed)

ISSN 1799-4942 (pdf)

Aalto University
School of Science
Department of Physics
www.aalto.fi

**BUSINESS +
ECONOMY**

**ART +
DESIGN +
ARCHITECTURE**

**SCIENCE +
TECHNOLOGY**

CROSSOVER

**DOCTORAL
DISSERTATIONS**